SINGULAR HOPF BIFURCATION

A Dissertation

Presented to the Faculty of the Graduate School

of Cornell University

in Partial Fulfillment of the Requirements for the Degree of

Doctor of Philosophy

by

Philipp Meerkamp

August 2012

SINGULAR HOPF BIFURCATION

Philipp Meerkamp, Ph.D.

Cornell University 2012

This dissertation concerns singular Hopf bifurcation in slow-fast vector fields with one fast and two slow variables. Singular Hopf bifurcation occurs generically in this setting. Singular Hopf bifurcation is important in the understanding of mixed-mode oscillations in systems modeling electrical activity in neural cells and chemical oscillations. Three approaches are taken in this study of singular Hopf bifurcation.

First, we analyze a normal form for singular Hopf bifurcation. Normal forms for this bifurcation depend upon several parameters, and the dynamics displayed by the normal forms is intricate. Extensive bifurcation diagrams of equilibrium points and periodic orbits that are close to singular Hopf bifurcation are presented. In addition, parameters are determined where there is a tangency between invariant manifolds that can mark the onset of mixed-mode oscillations in systems near singular Hopf bifurcation. One parameter of the normal form is identified as the primary bifurcation parameter, and we present a catalog of bifurcation sequences that occur as the primary bifurcation parameter is varied. These results are used to estimate the parameters for the onset of mixed-mode oscillations in a model of chemical oscillations.

Second, we present an in-depth study singular Hopf bifurcation and mixed-mode oscillations in a system modeling electric activity in a pituitary lactotroph cell. We transform the lactotroph model into singular Hopf normal form and analyze in detail to which extent the normal form approximates the lactotroph model. It is shown that mixed-mode oscillations in the lactotroph model are over large parameter ranges due to singular Hopf bifurcation.

Third, we describe a numerical method to rigorously compute enclosures of slow manifolds. Locally partitioning parameter space into regions with distinct behaviors, slow manifolds are central objects in the study of vector fields with multiple time scales as well as of mixed-mode oscillations. Important parts of the analysis of the singular Hopf normal form also involve slow manifolds. Computing slow manifolds poses two main challenges. First, slow manifolds are defined asymptotically in terms of the parameter ϵ separating the time scales and are thus non-unique fuzzy objects for $\epsilon > 0$. We meet this challenge by defining computable slow manifolds, which can be computed for $\epsilon > 0$. Second, the separation of time scales poses problems for many numerical schemes. The method to rigorously compute enclosures of slow manifolds described here becomes more efficient as $\epsilon \to 0$.

BIOGRAPHICAL SKETCH

Philipp Meerkamp was born in Bremen, Germany, in 1985. He received his secondary education in Stuhr, Germany, and, briefly, in Ecommoy, France. After attending Palmer's College in the United Kingdom for two years, he graduated from high-school ("A-levels") in 2004. His studies at Jacobs University Bremen, then called International University Bremen, concluded three years later with a Bachelor of Science in Mathematics and the desire to pursue PhD studies in the subject. Philipp began his doctoral studies in the Cornell Department of Mathematics in 2007.

To my family, who sparked my passion for science.

ACKNOWLEDGEMENTS

First, I would like to thank John Guckenheimer. He has been a perfect advisor. I admire his great intuition as well as broad knowledge and deep understanding of mathematics and other sciences. John has always been there to advise and discuss. He was usually ready to meet in person within 24 hours, or immediately responded by email with a concisely phrased effective idea. In our meetings, he has been extraordinarily patient, often explaining the same concept several times. I feel grateful and indebted to John for the help and support that I have received as his student. I am fortunate to have had John as my advisor.

I also would like to thank my committee members, David Bindel, Richard Rand and Alex Vladimirsky, for their advice, guidance and instruction, especially during my first years as a graduate student. I have also received support and outstanding instruction from John Hamal Hubbard and Yulij Ilyashenko.

Over the last four years, I have had several discussions and email exchanges with Hinke Osinga and Bernd Krauskopf (both at the University of Auckland) as well as their former student Mathieu Desroches (at INRIA Paris-Rocquencourt Centre). I am grateful for their ideas and input, which substantially strengthened my work with John Guckenheimer.

It was a true pleasure to collaborate with Tomas Johnson on a rigorous method to find enclosures of slow manifolds. He taught me most of what I know about validated numerical methods. Chapter 5 of this dissertation is based on joint work with him and John Guckenheimer. In addition, I had fine fellow PhD group members, whose advice and help in and outside of group meetings I am thankful for: Christian Kühn (now at the Vienna University of Technology), Chris Scheper (now at Opera Solutions) and Sarah Iams.

I am grateful for the help and support I received from the Mathematics department's network administrator Steve Gaarder. During my time at Cornell, I must have asked him for more favors than any other student in the program. I would moreover like to thank the graduate field coordinators of the Department of Mathematics, Donna Smith, Brenda Smith, and Melissa Totman.

Although I was officially a member of the Mathematics Department, the Center for Applied Mathematics (CAM) at Cornell University has always felt like a second home to me. I want to thank the graduate student CAMsters for their comradery and hospitality.

Dierk Schleicher (Jacobs University) has been a mentor since my first week as an undergraduate, when he convinced me to skip the first-year calculus courses and instead take an analysis class that began with the definition of a topological space. I am thankful for his insistence. In 2012, we published the paper "Hausdorff dimension and biaccessibility for polynomial Julia sets", in which we strengthened a theorem by Stanislav Smirnov and Anna Zdunik. Without Dierk's encouragement and guidance throughout the years, I would not have entered a PhD program in Mathematics.

I would like to thank my girlfriend Zhengyi, who has been a source of moral support and happiness. I am grateful for her proof-reading, constructive criticism, and help in improving earlier much less polished versions of this dissertation.

I am deeply grateful for the care and education I have received from my parents and grandparents since the very day I was born. It was through them that I became fascinated by science years before entering school, and because of their upbringing and encouragement that I persevered when challenges were harder than I had anticipated. In a sense, my scientific career really began in our living room.

TABLE OF CONTENTS

LIST OF TABLES

LIST OF FIGURES

CHAPTER 1

MOTIVATION AND RESULTS

Singular Hopf bifurcation has been observed in systems modeling action potentials in neurons as well as chemical reactions: examples include a reduced Hogdkin-Huxley model (see [9] and [12] for recent results) that has a subcritical singular Hopf bifurcation, a model for chemical reactors introduced by Koper [38, 41, 9] that has a supercritical singular Hopf bifurcation, and a model for an autocatalator first studied by Petrov, Scott and Showalter (see [56], as well as [48], [19] and [25] for more recent studies). All of these models exhibit mixed-mode oscillations that are directly related to singular Hopf bifurcation. Singular Hopf bifurcations are also present in a model of electrical activity in a pituitary lactotroph cell, introduced by Toporikova et al. [62].

We present work on three aspects of singular Hopf bifurcation, contained in Chapters 3 to 5 of this dissertation.

Chapter 3 is an extensive numerical investigation of a normal form for singular Hopf bifurcation in one fast and two slow variables that was introduced by Guckenheimer in [19]. New dynamical phenomena, not predicted by the Hopf theory in single time-scale systems, are found in the normal form. This is already true in systems with one slow and one fast variable undergoing singular Hopf bifurcation where there is a canard explosion [13], but the dynamics are far more complicated in systems with two slow variables and one fast variable. Guckenheimer [19] initiated the study of these phenomena. He observed bifurcations of equilibrium points and periodic orbits in the normal form, and showed that a tangency of invariant manifolds is present. We extend that work by mapping several types of bifurcations into the four-dimensional parameter space of the normal form. The main contributions of Chapter 3 are the numerically computed bifurcation diagrams and tables that locate these subsidiary bifurcations in a scaled version

of the normal form. Most of the bifurcations that we locate for the scaled normal form are non-degenerate and will persist when the system is perturbed. Thus, the bifurcation diagrams constitute a database that can be used to predict where additional bifurcations will be found near singular Hopf bifurcations of more complicated examples. Since numerical studies of the bifurcations of more complicated systems are challenging, we hope that this information will point to dynamical behaviors that might be difficult to discover otherwise. We illustrate this using a system studied by Koper [38]. Note that tangency bifurcations between a repelling slow manifold and the unstable manifold of the equilibrium point are especially important in the global dynamics of mixed-mode oscillations of this example.

Material from dissertation Chapter 3 was accepted for publication by the SIAM Journal on Applied Dynamical Systems in June 2012 in an article titled "Unfoldings of singular Hopf bifurcation", authored by John Guckenheimer and Philipp Meerkamp [24]. Some passages from the article are contained in other parts of this dissertation.

Chapter 4 of this dissertation is an in-depth study of singular Hopf bifurcation and mixed-mode oscillations in a model for electrical activity in a pituitary lactroph cell, introduced by Toporikova et al. [62]. Specifically, the lactotroph model is transformed into singular Hopf normal form in a sequence of coordinate transformations that is followed by a truncation of higher-order terms. We compare the bifurcation behavior of the lactotroph model with that of its normal form approximation. The chapter concludes with a study of mixed-mode oscillations in the lactotroph model, in which we find that in the lactotroph model, mixed-mode oscillations are primarily due to singular Hopf bifurcation rather than folded nodes. This confirms the importance of singular Hopf bifurcation in the analysis of oscillatory behavior in biologically relevant parameter regions of models for electrical activity in neurons.

Material from Chapter 4 is work by John Guckenheimer and Philipp Meerkamp.

Chapter 5 introduces an algorithm to rigorously compute slow manifolds using interval analysis. We compute enclosures of slow manifolds by exploiting transversality properties that improve as the separation of time scales parameter ϵ tends to 0, while working well even for moderately small values of ϵ. If H is a hypersurface and F is a vector field, then transversality of F to H is a *local* property: verification does not rely upon computation of trajectories of F. For a slow-fast vector field with one fast variable, translation of a normally hyperbolic critical manifold along the fast direction produces a transverse hypersurface when the translation distance is large enough. Translation distances proportional to ϵ suffice. We use piecewise linear surfaces H as enclosing manifolds. For the example we consider, transversality at vertices of a face of H implies transversality of the entire face. This reduces the computational complexity of checking transversality sufficiently that iterative refinement of the enclosures was feasible.

Since slow manifolds are objects that are defined asymptotically in terms of ϵ, they are not directly computable using finite information. We therefore develop a mathematical framework within which slow manifolds are defined for fixed values of $\epsilon > 0$. We define *computable slow manifolds* and relate this concept to the slow manifolds studied in geometric singular perturbation theory. This is similar in spirit to the finite resolution dynamics approach of Luzzatto and Pilarczyk [47].

The work on enclosures of slow manifolds is motivated by the study of tangencies of invariant manifolds. Proving the existence of tangencies is intrinsically complicated because the manifolds themselves must be tracked over a range of parameters. Computer-aided proofs of tangencies of invariant manifolds have previously been studied by Arai and Mischaikow in [1], and Wilczak and Zgliczyński in [68]. In Section 5.6, we prove that a tangency bifurcation involving a computable slow manifold occurs in

the singular Hopf normal form. Note that the tangency curves shown in Chapter 3 and Appendix B are non-rigorous since they were computed before the development of our rigorous method to enclose slow manifolds.

The material from Chapter 5 is work by John Guckenheimer, Tomas Johnson, and Philipp Meerkamp, and was accepted for publication by the SIAM Journal on Applied Dynamical Systems in May 2012 [22]. Some passages from the article are contained in other parts of this dissertation.

CHAPTER 2

BACKGROUND

2.1 Slow-fast dynamical systems

2.1.1 Basic terminology

Slow-fast differential equations have the form

$$\begin{aligned} \epsilon \dot{x} &= f(x, y, \epsilon) \\ \dot{y} &= g(x, y, \epsilon), \end{aligned} \tag{2.1}$$

where $x \in \mathbb{R}^n$, $y \in \mathbb{R}^m$, $f : \mathbb{R}^{n+m+1} \to \mathbb{R}^n$, and $g : \mathbb{R}^{n+m+1} \to \mathbb{R}^m$. We assume that the vector field (f, g) is smooth (C^∞), although most of the theory can easily be adapted to the finitely differentiable setting. Here x and y are the fast and slow variables, respectively. Chapters 3, 4 and 5 exclusively deal with systems that have two slow variables and one fast variable.

The *critical manifold* is the set

$$S_0 := \{(x, y) \in \mathbb{R}^{n+m} : f(x, y, 0) = 0\}. \tag{2.2}$$

The critical manifold is *normally hyperbolic* at points where $D_x f$ is hyperbolic, i.e., has no eigenvalue whose real part is zero. Sets where the critical manifold is not normally hyperbolic are referred to as *folds*. On normally hyperbolic pieces of the critical manifold, x is a function of y, $x = h_0(y)$. The corresponding differential equation

$$\dot{y} = g(h_0(y), y, 0) \tag{2.3}$$

is called the *slow flow* and can be thought of as the flow of on normally hyperbolic subsets of the critical manifold in the singular limit. A general procedure that rescales

time can be used to extend the reduced system to the fold points of S_0 [9]. We refer the resulting vector field as the *desingularized slow flow*.

Scaling time in system (2.1) by ϵ and setting $\epsilon = 0$, one obtains the *layer equation*:

$$\begin{aligned} x' &= f(x, y, 0) \\ y' &= 0 \end{aligned} \tag{2.4}$$

The layer equation can be thought of as the time-scaled flow at some distance from the critical manifold in the singular limit. Note that the manifold S_0 is exactly the set of critical points for the layer equation.

2.1.2 Fenichel theory and slow manifolds

Singular perturbation theory studies how the solutions to (2.1) for ϵ small, but positive, can be understood by studying solutions to (2.3) and (2.4). When $\epsilon > 0$ is sufficiently small, Fenichel's theorems [15, 34] guarantee that compact normally hyperbolic subsets of S_0 perturb to *slow manifolds*. Slow manifolds are smooth *locally invariant* manifolds, i.e., the vector field is tangent to it. They are $O(\epsilon)$ close to the critical manifold. However, slow manifolds are not unique, although different choices are within $O(e^{-c/\epsilon})$ distance from each other for some constant $c > 0$. The vector field is $O(1)$ on the slow manifold. The stability of the slow manifold is inherited from the stability of the corresponding family of equilibria of the layer equation. In slow-fast systems with one fast and two slow variables, slow manifolds are thus either attracting or repelling surfaces in three-dimensional space. Borrowing terminology from fluid dynamics, the solutions of systems with multiple time scales can have (boundary) layers in which the fast time scale determines the rate at which the solution varies.

The slow manifolds play a prominent role in qualitative analysis of the dynamics and bifurcations of multiple time scale systems. Indeed, model reduction procedures are frequently employed that replace a model by a lower-dimensional model that approximates the motion along a slow manifold and ignores the fast dynamics of the original model. The fast dynamics can then be taken into account by adding "jumps" in which the slow variables are fixed. For instance, a trajectory might follow a repelling slow manifold for a while, before jumping to then follow an attracting slow manifold. The ideal for this type of model reduction is an algorithm that computes the slow manifold exactly. That ideal seems very difficult to achieve. However, Chapter 5 presents an algorithm to compute rigorous bounds for the location of the slow manifold that are tight enough to give information that can be used in the analysis of bifurcations of the system.

2.1.3 Folded singularities

Qualitative analysis of the dynamics of slow-fast systems has been limited largely to systems with one or two slow variables. (See Wechselberger [67] for a recent study of systems with more than two slow variables.) Folded singularities of systems with two slow variables have received particular emphasis. *Folded singularities* separate segments along the fold where trajectories of the reduced system approach the fold from segments where trajectories of the reduced system flow away from the fold. Depending on the linear stability of a folded singularity in the desingularized slow flow, a folded singularity is referred to as a *folded saddle*, *folded node*, et cetera. Arnold et al. [2] studied the reduction of a system near a fold by means of coordinate transformations and rescaling to obtain a *system of first approximation*, in which all variables evolve on the same time scale. In generic slow-fast systems with two slow variables, the system

of first approximation at a folded singularity is

$$\begin{aligned} \dot{x} &= (y - x^2) \\ \dot{y} &= z \pm x \\ \dot{z} &= \alpha. \end{aligned} \tag{2.5}$$

The dynamics of these families was studied by Benoit [4] who observed that small amplitude oscillations occur in the vicinity of folded nodes: the case with a minus sign and $0 < \alpha < 1/8$. These oscillations were studied further by Wechselberger [66] and by Guckenheimer and Haiduc [20]. Their role as a mechanism for producing mixed-mode oscillations is reviewed by Desroches et al. [9].

Szmolyan and Wechselberger [59] investigated the ways in which folded singularities can bifurcate in generic one-parameter families of slow-fast systems with two slow variables. They named the two types of bifurcations that they studied *folded saddle-nodes type I* and *folded saddle-nodes type II*. At a folded saddle-node type I, a folded node and a folded saddle coalesce. At a folded saddle-node type II, an equilibrium of the reduced system crosses the fold curve. This equilibrium is also an equilibrium of the full system that crosses the fold of $f = 0$.

2.2 Singular Hopf bifurcation

2.2.1 Definition of singular Hopf bifurcation

In a slow-fast system, an equilibrium point may cross a fold of the critical manifold. If it undergoes a Hopf bifurcation at $O(\epsilon)$ distance from the fold both in parameter and phase space, we follow [19] and refer to this as a *singular Hopf bifurcation*.

In a one-parameter family of systems, if an equilibrium point of the desingularized system crosses the folds of C, there is a folded saddle-node of type II where it does so. In the full system, there is typically a Hopf bifurcation point at parameter values and state space location that are within $O(\epsilon)$ of the folded saddle-node of type II. This Hopf bifurcation is singular in the sense that its imaginary eigenvalues have a magnitude that is $O(\sqrt{1/\epsilon})$ and thus intermediate between the fast and slow time scales. Thus, the folded saddle-node of type II can be viewed as the singular limit of a singular Hopf bifurcation.

Singular Hopf bifurcation has also been studied in [13, 4, 5].

2.2.2 Normal forms in dynamical systems theory

Bifurcation analysis of dynamical systems is usually based upon the introduction of *normal forms*. Since bifurcation theory of slow-fast systems is a subject that is still in its infancy, we review the use of normal forms in systems with a single time scale [21]. Normal forms are representatives of a class of systems having a specified property, but how this class is chosen varies with the context. Classes of bifurcations are specified by *defining equations* and non-degeneracy conditions [16] . Consider the case of Hopf bifurcation as an example. The defining equations for a Hopf bifurcation specify that a one-parameter family of vector fields has an equilibrium with a pair of complex eigenvalues whose real parts are zero at the bifurcation value of the parameter. *Nondegeneracy assumptions* are imposed that imply that the remaining eigenvalues have non-zero real part and that the derivative of the real parts of the imaginary eigenvalues with respect to the parameter is non-zero. The *center manifold theorem* reduces further analysis of the bifurcation to a system with two-dimensional phase space and coordinate transfor-

mations in the center manifold are used to simplify the analytic expression of the vector field. Roughly, one tries to remove as many terms in the Taylor expansion of the vector as possible. An algebraic calculation finds two *resonant* terms in each odd degree. It is customary to truncate the expansion at degree three and call the resulting system *the* normal form for the Hopf bifurcation. If the appropriate degree three resonant term in the normal form is non-zero, the Hopf bifurcation theorem characterizes the dynamics of the vector field near the bifurcation. It proves that a periodic orbit emerges from the equilibrium point at the bifurcation and demonstrates that the family of vector fields is locally structurally stable: perturbations of the family are topologically equivalent to one another in a neighborhood of the equilibrium point. Similar procedures are used to find normal forms for other types of bifurcations, but few cases yield normal forms that are structurally stable like Hopf bifurcation. For example, tangencies of stable and unstable manifolds of a periodic orbit near some codimension-two "double" Hopf bifurcation with two pairs of imaginary eigenvalues at an equilibrium preclude a structurally stable normal form [21].

2.2.3 Normal form for singular Hopf bifurcation

Guckenheimer [19] introduced the following normal form for singular Hopf bifurcation in slow-fast vector fields with one fast and two slow variables

$$\begin{aligned} \dot{x} &= (y - x^2)/\epsilon \\ \dot{y} &= z - x \\ \dot{z} &= -\mu - ax - by - cz, \end{aligned} \tag{2.6}$$

which depends upon the four parameters μ, a, b, c as well as ϵ.

The reduction of a general slow-fast system with one fast variable x and two slow

variables (y, z) to the normal form (2.6) follows the procedure used by Arnold et al. [2]. We assume that the system has an equilibrium at the origin that crosses the fold curve of its critical manifold. The first step of the reduction uses singularity theory to transform the critical manifold to the paraboloid $y = x^2$. The equation for $\dot{x}$ then has the form $\epsilon\dot{x} = h_1(x, y, z)(y - x^2)$ with $h_1 \neq 0$. Rescaling time by h_1 makes $\epsilon\dot{x} = (y - x^2)$. At the origin, we now require that the gradient of $\dot{y}$ has non-zero projections both along the fast direction and along the fold curve. Writing $\dot{y} = h_2(y, z) + xh_3(x, y, z)$, we assume $h_3(0, 0, 0) = \beta < 0$. (The case $\beta > 0$ does not have a Hopf bifurcation.) Scaling x, y and t by factors $(-\beta)^{1/2}$, $-\beta$ and $(-\beta)^{-1/2}$ leaves the equation for $\dot{x}$ unchanged and makes $h_3(0, 0, 0) = -1$. We make a final coordinate change by replacing z with h_2 using the assumption that $\frac{\partial h_2}{\partial z} \neq 0$. This coordinate change makes the second equation of the system $\dot{y} = z - xh_3$. Note that the coordinate changes preserve the slow-fast splitting of the vector field. To obtain our normal form, the equations for $\dot{y}$ and $\dot{z}$ are truncated, retaining only constant and linear terms.

A system of first approximation can be obtained from the normal form (2.6) by a scaling transformation that eliminates ϵ as a parameter:

$$(X, Y, Z, T) = (\epsilon^{-1/2}x, \epsilon^{-1}y, \epsilon^{-1/2}z, \epsilon^{-1/2}t) \text{ and } (A, B, C) = (\epsilon^{1/2}a, \epsilon b, \epsilon^{1/2}c) \tag{2.7}$$

We obtain

$$\begin{aligned} X' &= Y - X^2 \\ Y' &= Z - X \\ Z' &= -\mu - AX - BY - CZ. \end{aligned} \tag{2.8}$$

Most of the analysis in Chapter 3 uses the system of first approximation rather than the normal form, as the presentation of the bifurcation structure of a four-parameter system is more easily accomplished than for a five-parameter system. For any fixed value of ϵ, the rescaling can be undone to obtain information about the original system (2.6). Argu-

ments involving ideas from geometric singular perturbation theory are often more easily conveyed for the original system that still contains ϵ explicitly. We thus work directly with system (2.6) in a part of Section 3.2. The results obtained there are translated to results about the system of first approximation. Note that in system (2.8), phenomena that are *local* to the origin, i.e. those that occur at bounded distance from the origin, are of particular interest: they tend to the origin in system (2.6) as $\epsilon \to 0$, and are thus likely to persist under perturbations to system (2.6). Therefore, most of Chapter 3 discusses local phenomena in system (2.8).

2.3 Mixed-mode oscillations

Mixed-mode oscillations (MMOs) are oscillations whose time series display cycles of at least two distinct amplitudes [9]. An example of an MMO trajectory occurring in the lactotroph model treated in Chapter 4 is shown in Figure 2.1. Guckenheimer identified singular Hopf bifurcation as a creation mechanism for mixed-mode oscillations [19]. In this setting, MMOs result from the concatenation of small-amplitude oscillations close to a fold of the critical manifold and large-amplitude oscillations in which the trajectory leaves the fold region. More precisely, the trajectory approaches a saddle-focus equilibrium that is close to undergoing singular Hopf bifurcation along its one-dimensional stable manifold and begins to oscillate around the stable eigendirection as it gets closer to the equilibrium. The oscillations increase in amplitude as the trajectory spirals away from the equilibrium in the equilibrium's two-dimensional unstable manifold. If the relative positions of the unstable manifold and the slow-fast system's repelling slow manifold are suitable, the trajectory can eventually leave the fold region, and can, in the presence of a return mechanism to the fold region, approach the equilibrium point again. Guckenheimer [19] identified a tangential intersection of the equilibrium's un-

stable manifold with the repelling slow manifold as an event that can mark the onset of MMOs.

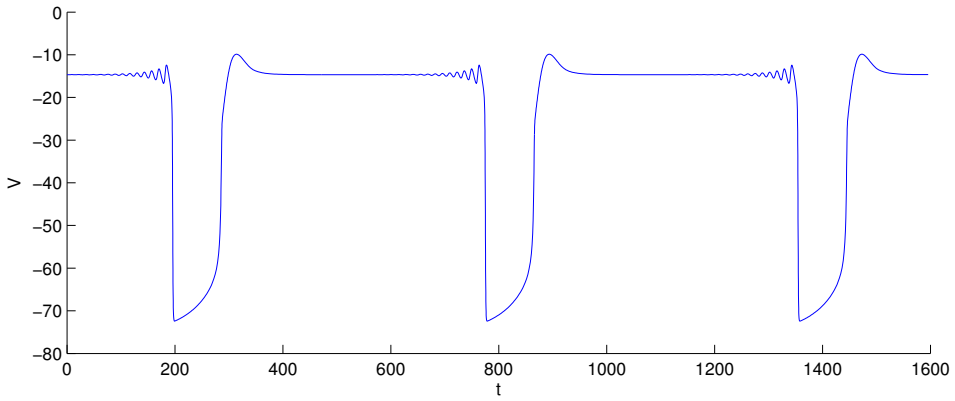

Figure 2.1: Mixed-mode oscillation in pituitary lactotroph model (4.1). Variable V corresponds to a membrane potential in the lactotroph cell.

Generating mechanisms for MMOs other than singular Hopf bifurcation have been found, see Desroches et al. [9] for an overview.

2.4 Interval analysis

Interval analysis was introduced by Moore in [49] as a method to use a digital computer to produce mathematically rigorous results with only approximate arithmetic. Tucker [63] is a modern introduction to the subject, and more advanced topics are discussed by Neumaier [53]. The main idea is to replace floating point arithmetic with a set arithmetic; the basic objects are intervals of points rather than individual points. Together with directed rounding, this method yields an enclosure arithmetic that allows for the rigorous verification of inequalities. Interval analysis thus accounts for both rounding and truncation errors. To use interval analysis to produce a mathematical proof, often

called *(auto-)validated numerical methods*, one has to prove that the statement at hand can be reduced to a finite number of inequalities, and then verify that these inequalities are satisfied. Interval arithmetic is used for the verification. The objects used to describe sets in validated numerics are typically convex sets in some coordinate system, e.g., intervals, parallelograms, or ellipsoids.

Interval analysis will be used in several ways in Chapter 5:

- *Interval arithmetic* is employed in many places, for instance to verify that a vector field is transverse to a given surface. Such computations can conveniently be performed using the MATLAB [73] toolbox INTLAB [76].
- *Automatic differentiation* is used to compute function derivatives rigorously, efficiently, and with high precision: in this set of techniques, the chain rule is applied mechanically until the derivative is expressed in terms of elementary functions, which in turn are evaluated using optimized interval-arithmetic algorithms. An introductory treatment of automatic differentiation can be found in [63], while [17] is an in-depth treatment of the automatic differentiation.
- Rigorous solutions to a differential equation are found using an *interval solver for initial value problems in ODEs*, which produces an enclosure for a trajectory segment of specified time length starting at a specified initial condition in which the trajectory segment is guaranteed to lie. In practice, points on the trajectory are usually found in a two-step process: to compute an interval enclosure of a new point on the trajectory, one first finds a rough enclosure of the trajectory up to the next time step and shows existence and uniqueness of the solution by verifying that the Picard-Lindelöf operator is a contraction. The second step then uses for example Taylor series to find a tight enclosure of the next point [50]. The software VNODE [78] used for the numerical integration in Chapter 5 is notably different

in that it is a two-step method but does not employ Taylor series.

- Covering relations with cone conditions are used to prove the existence of an unstable manifold in Section 5.6. A complete formal description of these concepts and methods can be found in [71, 70]. In [71] h-sets and covering relations are introduced, and in [70] the concept of an h-set with cones is introduced together with the appropriate modification to the definition of a covering relation. An *h-set* is a compact hyperbolic-like set, in the sense that it has expanding and contracting directions, in an appropriate coordinate system. An h-set is a set together with the coordinates. A map together with two h-sets, h_1, h_2, is said to satisfy *covering relations* if h_1 is mapped across h_2 under the map. Across in this setting means that the boundaries of h_1 transversal to the expanding directions are mapped outside h_2 and the image of h_1 does not intersect the boundaries of h_2 transversal to the contracting directions. Using the Brouwer degree, one can show, see [71], that a cycle of h-sets with covering relations must contain a periodic orbit. An *h-set with cones* is an h-set together with a quadratic form Q that describes a uniform cone field on the h-set. The map is said to satisfy *covering relations with cone conditions* if the quadratic form is increasing along orbits. Given recurrence, this yields uniqueness of periodic orbits. One can also use the *cone conditions*, see [70], to prove the existence of invariant manifolds and propagate them along orbits. The bounds on the location of the invariant manifolds given by covering relations with cone conditions are Lipschitz. In particular, around a fixed point one gets a cone which bounds the location of the invariant manifold. The Lipschitz constant depends on the ratio of the positive and negative eigenvalues of Q.

CHAPTER 3

SINGULAR HOPF NORMAL FORM BIFURCATION STRUCTURE

Bifurcation analysis of normal forms for higher codimension bifurcations provides a template that can be used to predict what types of subsidiary bifurcations occur as the normal form's parameters are varied. In this way, normal forms are powerful tools that provide insights into systems other than the normal form in which a given bifurcation occurs.

This chapter presents a detailed catalog of codimension-one bifurcations occurring in system (2.8), indicate where these bifurcations occur, and how these bifurcations change as additional parameters are varied. Our strategy is to do this in three stages, first examining a line in the parameter space parallel to the μ-axis, then a two-dimensional slice of the parameter space that varies (μ, A) and finally investigating how the bifurcations within this slice change as (B, C) is varied.

We regard μ as the *primary* bifurcation parameter and seek to determine the sequences of bifurcations of (2.8) that occur as μ varies while (A, B, C) remain fixed. This includes period-doubling bifurcations, folds of periodic orbits, Hopf bifurcations, homoclinic bifurcations, and a tangency of invariant manifolds, in which the two-dimensional unstable manifold of an equilibrium in the fold region intersects the repelling slow manifold tangentially. Section 3.1 presents the bifurcations and a sequence of phase portraits for the family with $(A, B, C) = (-0.05, 0.001, 0.1)$.

Section 3.2 studies how the bifurcations identified in Section 3.1 depend upon the parameter A with $(B, C) = (0.001, 0.1)$ remaining fixed. We present a detailed two-dimensional (μ, A) bifurcation diagram, showing a curve along which tangencies of invariant manifolds occur, bifurcations of the periodic orbit born in the singular Hopf

bifurcation, bifurcations of equilibrium points occurring close to the origin, and curves of homoclinic bifurcations. Canard explosions [13], in which periodic orbits that get extremely close to slow manifolds grow rapidly in size, occur near the homoclinic bifurcations. We discuss the codimension-two bifurcations that occur in this restricted two-parameter family. Due to the numerical problems associated with the large separations of time-scales for very small ϵ [9, 40], we computed the bifurcation curves of periodic orbits as well as the tangency curve in the bifurcation diagrams for values of ϵ in the range of approximately 10^{-2} and 10^{-4}. Section 3.3 describes how this (μ, A) bifurcation diagram of system (2.8) changes as (B, C) is varied and identifies codimension-three bifurcations. We show some topologically inequivalent (μ, A) diagrams in this section and give a larger portfolio in Appendix B. A table in Section 3.3 lists all the μ bifurcation sequences that we found. We observe that the position of a tangency of invariant manifolds is often related to the stability of the periodic orbit that bounds the unstable manifold involved in the tangency bifurcation: tangency bifurcations typically occur before or very close to where the periodic orbit bifurcates to become unstable.

Section 3.4 discusses a modification of the normal form (2.6) that makes the critical manifold S-shaped. Koper [38] introduced a model of chemical oscillations that is equivalent to a subfamily of the modified normal form. We investigate changes that occur in the bifurcation diagrams of (2.6) due to the modifications of the system, finding that bifurcations of structures located close to the origin persist and are perturbed only slightly. In the modified system, trajectories that jump from the vicinity of the origin approach another sheet of the critical manifold, flow along the associated attracting slow manifold to a fold and then jump back to the attracting slow manifold which comes close to the origin. This sequence of events constitutes a global return mechanism for trajectories to pass repeatedly near the origin. Mixed-mode oscillations [9] occur in this setting with small amplitude oscillations located in the vicinity of the origin and large

amplitude oscillations that follow the global returns. We use this example to illustrate how the table of bifurcation sequences from Section 3.4 can be used to estimate parameters that lie on the boundary of the parameter region for which mixed-mode oscillations are found.

Section 3.5 summarizes the results in Chapter 3 and discusses aspects of our analysis that remain incomplete. We provide a table listing all bifurcation labels used in this dissertation together with the full names of the bifurcations in Appendix A. Appendix B contains a portfolio of (μ, A) bifurcation diagrams for system (2.8). Appendix C contains supplementary data on the positions of codimension-three bifurcations in system (2.8). The positions of bifurcations of equilibria and periodic orbits, as well as positions of such objects in phase space were computed using the numerical continuation packages MatCont [77] and AUTO [74]. Analytic or asymptotic expressions for certain codimension-one and -two bifurcations of equilibria and periodic orbits discussed in Sections 3.2 and 3.3 match the numerical results wherever applicable. Appendix D comments on the numerical methods used for the computation of tangency of invariant manifold bifurcation curves.

3.1 Variations of the primary parameter

This section studies bifurcations and phase portraits of (2.8) that occur as μ is varied with $(A, B, C) = (-0.05, 0.001, 0.1)$ fixed. The values of these parameters are selected so that a stable equilibrium point, denoted E_f in this chapter, undergoes supercritical Hopf bifurcation. The distance from E_f to the origin is $O(\epsilon^{1/2})$. There are four bifurcations that we identify in the one-parameter family obtained from varying μ:

- Hopf bifurcation,
- Tangency of the unstable manifold of an equilibrium with the repelling slow manifold,
- Torus bifurcation of the periodic orbit,
- Period-doubling of the periodic orbit.

We present phase portraits that bracket each of the bifurcations to illustrate the changes that occur in the dynamics of this family as μ increases.

Guckenheimer [19] gives explicit formulas for Hopf bifurcation of (2.8) and its first Lyapunov coefficient. Here the Hopf bifurcation occurs for $\mu \approx 0.001246$. Figure 3.1 shows the attracting and repelling slow manifolds, denoted S_a and S_r throughout the chapter, and the one-dimensional strong stable manifold (black) of the equilibrium at a parameter $\mu = 0$ close to the Hopf bifurcation. S_a is drawn in red and magenta, with the top (red) half tending to E_f while the bottom (magenta) half flows to $X = -\infty$. The top half (cyan) of S_r consists of trajectories that flow from $X = -\infty$, while the bottom half (blue) consists of trajectories that originate close to one branch of the strong stable manifold of the equilibrium. The existence of locally invariant slow manifolds of singularly perturbed systems that lie within distance $O(\epsilon)$ from normally hyperbolic critical manifolds was proved by Fenichel [15]. Attracting manifolds have fast foliations consisting of trajectories that approach each other in forward time; repelling manifolds have fast foliations consisting of trajectories that approach each other in backward time. As ϵ tends to zero, the flow on the slow manifolds approaches the flow of the reduced system. Since we have a single fast variable, the slow manifolds are either attracting or repelling. Extensions of these manifolds to the vicinity of the fold curve intersect one another. Detailed analyses of such intersections near folded saddles and folded nodes were performed by Benoit [3], Szmolyan and Wechselberger [59], Wechselberger [66], Guck-

enheimer and Haiduc [20], Desroches et al. [11] and Krupa and Wechselberger [42]. S_r separates trajectories in the basin of attraction of E_f from trajectories that flow to infinity in forward time.

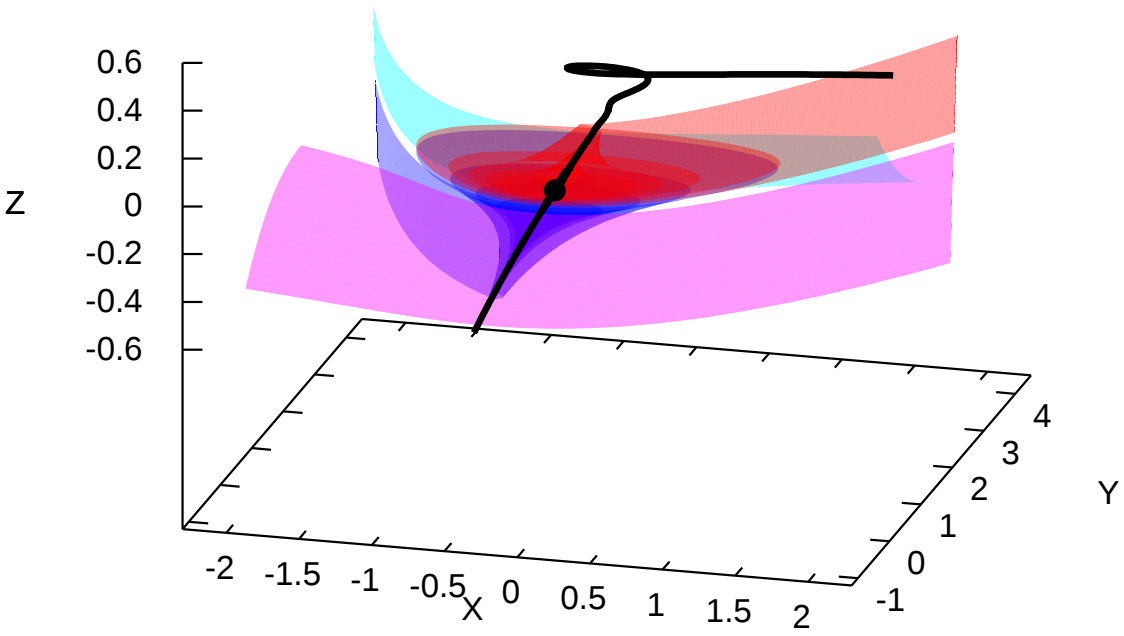

Figure 3.1: Phase space of system (2.8) when $(\mu, A, B, C) = (0.0, -0.05, 0.001, 0.1)$. The system has an attracting equilibrium with a complex eigenvalue pair at $(X, Y, Z) = (0, 0, 0)$. Two trajectories tending to the equilibrium along the strong stable eigendirections are drawn as black curves. Parts of S_r that approach the stable manifold of the equilibrium or escape to $X = \infty$ as $t \to -\infty$ are shown in blue and cyan respectively. Parts of S_a that approach the equilibrium or tend to $X = -\infty$ as $t \to \infty$ are shown in red and magenta respectively.

Figure 3.2 displays the phase portrait for $\mu = 0.0012715$. The equilibrium point E_f has become a saddle-focus with a two-dimensional unstable manifold $W^u(E_f)$ (red) whose boundary is the stable periodic orbit Γ (green) born at the Hopf bifurcation. Trajectories in the one-dimensional stable manifold $W^s(E_f)$ are plotted in black. As

μ increases, Γ and $W^s(E_f)$ grow in size, getting close to the slow manifolds. At $\mu = 0.0014975$, they come close to touching tangentially as illustrated in Figures 3.3 and 3.4. The multipliers of Γ have become complex, but they still have magnitude smaller than one. Note from Figure 3.4 that $W^u(E_f)$ forms a "scroll" which gets much closer to S_r than Γ does.

S_r and $W^u(E_f)$ begin to intersect transversely at approximately $\mu = 0.00156$. This results in bistability for $W^u(E_f)$: some trajectories escape to $X = -\infty$, while others remain in the fold region, and oscillate while approaching Γ, which still has complex attracting multipliers (see Figure 3.5).

Figure 3.6 shows a phase portrait where $\mu = 0.0017533$. Almost all trajectories in $W^u(E_f)$ appear to leave the fold region, tending towards $X = -\infty$, with some trajectories following S_r for extended periods of time on their last turn before leaving the fold region. $W^u(E_f)$ is no longer the boundary of the basin of attraction of Γ, which remains attracting with complex multipliers. Note the transverse intersection of $W^u(E_f)$ and S_r.

Γ undergoes a torus bifurcation at $\mu = 0.0017829$, in which its stability changes from complex attracting to complex repelling, and an invariant torus appears around it (see Figure 3.7). While numerical computations suggest that at this parameter almost every trajectory in $W^u(E_f)$ tends to $X = -\infty$, the position of the torus and the dynamics close to it may still have an impact on how many "turns" trajectories make before exiting the fold region. The invariant torus only exists over a short parameter range: at $\mu = 0.0017880$, trajectories in the unstable manifold of Γ diverge to $X = -\infty$.

We note that the multipliers of Γ become real repelling for larger values of μ, before Γ undergoes a period-doubling bifurcation at approximately $\mu = 0.0021910$ (see Figure 3.8 for a phase portrait just after the period-doubling).

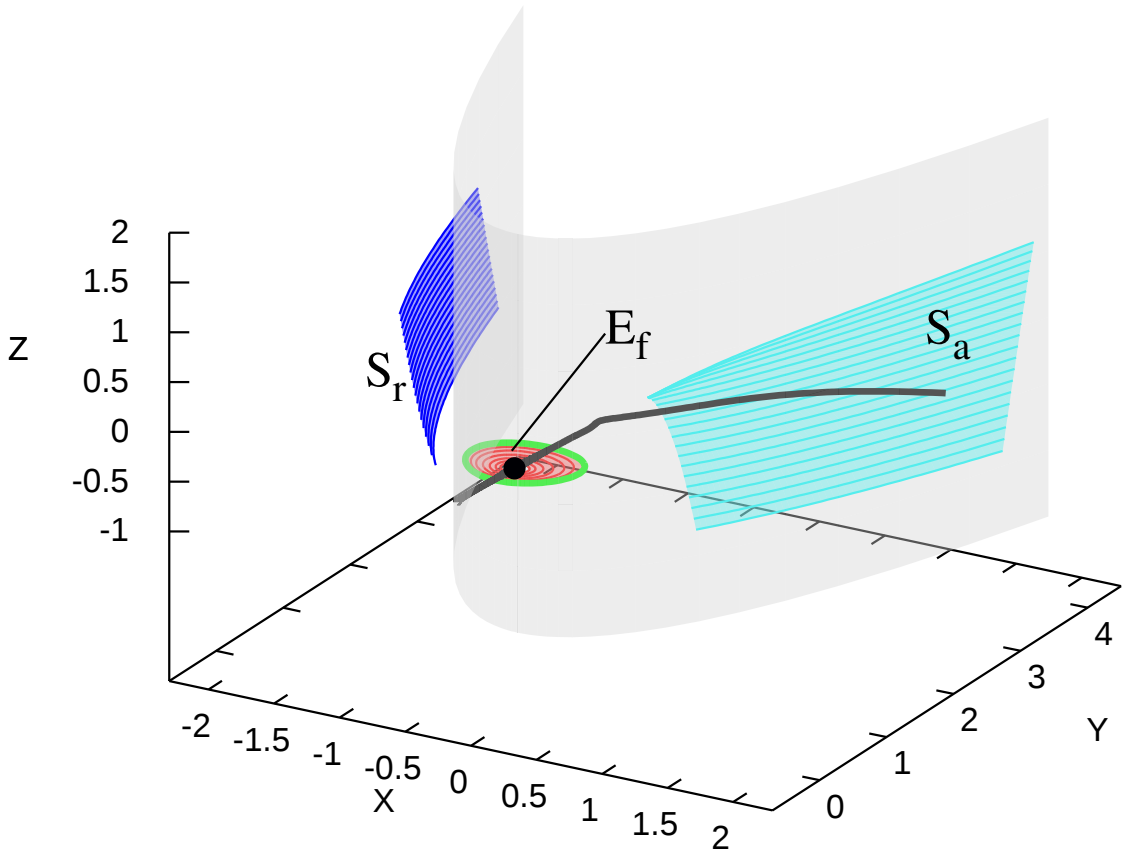

Figure 3.2: Phase space of system (2.8) when $(\mu, A, B, C) = (0.0012715, -0.05, 0.001, 0.1)$. The critical manifold has the shape of a parabolic sheet and is plotted in gray. Subsets of S_a and S_r are shown in cyan and blue respectively. The black dot marks the position of E_f. Its two-dimensional unstable manifold $W^u(E_f)$ is plotted as a red surface, with a part close to the equilibrium removed. The singular Hopf periodic orbit is shown as a green curve. The stable manifold $W^s(E_f)$ of the equilibrium E_f is drawn as a black curve, it leaves the fold region in reverse time: one branch follows S_r and the other remains close to S_a for a while.

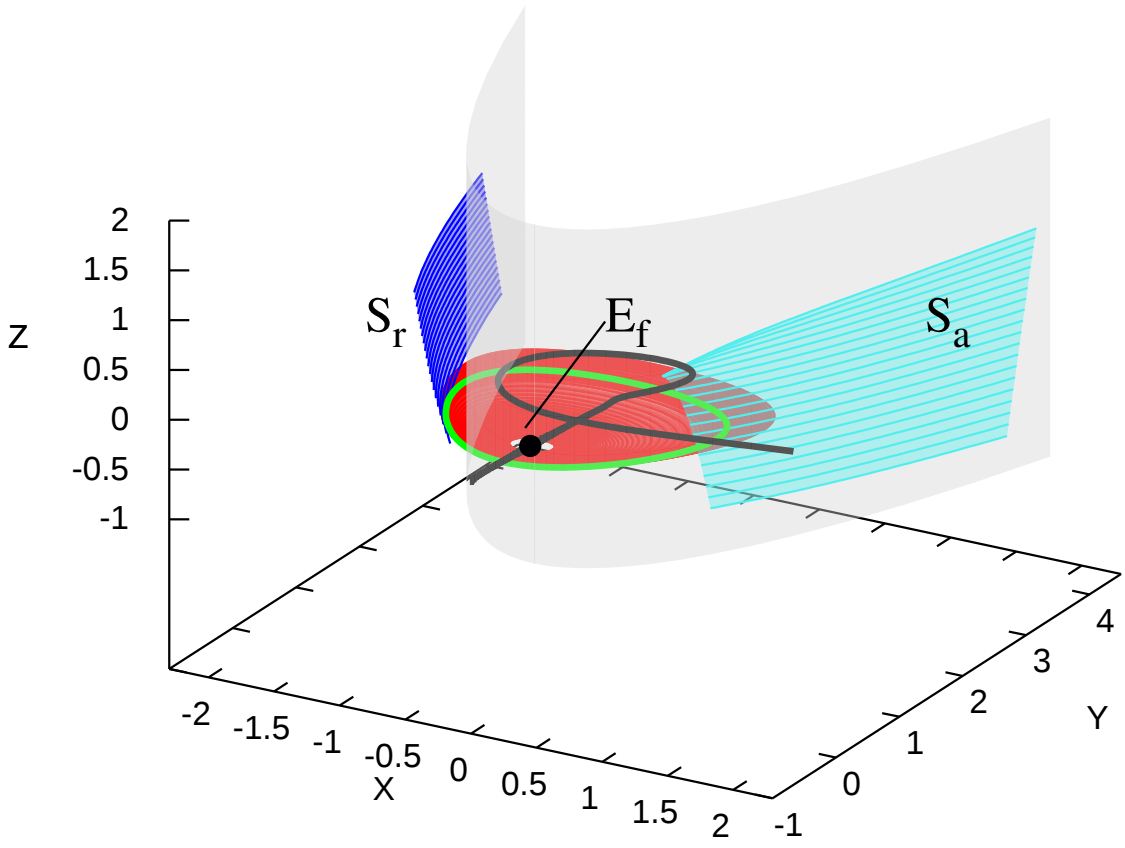

Figure 3.3: Phase space of system (2.8) when $(\mu, A, B, C) = (0.0014975, -0.05, 0.001, 0.1)$, showing the same objects as Figure 3.2, with the same color coding. The position of the "top" part of $W^s(E_f)$ changed considerably with respect to Figure 3.2. This is to be expected, since the S_a is repelling in reverse time.

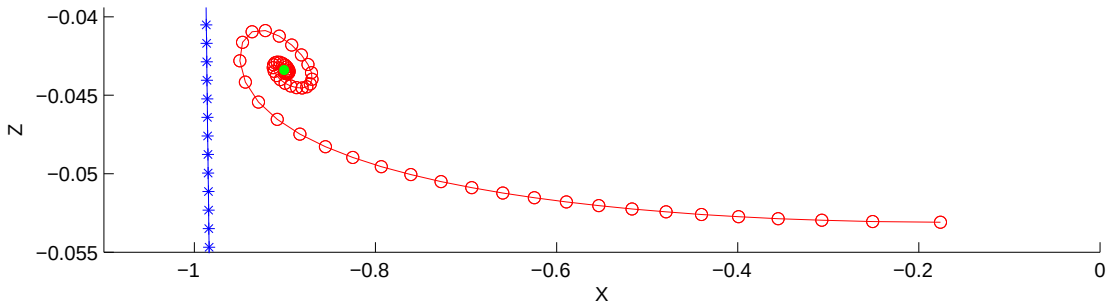

Figure 3.4: Objects in phase space crossing the plane $Y = 0.5$ at $(\mu, A, B, C) = (0.0014975, -0.05, 0.001, 0.1)$: a selection of trajectories in S_r are plotted using blue stars, connected with straight lines. The green dot shows the position of the stable periodic orbit's intersection with the plane with $\dot{Y} > 0$. The red circles, also connected by straight lines, represent intersections of a single trajectory in $W^u(E_f)$ with the plane with $\dot{Y} > 0$.

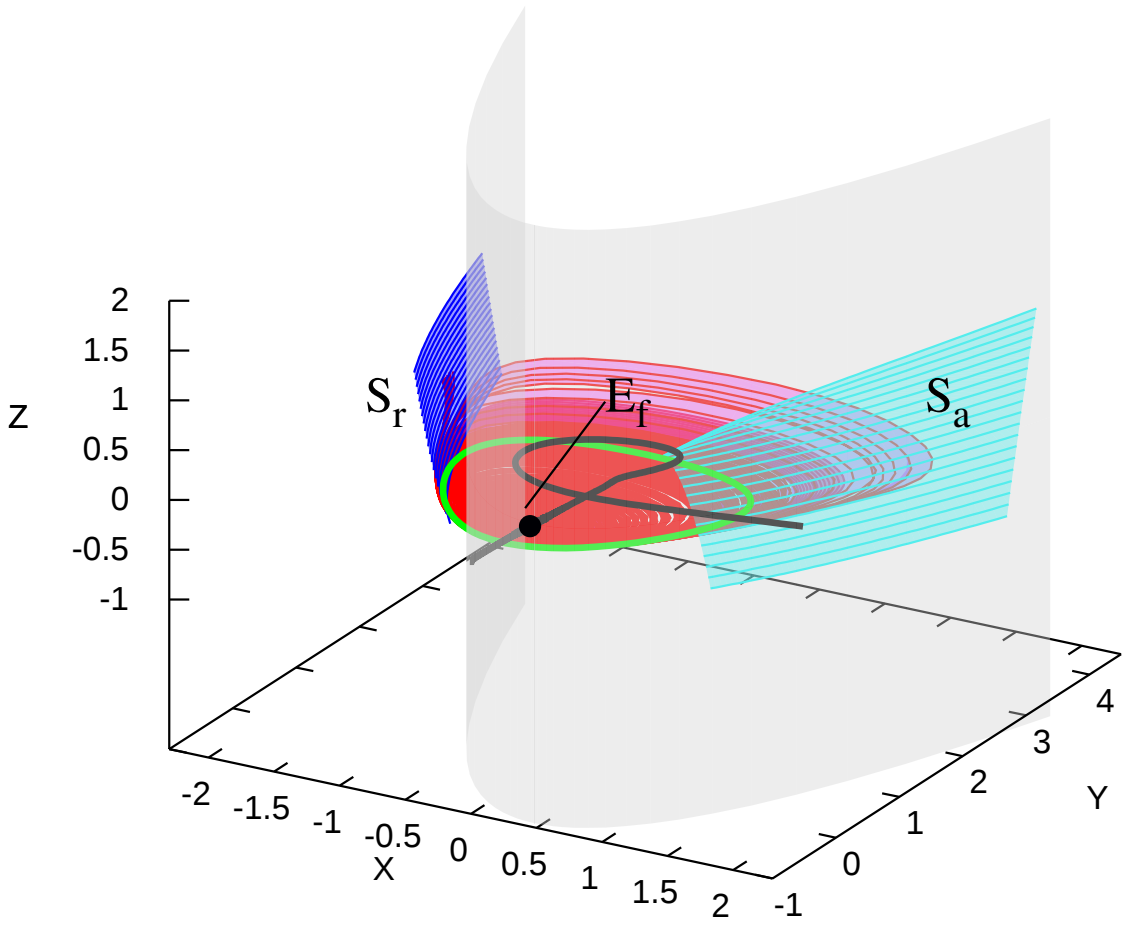

Figure 3.5: Phase space of system (2.8) when $(\mu, A, B, C) = (0.0015709, -0.05, 0.001, 0.1)$. In contrast to previous figures, parts of the unstable manifold of the equilibrium $W^u(E_f)$ near the origin are colored in red and magenta, distinguishing the trajectories that escape to $X = -\infty$ from those that are attracted to the periodic orbit.

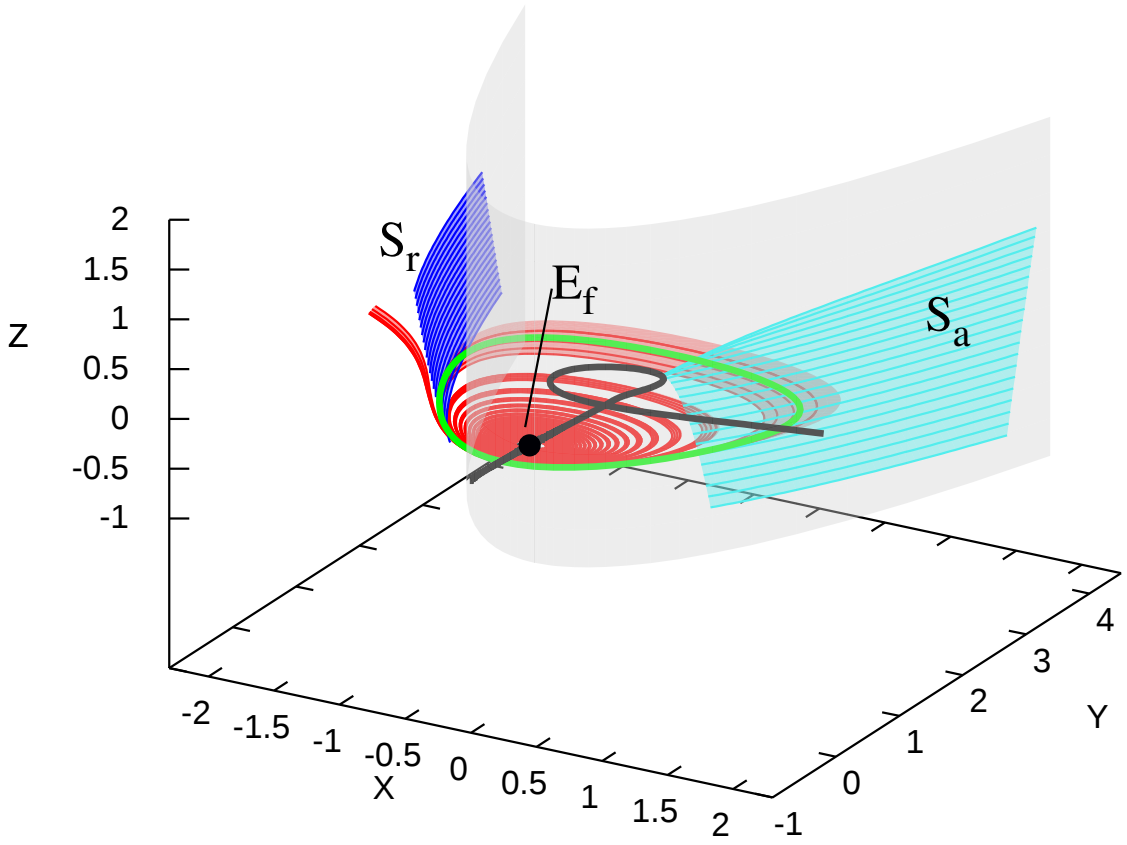

Figure 3.6: Phase space of system (2.8) when $(\mu, A, B, C) = (0.0017533, -0.05, 0.001, 0.1)$. The color coding is as in Figure 3.2, but here only a part of one fundamental domain of $W^u(E_f)$ is shown.

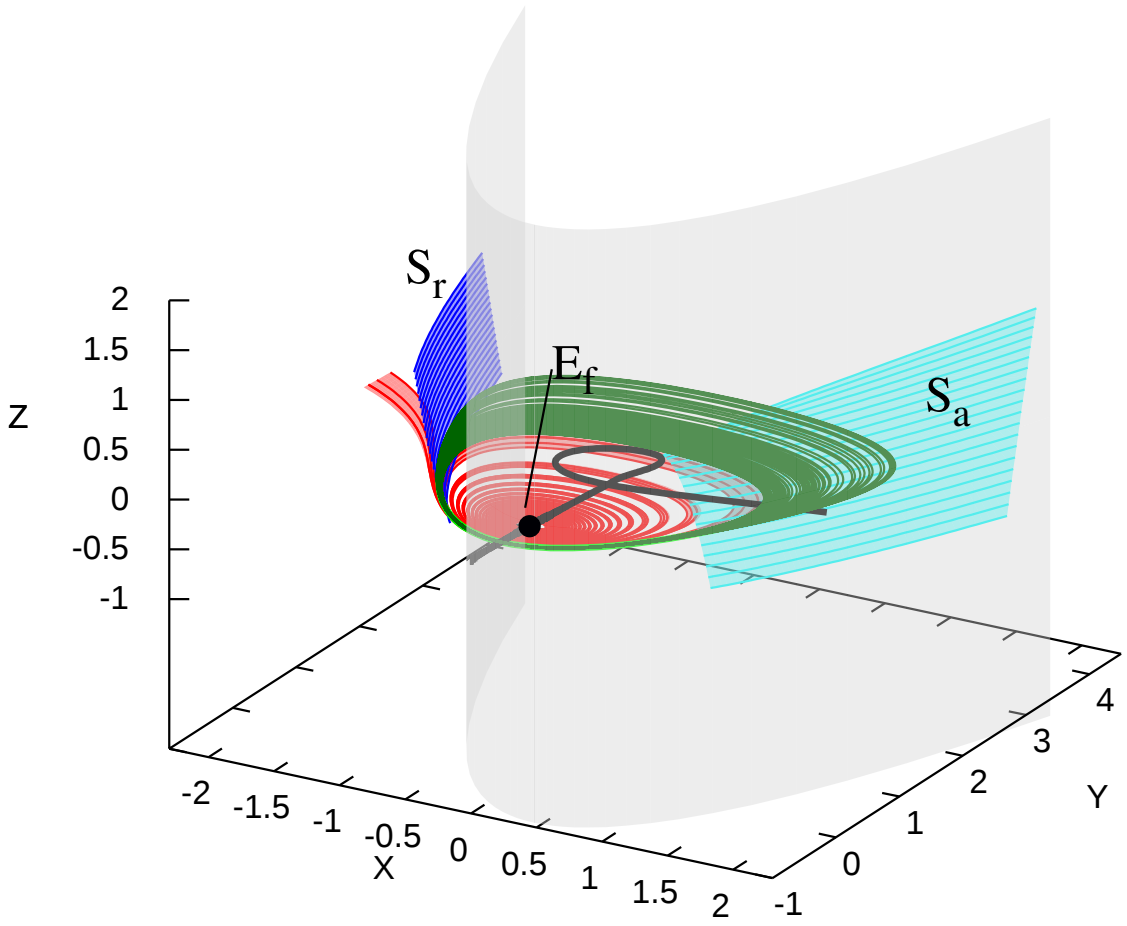

Figure 3.7: Phase space of system (2.8) when $(\mu, A, B, C) = (0.0017846, -0.05, 0.001, 0.1)$. A segment of a trajectory on the invariant torus is drawn as a dark-green line. Otherwise, the color coding is as in the previous figure. The periodic orbit is largely obscured by the torus.

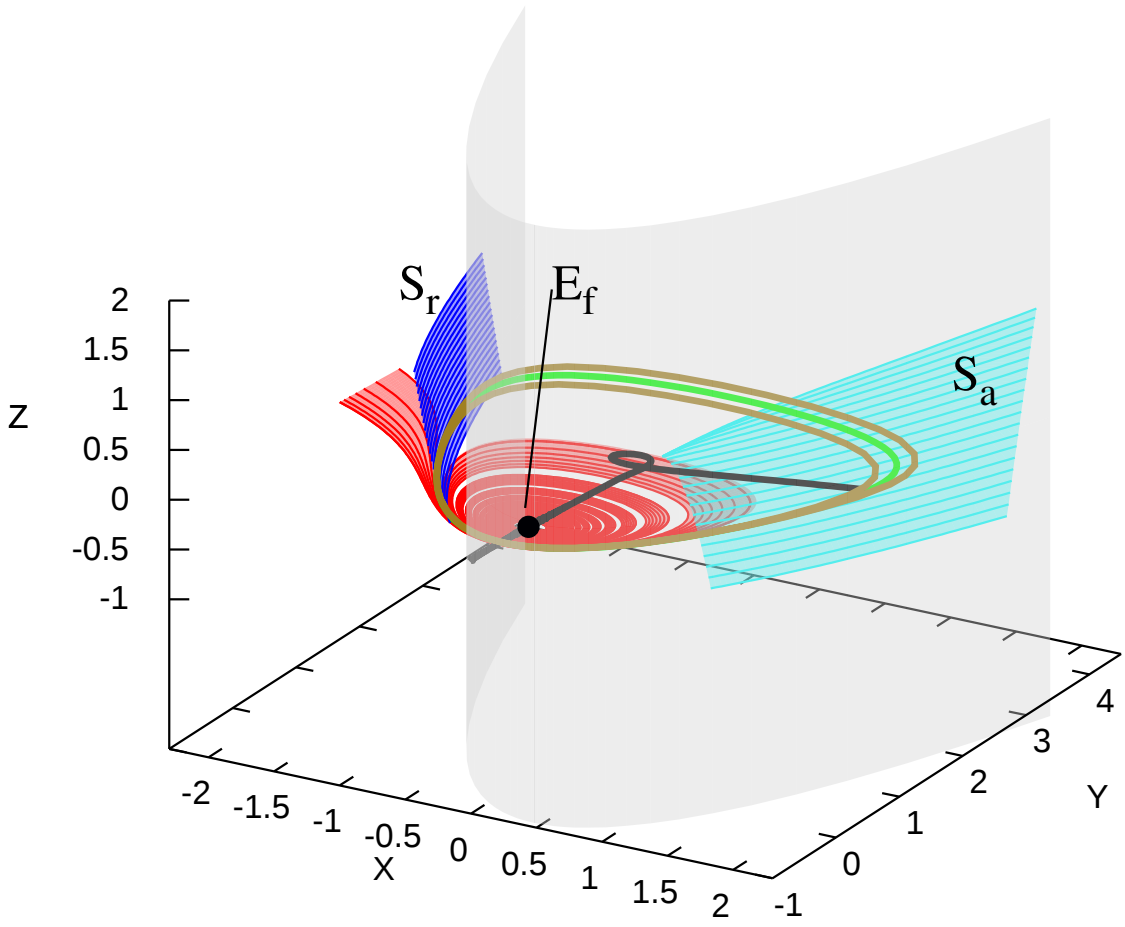

Figure 3.8: Phase space of system (2.8) when $(\mu, A, B, C) = (0.0022000, -0.05, 0.001, 0.1)$. A period-doubled periodic orbit is plotted with an olive thick line. The color coding for the other periodic orbit, the slow manifolds, critical manifold, and invariant manifolds of the equilibrium near the origin is as in the earlier figures. A part of the unstable manifold of the equilibrium near the origin not plotted here comes very close to the period-doubled periodic orbit.

3.2 Bifurcation structure of a two-dimensional parameter slice $(B, C) = (0.001, 0.1)$

This section describes the two-dimensional bifurcation diagram of system (2.8), with parameters $(B, C) = (0.001, 0.1)$ fixed and (μ, A) varying. The diagram in Figure 3.9 is typical in the sense that all other generically occurring (μ, A) diagrams share many of its codimension-one and -two phenomena and bifurcations. The codimension-one bifurcations with the symbols that label them in Figure 3.9 are

- saddle-node bifurcation (SN)
- (singular) Hopf bifurcation (Hopf)
- period-doubling bifurcations (PD)
- fold of periodic orbit bifurcations (LPC)
- torus bifurcations (NS)
- tangency of invariant manifolds (T)
- canard explosions ending in homoclinic bifurcations (S)

The codimension-two bifurcations are

- resonances of periodic orbits (R1,R2,R3,R4)
- degenerate homoclinic bifurcations (P)
- zero Hopf bifurcations (ZH)
- generalized Hopf bifurcations (GH)

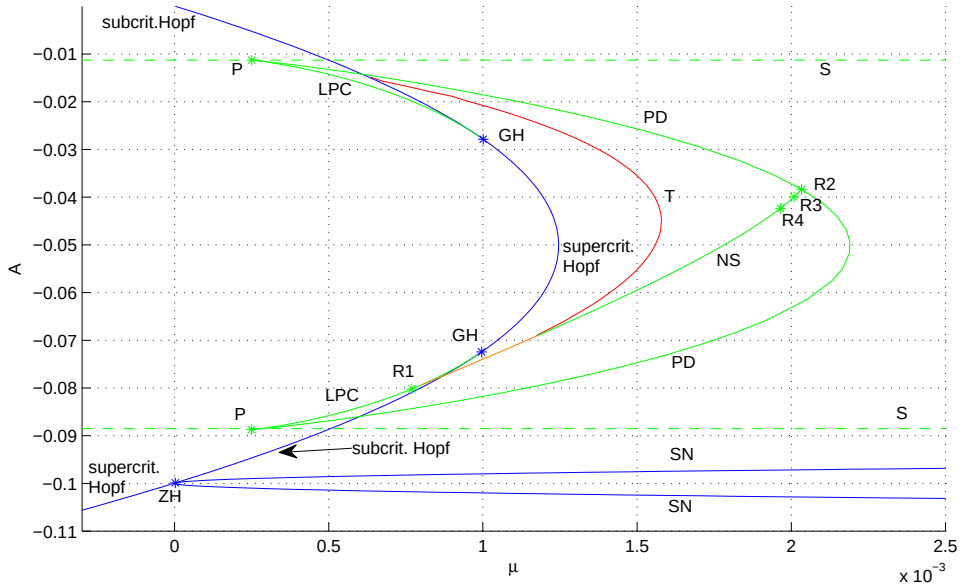

Figure 3.9: (μ, A) bifurcation diagram for system (2.8) with $(B, C) = (0.001, 0.1)$.

We briefly discuss each of these bifurcations in turn.

Saddle-node bifurcation. Recall that we assume that A and C are $O(\epsilon^{1/2})$ and that B is $O(\epsilon)$. System (2.8) can have up to two equilibria. There is only one equilibrium point near the origin unless $A + C = O(\epsilon)$, in which case there are two. There is a saddle-node bifurcation (labeled SN in the diagrams) at $\mu = (A+C)^2/(4B)$ and $(X, Y, Z) = (X_e, X_e^2, X_e)$ with $X_e = (A + C)/2B$. The solution curve of $\mu = (A + C)^2/(4B)$ bounds a thin region of parameters where no equilibria exist.

Hopf bifurcation and its codimension-two degeneracies. The formulas for Hopf bifurcation loci in the fold region and its codimension-two degeneracies are complicated expressions, and are best understood by disregarding terms that are of higher

order in ϵ. For all $B \neq 0$, the system has only one Hopf bifurcation that occurs at O(1) distance from the origin, occurring at $\mu = -A^2/2 - AC/2 + O(\epsilon^{3/2})$ and $(X, Y, Z) \approx (A/2, A^2/4, A/2) + O(\epsilon^{1/2})$, making it a singular Hopf bifurcation. The Hopf bifurcation is degenerate at a zero Hopf bifurcation (marked ZH in the diagrams), where the Hopf equilibrium point has a zero eigenvalue in addition to the purely imaginary eigenvalue pair, and at two generalized Hopf bifurcations (GH), where the first Lyapunov coefficient vanishes. The Hopf center manifold is attracting for values of A greater than that of the zero Hopf bifurcation, and repelling for values of A smaller than that of the zero Hopf bifurcation. The criticality of the Hopf bifurcation changes at each of these codimension-two degeneracies. Supercritical [subcritical] Hopf bifurcations at values of A greater than that of the ZH bifurcation give rise to periodic orbits when the Hopf curve is crossed with μ increasing [decreasing], while at smaller values of A supercritical [subcritical] Hopf bifurcations give rise to periodic orbits as the Hopf curve is crossed with μ decreasing [increasing].

Period-doubling bifurcations. Numerical continuation with MatCont [77] and AUTO [74] show that Γ undergoes a period-doubling bifurcation (labeled PD in bifurcation diagrams) as μ is increased. In the rescaled system (2.8), these bifurcations typically occur on periodic orbits that are $O(1)$ distant from the origin. Near the endpoints of the period-doubling bifurcation curve, where the PD curve meets a homoclinic bifurcation, the amplitude becomes even larger and the bifurcating orbits of system (2.6) no longer shrink to the origin as $\epsilon \to 0$. This degeneracy is described further in the paragraph on "Degenerate homoclinic bifurcations" below.

Fold of periodic orbits bifurcations. A fold of periodic orbits bifurcation curve (labeled LPC) emanates from each of the generalized (singular) Hopf bifurcations (GH). This bifurcation, in which two periodic orbits annihilate each other as μ decreases, is initially local to the origin in system (2.8), but later becomes non-local in a canard explosion, and ends where the LPC curve meets a homoclinic bifurcation (see the paragraph on "Degenerate homoclinic bifurcations" for more details).

Torus bifurcations. A locus of torus bifurcations (NS) emanates from the zero Hopf bifurcation (ZH). Associated with this are attracting invariant tori that surround the bifurcating singular Hopf periodic orbit. These tori apparently exist only in a thin strip of parameters to the right of the torus bifurcation curve.

Tangency of invariant manifolds. In Figure 3.9, E_f has a two-dimensional unstable manifold in the parameter region bounded below by the saddle-node curve, and on the left by the Hopf curve. In part of this region, $W^u(E_f)$ intersects S_r. This intersection is tangential at the tangency curve (T), where the manifolds begin to intersect as μ increases. Note that there are values of A where the manifolds intersect immediately after the Hopf bifurcation. See appendix D for details on the computation of the tangency curve.

Canard explosions and homoclinic bifurcations. The periodic orbit Γ grows rapidly in canard explosions. The canard explosions consist of periodic orbits that have long segments lying near S_r. The small parameter ranges in which they occur are determined by the geometry of the slow flow as illustrated in Figure 3.10. The slow flow is computed by differentiating the equation of the critical manifold in system (2.6) with

respect to t, and using the result and the equations for the derivatives of the slow variables to obtain equations for $\dot{x}$ and $\dot{z}$ in x and z only. After rescaling the vector field so that the direction reverses on the repelling sheet of the critical manifold, we obtain the following desingularized slow flow equations:

$$\begin{aligned} x' &= z - x \\ z' &= -2x\,(\mu + ax + bx^2 + cz) \end{aligned} \tag{3.1}$$

Trajectories that follow S_r can jump at any location along the manifold. The singular limit of trajectories of system (2.6) approach concatenations of trajectories of the slow flow together with segments parallel to the x-axis that begin on the repelling sheet of the critical manifold and end on the attracting sheet of the critical manifold. Since the critical manifold is a parabolic cylinder symmetric with respect to reflection in the (y, z) plane, the singular limits of some periodic orbits consist of trajectories of the slow flow that connect points (x, z) to points $(-x, z)$ concatenated with the horizontal segment from $(-x, z)$ to (x, z). We call these periodic orbits with a single fast segment *simple*. We refer to their singular limits as singular cycles.

We expect the simple periodic orbits to grow rapidly where the slow flow equations satisfy

$$\frac{\dot{z}(x, z)}{\dot{x}(x, z)} \approx -\frac{\dot{z}(-x, z)}{\dot{x}(-x, z)}.$$

With the simplifying assumption $\mu = 0$, substitution of the slow flow equations into the ansatz gives that when $\mu = 0$, canard explosions are likely to occur at parameters satisfying

$$a^2 + ac + b = 0, \tag{3.2}$$

and that the trajectory segments on the slow manifolds of system (2.8) can approximately be parametrized by $(X, Y, Z) = (X, X^2, AX^2)$. Note that $\epsilon(a^2+ac+b) = A^2+AC+B$ in the rescaling from system (2.6) to system (2.8). Numerical calculations with MatCont

and AUTO show that these estimates are very accurate, and that the location of periodic orbits is insensitive to the small value of μ. In Figure 3.9, canard explosions occur along lines that are nearly horizontal, and end in homoclinic bifurcations with equilibria that are far from the origin. Dashed green lines labeled S are drawn in Figure 3.9 at $A = \sqrt{C^2 - 4B}$ as approximations to the region where the slow flow has singular cycles.

Resonances of periodic orbits. There are 1:1, 1:4, 1:3 and 1:2 resonances on the torus bifurcation curve (labeled R1, R4, R3 and R2 respectively), where Γ has multipliers on the unit circle with arguments $0, \pi/4, \pi/3$ and $\pi/2$ respectively. At the 1:1 resonance, the torus bifurcation curve ends at a fold of periodic orbits bifurcation locus in a bifurcation that is analogous to the Bogdanov-Takens bifurcation for two-dimensional vector fields [61, 21]. At the 1:2 resonance, the torus bifurcation curve ends at the period-doubling curve in another bifurcation analogous to the Bogdanov-Takens bifurcation with symmetry [61, 21].

Degenerate homoclinic bifurcations. The homoclinic bifurcation is degenerate at two points, labeled P in the (μ, A) bifurcation diagrams. At each of these points, a fold of periodic orbits curve (LPC) and a period-doubling curve (PD) meet the curve of homoclinic bifurcations. We believe that these codimension-two phenomena are due to homoclinic orbit flips (top point) and homoclinic inclination flips (lower point). Unfoldings of these bifurcations were developed by Sandstede [57] (orbit flip) and Homburg et al. [29] (inclination flip) and Kisaka et al. [36, 37] (inclination flip). We did not investigate the points P in detail.

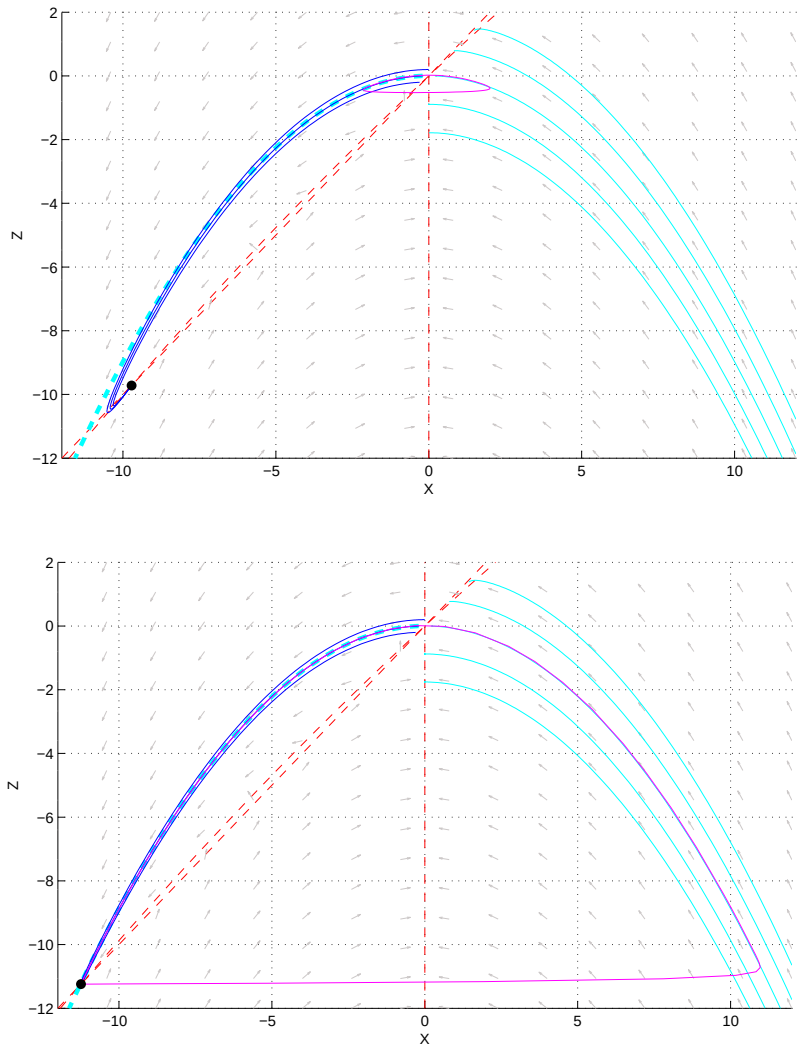

Figure 3.10: Phase portraits for system (2.8) for parameters $(\mu, A, B, C) = (2.5008 \times 10^{-6}, -0.090281, 0.001, 0.1)$ (top) and $(\mu, A, B, C) = (2.5008 \times 10^{-6}, -0.088758, 0.001, 0.1)$ (bottom), showing the projection of a periodic orbit (magenta, computed in the full system with MatCont) onto the slow flow. The nullclines of the slow flow as well as the fold curve are drawn using red dashed lines. Segments of trajectories of the slow flow are plotted in blue and cyan, the two middle ones ending at the origin. A reflection of the middle cyan trajectory about the Z axis is plotted as a dashed cyan line. The position of the equilibrium far from the origin on the repelling sheet of the critical manifold is marked with a dot.

3.3 Catalog of bifurcation diagrams in one and two-dimensional parameter slices

This section first describes curves of codimension-one bifurcations in (μ, A) bifurcation diagrams for different fixed values of (B, C). This includes information about the codimension-two bifurcations at which codimension-one bifurcation curves meet or end. We then complete our study of the bifurcations of system (2.8) by investigating how the (μ, A) bifurcation diagrams change as B and C vary. These changes occur when we encounter points of codimension larger than two and when we encounter intersections of the loci of codimension-one and -two bifurcations that are not transverse. Most of the changes we find are of the latter type. Indeed, we identify here only a single degeneracy of the first type, which occurs when $B = 0$.

Equilibrium point bifurcations. Unless $B = 0$, system (2.8) has a saddle-node bifurcation at $\mu = (A + C)^2/(4B)$, whose properties are described in Section 3.2. Similarly, there is only one curve of local Hopf bifurcations for $B \neq 0$, occurring at $\mu \approx -A^2/2 - AC/2 + O(\epsilon^{3/2})$. It is degenerate at a zero Hopf (ZH) bifurcation at $A = C(B - 1)$. A computation of the normal form coefficients using notation from Kuznetsov [44] shows that if $B < 0$, then $s = 1$, $\theta < 0$, and the system has homoclinic orbits, invariant tori, and invariant spheres, which are local in the vicinity of the zero Hopf bifurcation. If $B > 0$, then $s = 1$, $\theta > 0$, and the dynamics in the vicinity of the zero Hopf bifurcation is simpler.

The Hopf bifurcation is also degenerate at generalized Hopf bifurcations (GH), where the first Lyapunov coefficient vanishes. Simplifying the expression for the first

Lyapunov coefficient by eliminating terms that are of higher order in ϵ, we observe that there are generalized Hopf bifurcations approximately when $A^2 + AC + 2B = 0$ has a real solution, i.e. whenever $C^2 - 8B \geq 0$. We note that equilibrium points at $O(1/\epsilon)$ distance from the origin can undergo Hopf bifurcation as well.

Periodic orbit bifurcations. Period-doubling bifurcations (PD) exist in those (B, C) regions where the slow flow has singular cycles. The bifurcation loci begin and end at points labeled P, where the periodic orbit that is to double undergoes a canard explosion. At these points, the period-doubling bifurcation curve meets a fold of periodic orbits curve, in what seems to be a tangential way. The period-doubling occurs as μ increases through the bifurcation parameter value, and the first period-doubling bifurcation may be followed by further period-doublings. Fold of periodic orbits (LPC) curves exist in those (B, C) regions where the slow flow has singular cycles. There is one fold of periodic orbits curve if no generalized Hopf bifurcation is present, and the bifurcation curves begin and end at meeting points labeled P, where they connect with period-doubling bifurcations. If two generalized Hopf bifurcations are present, then the fold of periodic orbits curves begin at generalized Hopf bifurcations, and end at points marked P. Given (B, C), the sign of B determines whether the LPC curve lies to the left ($B > 0$) or to the right ($B < 0$) of the Hopf bifurcation curve. Canard explosions of the slow flow occur for parameters near those that satisfy $A^2 + AC + B = 0$ where the slow flow has singular cycles. These canard explosions typically end in homoclinic bifurcations with equilibrium points that are at $O(\epsilon)$ distance from the origin. Being non-local in many cases, we did not investigate homoclinic bifurcations thoroughly and plot homoclinic bifurcation curves only in figure B.1 which gives the (μ, A) bifurcation diagram for $(B, C) = (-0.01, 0.1)$.

Invariant tori exist close to the torus bifurcation curves marked NS. If $B < 0$, normal form theory predicts that these tori are unstable close to the zero Hopf bifurcation [44], and exist for values of A greater than that of the torus bifurcation curve. A more detailed analysis of the stability and persistence of the torus bifurcations was not performed. When $B < 0$, the torus bifurcation curve starts at the zero Hopf bifurcation, and ends at a 1:2 resonance (labeled R2), where it meets the period-doubling curve. The torus bifurcation curve intersects no other bifurcation curves included in the diagrams. The defining equation that characterizes torus bifurcations is also satisfied by "neutral" periodic orbits with two multipliers whose product is one. Consider first parameters (B, C), $B > 0$ for which there is no generalized Hopf bifurcation. A curve $L_{(B,C)}$ of neutral periodic orbits emanates from the Hopf bifurcation. This curve is shown in Figure B.10, but is omitted in all other bifurcation diagrams. Close to the zero Hopf bifurcation, the multipliers are real, and the periodic orbits are saddles. The curve $L_{(B,C)}$ can intersect the period-doubling bifurcation curve in 1:2 resonances or meet a fold of periodic orbits bifurcation curve tangentially in 1:1 resonances where the multipliers become complex. Both events can occur more than once in the same (μ, A) diagram, due to bending of the curve $L_{(B,C)}$, see e.g. Figure B.8 for two 1:2 resonances. If there is a generalized Hopf bifurcation and $B > 0$, then there is typically one curve of torus bifurcations, beginning at a fold of periodic orbits bifurcation at a 1:1 resonance, and ending at an intersection with a period-doubling bifurcation curve at a 1:2 resonance. Independent of whether a generalized Hopf bifurcation is present or not, when $B > 0$ and $C > 0$, as the absolute value of C decreases towards the parameter $C = C(B)$ where an isola vanishes, the curve $L_{(B,C)}$ tends to move along the families of periodic orbits, from the singular Hopf bifurcation towards and beyond the period-doubling bifurcation. See Figures B.3 to B.10 for a sequence of diagrams illustrating this trend. If $B > 0$ and $C < 0$, then the families of periodic orbits are traversed away from the Hopf bifurcation as C increases towards the

point where the isola vanishes.

Tangency of invariant manifolds. We now discuss intersections of $W^u(E_f)$ with S_r. Regions in parameter space where these manifolds intersect are separated from those where they do not intersect by tangencies of invariant manifolds as well as by three codimension-one bifurcations: saddle-node bifurcations, Hopf bifurcations, and fold of periodic orbits bifurcations. The tangency curve is in many cases very close to torus bifurcations or period-doubling bifurcations, to the point of being indistinguishable from these bifurcation curves in some of the (μ, A) bifurcation diagrams. Nonetheless, the tangency of invariant manifolds is a bifurcation in its own right, and does not coincide with period-doubling or torus bifurcations in system (2.8) except at isolated points of the (μ, A) diagrams.

The tangency curve is situated in the (μ, A) diagrams in different ways for $B > 0$ and $B < 0$. If $B < 0$, E_f leaves an $O(1)$ neighborhood of the origin in system (2.8) when $A + C = O(\epsilon)$ with $A + C < 0$. The tangency curve begins at the saddle-node curve at a value of A slightly more negative than that of the zero Hopf bifurcation, indistinguishably close in most of the diagrams of this chapter and Appendix B. In this region of parameter space, $W^u(E_f)$ may approach the one-dimensional stable manifold of the second equilibrium in the vicinity of the origin and then leave the fold region, or can "get caught" in invariant structures around the two equilibrium points involved in the zero Hopf bifurcation, cf. [44] Figure 8.22. The tangency curve may intersect the PD curve, but systematic numerical computations suggest that the tangency curve does not lie visibly to the right of it at the resolution of the (μ, A) bifurcation diagrams included in this dissertation. The tangency curve ends at the top point P, where the boundary of the region with an intersection of invariant manifolds begins to coincide with the fold

of periodic orbits bifurcation curve, and the intersection begins to be transverse at the boundary parameters.

If $B > 0$, there is a saddle-focus in the vicinity of the origin in the region $R_{(B,C)}$ that lies to the right of the Hopf curve and above the saddle-node curve. If now $C < 0$, then $W^u(E_f)$ and S_r intersect transversely in the entire region $R_{(B,C)}$. If $C > 0$, then in some parts of the region $R_{(B,C)}$ the two invariant manifolds do not intersect. More precisely, there is a tangency curve, beginning on the Hopf bifurcation curve, very close to the torus bifurcation curve or at a larger value of A, lying to the right of the Hopf curve until it meets the Hopf curve again at a larger value of A, very close to the period-doubling curve or at a smaller value of A. The tangency curve can intersect the torus and period-doubling curves for large enough values of $C = C(B)$, and there may be interactions between $W^u(E_f)$ and the attracting tori for (μ, A) slightly below the torus bifurcation curve. Systematic numerical computations suggest that the tangency curve does not lie visibly to the right of the period-doubling curve at the resolution of the (μ, A) bifurcation diagrams included in this chapter and Appendix B. It never lies much to the right of the torus bifurcation curve either, see Figure B.6 for a case in which the tangency curve lies visibly to the right of the torus bifurcation curve.

Remark: local and non-local bifurcations. The bifurcations described above are, with two exceptions, local to the origin in system (2.8). The first exception is the saddle-node bifurcation (labeled SN), which is local in the vicinity of the zero Hopf bifurcation (ZH), but is generally non-local. Note also that the range of values of A for which saddle-node bifurcations occur for (B, C) fixed and $\mu = O(\epsilon)$ is $O(\epsilon)$, while most other codimension-one bifurcations are of interest over an $O(\epsilon^{1/2})$ range of A. The second exception is that the periodic orbit Γ can become non-local at parameters close to the

horizontal dashed green lines in the (μ, A) bifurcation diagrams where the slow flow has singular cycles. In particular, period-doubling (PD) and fold of periodic orbits (LPC) bifurcations become non-local at the points marked P, and torus bifurcations (labeled NS) where a torus forms around a periodic orbit can become non-local if they are in the vicinity of the green dashed lines.

Global bifurcation structure. System (2.8) is highly degenerate when $B = 0$. It has only one equilibrium point, which is in the fold region unless $A + C = O(\epsilon)$. Asymptotic formulas for the first Lyapunov coefficient of the singular Hopf bifurcation when $B \neq 0$ suggest that the generalized Hopf bifurcation passes through the zero Hopf bifurcation at $B = 0$ in a non-generic manner, see Figures B.1, B.2 as well as B.4, 3.9, B.3 for sequences of (μ, A) diagrams in which B becomes small relative to C. Also, as the generalized Hopf bifurcation passes through the zero Hopf bifurcation, the normal form type of the zero Hopf bifurcation changes [44]. We conjecture that the addition of higher order terms to the system (2.6) can produce qualitative changes in its bifurcation diagram, but do not pursue that issue here.

We next list phenomena that produce changes in the (μ, A) bifurcation diagrams due to non-transverse intersections of these slices with bifurcation manifolds of codimensions one and two:

- folds of generalized Hopf bifurcations,
- folds of the curves where the slow-flow has singular cycles,
- tangential intersections of the period-doubling bifurcation locus and the Hopf bifurcation loci,

- tangential intersection of the torus bifurcation locus and the Hopf bifurcation locus,
- resonant zero Hopf and generalized Hopf bifurcations,
- endpoint of the tangency curve crosses the torus bifurcation locus,
- endpoint of the tangency curve crosses the period-doubling bifurcation locus,
- the tangency curve intersects the period-doubling bifurcation locus tangentially,
- the tangency curve "attaches" to the Hopf curve.

Figure 3.11 displays 16 regions in the (B, C) parameter space of system (2.8). It is largely based on systematic inspection of (μ, A) bifurcation diagrams for $10^{-4} \leq B \leq 10^{-2}$ (see also Appendix C for selected raw data), guided by asymptotic expressions for loci of codimension-three bifurcations. We expect the patterns shown in Figure 3.11 to change significantly for larger values of B. The 16 regions constitute a partitioning into regions corresponding to classes of topologically equivalent (μ, A) bifurcation diagrams, with two caveats: first, regions Ia and Ib as well as VIIIa and VIIIb have topologically equivalent (μ, A) diagrams, we merely distinguish them for symmetry reasons. Changing the sign of parameter C corresponds to reflecting bifurcation curves in (μ, A) diagrams about the μ-axis, and to changing the time orientation. Under this transformation, the tangency curve transforms into a curve corresponding to a tangential intersection of $W^s(E_f)$ with S_a. The tangency involving S_r is present in quadrants I, II and III of Figure 3.11, whereas the tangency involving S_a is present in quadrants II, III and IV of Figure 3.11. Appendix B contains at least one representative (μ, A) bifurcation diagram for each of the 8 regions of (B, C) parameter space in which $C > 0$. Secondly, certain codimension-three events related to the torus bifurcation and its degeneracies are not included in Figure 3.11.

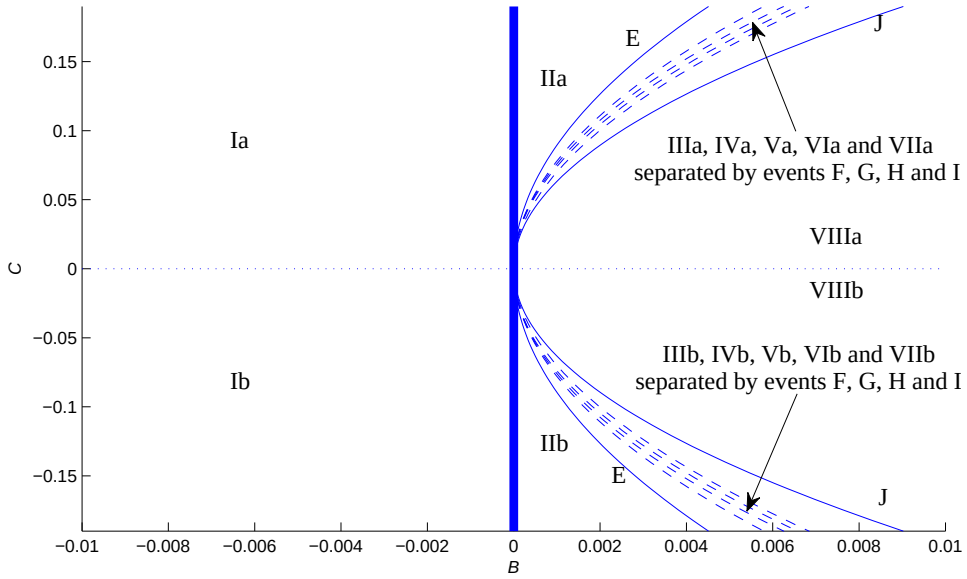

Figure 3.11: Regions in (B, C) parameter space. Solid and dashed lines indicate the positions of codimension-three phenomena that separate regions in (B, C) parameter space yielding different corresponding (μ, A) bifurcation diagrams.

The degeneracy at $B = 0$ (thick solid line in Figure 3.11) separates regions in (B, C) parameter space with vastly different (μ, A) bifurcation diagrams. For C fixed, (μ, A) diagrams become degenerate as $|B|$ tends to 0 and the zero Hopf bifurcation approaches generalized Hopf bifurcations. There is only one topological type of (μ, A) diagram for $B < 0$. The situation is more complicated for $B > 0$. What follows is a description of the topological changes in the (μ, A) diagrams occurring at the curves separating the regions where $B > 0$. We only treat the first quadrant of Figure 3.11, a description for the fourth quadrant may be obtained using the symmetry $C \mapsto -C$. Note that no curves in Figure 3.11 intersect, except maybe for $0 \leq B \ll 10^{-4}$.

Regions IIa and IIIa are separated by curve E, which consists of (B, C) values where

the surface of generalized Hopf (GH) bifurcations is tangent to the (μ, A) slice of the parameter space. The formula for the first Lyapunov coefficient indicates that the curve E is tangent to the parabola $8B = C^2$ at the origin of the (B, C) plane. On this curve, there is a single generalized Hopf (GH) bifurcation of the (μ, A) bifurcation diagrams. To the left of this curve, there are two generalized Hopf bifurcations; to the right there are none. Curves F, G, H and I all correspond to events relating to the tangency curve or to bifurcations of periodic orbits. These curves were found by inspecting appropriate sequences of (μ, A) diagrams. A superset of the data used can be found in appendix C. Regions IIIa and IVa are separated by curve F, where the endpoint of the tangency curve crosses the torus bifurcation locus. In region IIIa, the tangency curve and torus bifurcation curve intersect, while they are disjoint in region IVa. The tangency curve coalesces with the Hopf bifurcation curve at the boundary of regions IVa and Va, represented by curve G. Regions Va and VIa are separated by the curve H, which consists of (B, C) values where the torus bifurcation locus intersects the Hopf bifurcation locus tangentially: to the right of H, the torus bifurcation locus and the Hopf curve no longer intersect. In region VIa, the period-doubling bifurcation locus intersects the Hopf bifurcation in two points. As B is increased, these two points coalesce when the two bifurcation loci intersect tangentially on the curve I, after which they no longer meet in regions VIIa and VIIIa. Regions VIIa and VIIIa are separated by the curve J where the two (μ, A) curves of homoclinic bifurcations coalesce as B increases. The curve J is approximated by the quadratic equation $C^2 - 4B = 0$.

Torus bifurcation and the global bifurcation structure. For $B < 0$, taking account of the torus bifurcation curve and its degeneracies (resonances) does not yield more topologically different (μ, A) bifurcation diagrams. For $B > 0$, the division of (B, C) parameter space into regions with topologically equivalent (μ, A) diagrams gets

significantly more complicated and is not presented here. The paragraphs of Section 3.3 headed "Periodic orbit bifurcations" give a general description of the positions of torus bifurcation curves relative to other bifurcation curves. Data on the position of the crossing of a 1:2 resonance with the Hopf curve can be found in Appendix C.

One-dimensional bifurcation diagrams. Table 3.1 lists the sequences of local bifurcations shown in the (μ, A) diagrams of this chapter and Appendix B that occur as the primary bifurcation parameter μ is increased. We list only sequences occurring well within the (B, C) regions we have identified. There could be some additional sequences, e.g. extremely close to the zero Hopf bifurcation, or where $|B| << C^2$, i.e. where the zero Hopf, generalized Hopf and P bifurcations occur at very similar values of A. Two branches of periodic orbits emanate from LPC bifurcation points. If a sequence begins with an LPC bifurcation and also contains a torus bifurcation or period-doubling, then one branch of periodic orbits emanating from the LPC bifurcation has a torus bifurcation and period-doubling, while the other one ends in a singular Hopf bifurcation. $W^u(E_f)$ and S_r intersect after the tangency in the bifurcation sequences.

3.4 An Example: the Koper model

This section demonstrates how the analysis of our system of first approximation can be used in investigations of systems undergoing singular Hopf bifurcation. We use a vector field that was studied first by Koper [38] as a model of mixed-mode oscillations

Sequence #	Sequence description	(B, C) region present
1	H_{sup}	Ia, IIa, IIIa, IVa, Va, Ib, IIb, IIIb, IVb, Vb
2	H_{sup} - (SN)	IIa, IIIa, IVa, Va, IIb, IIIb, IVb,Vb
3	(SN) - H_{sup} - T ± PD	Ib
4	(SN) - H_{sup} - T ± NS - PD	Ia
5	H_{sup} - LPC	Ia, Ib
6	H_{sup} - T ± PD	Ia, IIa, Ib
7	H_{sup} - T ± NS - PD	IIa
8	LPC - H_{sup} - NS - PD	IIb, IIIb
9	LPC - H_{sup} - PD	IIb, IIIb
10	LPC - H_{sup} - T ± PD	IIa
11	LPC - NS - H_{sup} - PD	IIb, IIIb
12	LPC - PD - H_{sup}	IIb, IIIb, IVb
13	H_{sub}	Ia, IIa, IIIa, IVa, Va, Ib, IIb, IIIb, IVb, Vb
14	H_{sub} - (SN)	IIa, IIIa, IVa, Va, IIb, IIIb, IVb, Vb
15	(SN) - H_{sub} - PD	Ia
16	(SN) - H_{sub} - NS - PD	Ib
17	H_{sub} - LPC	Ia, Ib
18	H_{sub} - PD	Ia, Ib, IIb
19	H_{sub} - NS - PD	IIb
20	LPC - H_{sub} - NS - PD	IIa, IIIa
21	LPC - H_{sub} - T ± NS - PD	IIa, IIIa
22	LPC - H_{sub} - T ± PD	IIa, IIIa
23	LPC - H_{sub} - PD	IIa, IIIa
24	LPC - NS - H_{sub} - T ± PD	IIa, IIIa
25	LPC - PD - H_{sub}	IIa, IIIa, IVa

Table 3.1: List of bifurcation sequences occurring in system (2.8) as the main bifurcation parameter μ is increased. Each sequence is described in terms of the codimension-one bifurcations involved, μ increasing. The sign "-" separates codimension-one bifurcations occurring at different values of μ. A "±" sign appears between two bifurcations where the first bifurcation listed either occurs before the second or indistinguishably close to the second, at the resolution of the diagrams in Chapter 3 and Appendix B. Saddle-node bifurcations are listed in parentheses, since they are only local close to the zero Hopf point.

in chemical systems:

$$\begin{aligned} \epsilon_1 \dot{x} &= k\, y - x^3 + 3\, x - \lambda \\ \dot{y} &= x - 2\, y + z \\ \dot{z} &= \epsilon_2\, (y - z) \end{aligned} \tag{3.3}$$

Further discussion of this model can be found in [41], [43] as well as Desroches et al. [9] and references cited there. Using affine coordinate changes and a time rescaling

(see [9]), the Koper vector field can be written in the following form:

$$\begin{aligned} \dot{x} &= (y - x^2 - x^3)/\epsilon \\ \dot{y} &= z - x \\ \dot{z} &= -\mu - a\,x - b\,y - c\,z \end{aligned} \tag{3.4}$$

Note that

- the system (3.4) has one more parameter than the system (3.3), so the Koper vector field is a subfamily of (3.4), and
- the system (3.4) is a variant of the singular Hopf normal form (2.6) in which the parabolic critical manifold has been replaced by a cubic critical manifold [9] by the addition of a single, higher order term to the equation.

With the scaling of parameters and coordinates used to obtain system (2.8) from system (2.6), (3.4) transforms to

$$\begin{aligned} \dot{X} &= (Y - X^2 - \epsilon^{1/2}X^3) \\ \dot{Y} &= Z - X \\ \dot{Z} &= -\mu - AX - BY - CZ. \end{aligned} \tag{3.5}$$

It is apparent that the system (3.5) is a small perturbation of the system (2.8) in a bounded region of (X, Y, Z) space. Figures 3.12 and B.1 show (μ, A) bifurcation diagrams for systems (3.5) and (2.8) at the same values of $(B, C) = (-0.01, 0.1)$. The similarity of these two figures supports the use of the normal form (2.6) to study local bifurcations near a singular Hopf bifurcation. Note that the cusp of the saddle-node curve in Figure 3.12 is not local: it tends to infinity as $\epsilon \to 0$.

Consider the Koper model with $\epsilon_2 = 1$. When additionally $\epsilon_1 = 0.1$ and $k = -10$, there is a supercritical singular Hopf bifurcation at approximately $\lambda \approx -7.670$. Continuing this family of periodic orbits with varying λ using AUTO, we find that the emerging

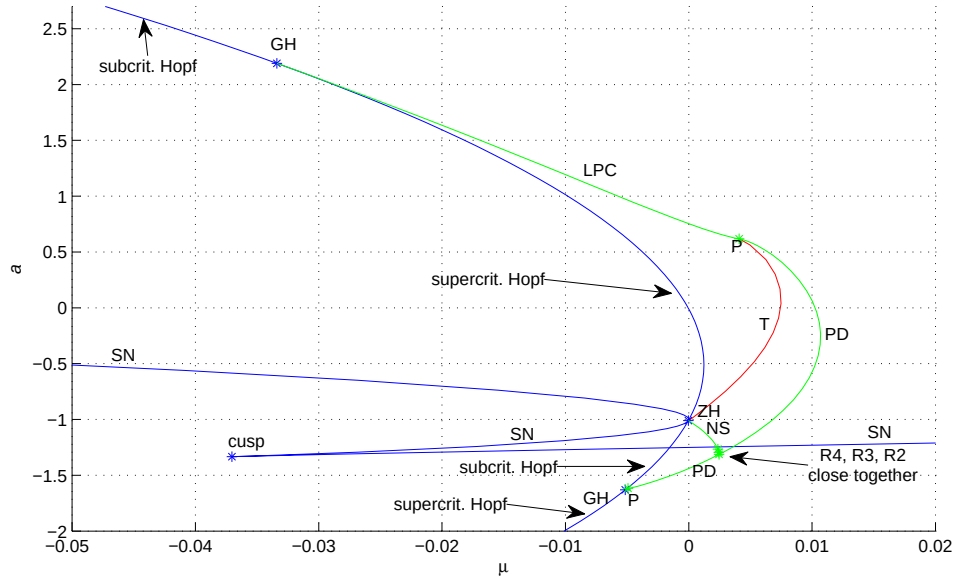

Figure 3.12: Bifurcation diagram for cubic singular Hopf normal form, $b = -1, c = 1$ (i.e., $B = -0.01, C = 0.1$).

periodic orbit undergoes a period-doubling bifurcation at $\lambda \approx -7.461$, and the "undoubled" periodic orbit undergoes a fold of periodic orbits (LPC) bifurcation at $\lambda \approx -6.235$. The periods of the periodic orbits at the bifurcation points are approximately 0.64, 0.82 and 1.67 respectively. If τ denotes the initial period of the periodic orbits emerging from the singular Hopf bifurcation, local bifurcations of periodic orbits typically occur with periods less than 1.5τ. This suggests that the LPC bifurcation is not local. Figure 3.13 shows that indeed, the shape of the periodic orbit at the LPC bifurcation follows the cubic shape of the critical manifold, rather than staying close to the fold curve at which the singular Hopf bifurcation occurred.

Among the sequences with a supercritical Hopf bifurcation, only 3, 4 and 6 to 12 also have a period-doubling. Note that sequences 8 to 12 have a period-doubling bifurcation

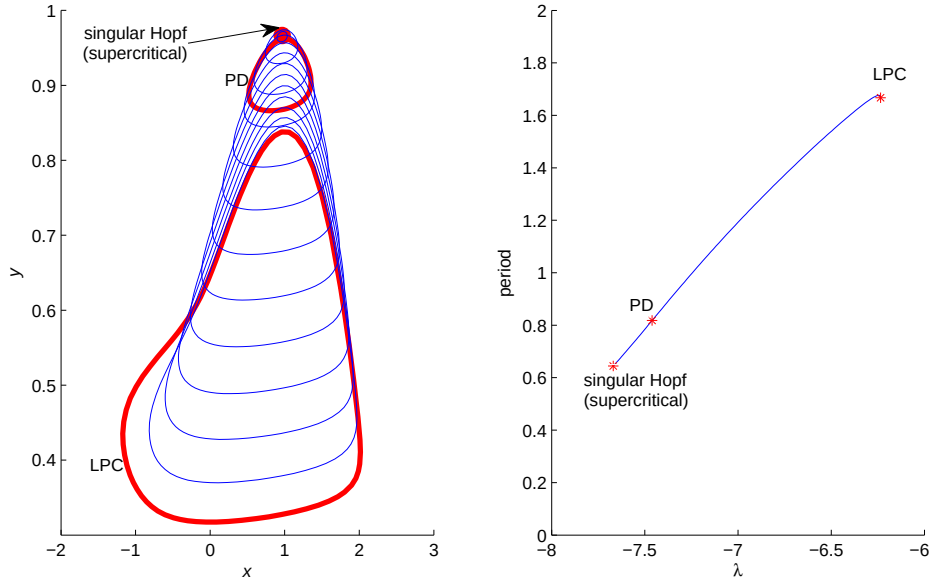

Figure 3.13: Periodic orbits emanating from a supercritical Hopf bifurcation for system (3.3) and $\epsilon_1 = 0.1, \epsilon_2 = 1, k = -10$. Observe that the periodic orbits follow the cubic shape of the (parameter-dependent) critical manifold more as λ increases.

and a supercritical Hopf bifurcation on distinct branches of periodic orbits, and that sequences 4 and 7 contain torus bifurcations. Thus, only sequences 3 and 6 match the continuation data. This suggests that there is a tangency of invariant manifolds either between the supercritical Hopf bifurcation and the period-doubling bifurcation or very close to the period-doubling bifurcation: indeed, numerical calculations show that the tangency occurs at $\lambda \approx -7.539$.

Due to the S-shape of the critical manifold in the Koper model, trajectories in the unstable manifold in the vicinity of the fold region that escape from the fold region can return to the fold region. As a result, the tangency of invariant manifolds can mark the onset of mixed-mode oscillations: a trajectory approaches the equilibrium point near the

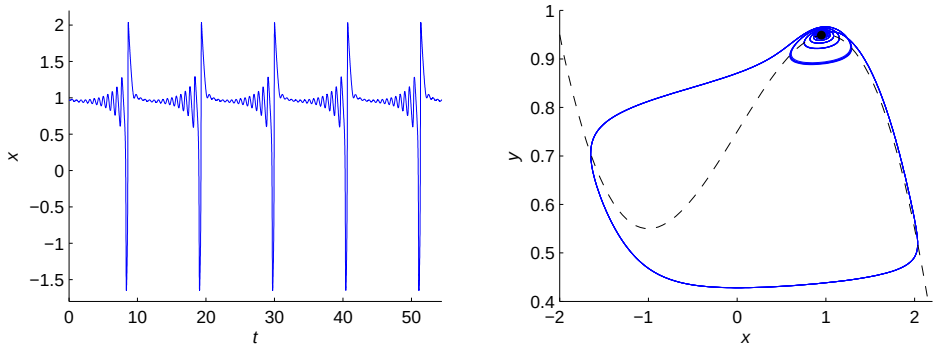

Figure 3.14: Mixed-mode oscillations in system (3.3) with $\epsilon_1 = 0.1, \epsilon_2 = 1, k = -10, \lambda = -7.50$: the left panel shows the time-series of the x-coordinate of an MMO trajectory, the right panel shows the same trajectory in the xy-plane. E_f is marked with a black dot, the critical manifold is drawn as a dashed black line.

fold region, then follows the equilibrium's two-dimensional unstable manifold, leaves the fold region, and approaches the equilibrium once more along its stable manifold. The Koper system has mixed-mode oscillations at $\lambda = -7.50$, illustrated in Figure 3.14. Thus local analysis of system (2.8) led to information about the Koper model as an alternative to applying numerical continuation tools directly on the Koper model. This approach can be used to explore the effects of varying additional parameters in the Koper model as well as to study other systems in which singular Hopf bifurcation occurs.

3.5 Discussion

This chapter includes a comprehensive analysis of bifurcations that occur in the normal form (2.6) for a singular Hopf bifurcation. In particular, we analyze bifurcations of

equilibrium points, periodic orbits originating from these equilibria and "simple" tangencies between the unstable manifold $W^u(E_f)$ of an equilibrium E_f and a repelling slow manifold S_r of the system. We approach the study of these bifurcations in a hierarchical fashion, designating the parameter μ as the primary bifurcation parameter and then performing analyses of parallel two-dimensional slices throughout the four-dimensional parameter space of the system. While our analysis is comprehensive, it is hardly complete. We point to three aspects of the bifurcations of this system for further study.

In some parameter ranges, the system (2.6) has complicated invariant sets in $O(\sqrt{\epsilon})$ neighborhoods of the origin. Torus and period-doubling bifurcations of periodic orbits give rise to invariant sets that undergo further bifurcations. We have not pursued the study of these invariant sets or their bifurcations. Trajectories in these sets typically make multiple oscillations when projected to the (x, y) coordinate plane. Similarly, there are more complex intersections of invariant manifolds than those we have investigated in this chapter. The three two-dimensional invariant manifolds that we have studied are the attracting and repelling slow manifolds and the unstable manifold of an equilibrium point. In some parameter regimes, the attracting and repelling slow manifolds have multiple intersections that constitute maximal canards of a folded node of the system [3, 20, 66]. These manifolds and their intersections bound rotational sectors of trajectories that make different numbers of oscillations as they pass through the folded node region. The unstable manifold of the equilibrium can also become entangled with the repelling slow manifold and have multiple intersections that separate regions of the unstable manifold that flow to $x = -\infty$ after making different numbers of oscillations. In systems like the Koper model where trajectories jumping from the vicinity of a singular Hopf bifurcation make a global return to that region, tangencies between the different invariant manifolds play a significant role in the bifurcations of MMOs. We have not

considered here secondary tangencies of the unstable manifold and the repelling slow manifold that are analogous to the bifurcations of secondary canards of a folded node analyzed by Wechselberger [66].

The second aspect of singular Hopf bifurcation that calls for further investigation is the presence of highly degenerate bifurcations within the normal form. In particular, we have seen that the system is very degenerate when $b = 0$. In analogy with the study of codimension-two bifurcations of equilibria [21], the addition of higher order terms could resolve this degeneracy. We do not study that possibility here. Additionally, as noted by a referee of [24], the normal form (2.6) has a continuous family of periodic orbits when the parameters (μ, a, b, c) are all zero. Higher order terms in the Taylor expansion of the normal form can destroy this degeneracy.

Third, our investigation of the points P where period-doubling bifurcation, fold of periodic orbits bifurcation and the slow flow has singular cycles meet at the degenerate homoclinic bifurcation remains incomplete. These points appear to be homoclinic orbit flips or inclination flips [40], but we have not reconciled aspects of the behavior found here with that predicted by the unfoldings of generic orbit flips or inclination flips. Investigations of phase portraits suggest that if $B < 0$, there is a homoclinic orbit flip at approximately $(\mu, A) = (B/4, (-C \pm \sqrt{C^2 - 4B})/2)$, provided that the square root evaluates to a real number. However, we find that the relative positions of the bifurcation curves are interchanged from those predicted by the theory, cf. [54] and Figure 3.15. If $B > 0$, we surmise the existence of an homoclinic orbit [inclination] flip of type C [54] at approximately $(\mu, A) = (B/4, (-C - \sqrt{C^2 - 4B})/2)$ if the parameter C is positive [negative], and at $(\mu, A) = (B/4, (-C + \sqrt{C^2 - 4B})/2)$ if parameter C is negative [positive], cf. Section 3.2.

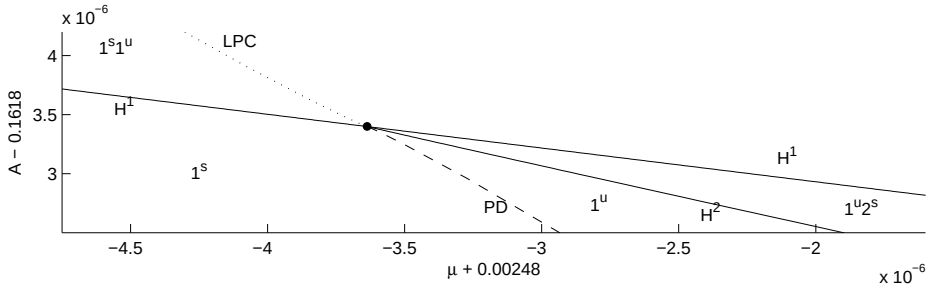

Figure 3.15: Bifurcation diagram for system (2.8), showing bifurcation curves of periodic orbits in the vicinity of homoclinic orbit flip at $(\mu, A, B, C) = (-0.00248364, 0.161803, -0.01, -0.1)$. Numbers with superscripts s or u indicate the number of loops as well as the stability of periodic orbits in each region of parameter space. Unstable periodic orbits are of saddle-type. The labels H^1 and H^2 distinguish homoclinic bifurcation loci of periodic orbits with one and two loops respectively.

CHAPTER 4

CASE STUDY: SINGULAR HOPF BIFURCATION IN A PITUITARY LACTOTROPH MODEL

Section 3.4 applied insights from the singular Hopf normal form analysis in Chapter 3 to a model for a chemical reactor introduced by Koper. Recall that Koper's vector field is up to a perturbative term of higher order in ϵ a subfamily of that of the singular Hopf normal form. This chapter demonstrates studies a model for electrical activity in a pituitary lactotroph cell, focussing on singular Hopf bifurcation and mixed-mode oscillations.

4.1 Model definition

Toporikova et al. [62] introduced a three-variable model for electrical activity in a lactotroph cell in 2008. The model is based on an earlier model for electrical activity and calcium dynamics in lactotroph cells by Tabak et al. [60], and has more recently been studied by Vo et al. [64, 65]. In the model, V is the membrane potential of the cell, n is the fraction of activated K^+ channels of the delayed rectifier type, and e is the fraction of A-type K^+ channels that are not inactivated.

$$\begin{aligned} C\frac{dV}{dt} &= -(I_{Ca} + I_K + I_A + I_L) \\ \tau_e \frac{de}{dt} &= e_\infty(V) - e \\ \tau_n \frac{dn}{dt} &= n_\infty(V) - n \end{aligned} \tag{4.1}$$

The ionic currents I_{Ca}, I_K, I_A and I_L are given by

$$\begin{aligned} I_{Ca} &= g_{Ca}\, m_\infty(V)\,(V - V_{Ca}) \\ I_K &= g_K\, n\,(V - V_K) \\ I_A &= g_A\, a_\infty(V)\, e\,(V - V_K) \\ I_L &= g_L\,(V - V_K), \end{aligned} \tag{4.2}$$

where

$$x_\infty(V) = \frac{1}{1 + \exp(\frac{V_x - V}{s_x})} \tag{4.3}$$

for $x = m, n, a$ and

$$e_\infty(V) = \frac{1}{1 + \exp(\frac{V - V_e}{s_e})}. \tag{4.4}$$

Following Vo et al., we will vary C, g_K and g_A and keep all other parameters fixed. The parameter values used are given in Table 4.1.

Parameter	Value	Definition
C	0 – 20 pF	Membrane capacitance
g_K	0 – 10 nS	Maximal conductance of delayed rectifier K^+ channels
g_A	0 – 25 nS	Maximal conductance of A-type K^+ channels
g_{Ca}	2 nS	Maximal conductance of Ca^{2+} channels
V_{Ca}	50 mV	Reversal potential for Ca^{2+}
V_m	−20 mV	Voltage value at midpoint of m_∞
s_m	12 mV	Slope parameter of m_∞
V_K	−75 mV	Reversal potential for K^+
V_n	−5 mV	Voltage value at midpoint of n_∞
s_n	10 mV	Slope parameter of n_∞
τ_n	40 ms	Time constant for n
V_a	−20 mV	Voltage value at midpoint of a_∞
s_a	10 mV	Slope parameter of a_∞
V_e	−60 mV	Voltage value at midpoint of e_∞
s_e	5 mV	Slope parameter of a_∞
g_L	0.3 nS	Maximal conductance of leak current
τ_e	20 ms	Time constant of e

Table 4.1: Table showing parameter values used for model (4.1).

Vo et al. [64] show that system (4.1) can be regarded as a slow-fast system with one fast and two slow variables by non-dimensionalizing V as well as selected system

parameters. Specifically, they introduce $k_v = 100$ mV as a typical voltage scale and $k_t = \tau_e = 20$ ms as a typical slow time scale of the system. Time is scaled to $\tau = t/k_t$. The voltage V is scaled to $v = V/k_v$, and the parameters of the steady state activation and inactivation functions are scaled to match the scaling of V. The parameters g_x are scaled to $\tilde{g}_x = g_x/g_{max}$ for $x \in \{Ca, K, A, L\}$ and $g_{max} = \max(g_{Ca}, g_K, g_A, g_L)$. The result is a dimensionless slow-fast system with slow variables e and n, fast variable v, separation of time scales parameter $\epsilon = \tau_v/k_t = C/(k_t\, g_{max})$.

We sometimes found it inconvenient that due to the maximum that appears in the above scalings, the scaled system parameters depend non-smoothly on the original parameters. We therefore worked with $g_{max} = 5$ rather than $g_{max} = \max(g_{Ca}, g_K, g_A, g_L)$.

Overview. The contents of this chapter is organized as follows: Section 4.2 describes the algebraic manipulations that bring system (4.1) into singular Hopf normal form (2.6).

Section 4.3 presents bifurcation diagrams for (4.1) and compares the system's bifurcation structure with that of the singular Hopf normal form.

Section 4.4 uses the analysis of the singular Hopf normal form in [24] to predict the onset of mixed-mode oscillations in (4.1) to be at a subcritical singular Hopf bifurcation. We track the MMOs as the parameter g_K of system (4.1) increases, and observe how the mixed-mode behavior gradually morphs into relaxation oscillations.

4.2 Transformation of the lactotroph model (4.1) to singular Hopf normal form

4.2.1 Computation of singular Hopf normal form coefficients

We describe the algebraic manipulations that bring system (4.1) into singular Hopf normal form (2.6). This is done by means of coordinates changes that eliminate certain constant, linear and quadratic-order terms from the Taylor series expansions of the derivatives of system (4.1). At the end, the system obtained will match the singular Hopf normal form up to and including quadratic terms in the fast equation, and up to and including linear terms in the slow equation. The singular Hopf normal form coefficients μ, a, b and c can now be read off as the constant and linear coefficients in the transformed system.

Since the changes of coordinate result in systems whose Taylor series coefficients are complicated expressions of the original coefficients, the computations were carried out using the computer algebra system Mathematica [72].

We begin by passing to the non-dimensionalized form of (4.1), in which v is a fast variable and e and n are slow variables. Solving a system of linear equations, we compute the parameter $\tilde{g}_{L_0}$ as well as the (e, n) coordinates (e_0, n_0) at which a folded singularity occurs, as a function of the v coordinate v_0 of the folded singularity and all Toporikova system parameters except $\tilde{g}_L$. A translation $(\bar{v}, \bar{e}, \bar{n}) = (v - v_0, e - e_0, n - n_0)$ moves the folded singularity to the origin. We then relabel $\bar{v}, \bar{e}$ and $\bar{n}$ as v, e and n. We moreover replace $\tilde{g}_L$ by $\tilde{g}_{L_0}$ in the system, before expanding the system as a multivariable Taylor series in v, e and n around the origin up to quadratic terms.

Some of the Taylor series coefficients are sizable expressions, while several others are identical to 0: since the folded singularity is on the critical manifold, the constant coefficient in the expansion of $\frac{dv}{d\tau}$ equals 0. In a similar way, the linear coefficient in v in the expansion of $\frac{dv}{d\tau}$ equals 0. Inspection of the form of $\frac{de}{d\tau}$ and $\frac{dn}{d\tau}$ shows that only four out of the 10 Taylor series coefficients in each of the corresponding Taylor series are non-zero. To keep the size of the expressions that appear in the derivation of the normal form coefficients manageable, we therefore temporarily work with the system shown below:

$$\begin{aligned}
\frac{dv}{d\tau} &= \left(c_1^1 e + c_2^1 n + c_3^1 v^2 + c_4^1 e^2 + c_5^1 n^2 + c_6^1 ve + c_7^1 vn + c_8^1 en\right)/\epsilon \\
\frac{de}{d\tau} &= c_1^2 + c_2^2 v + c_3^2 e + c_4^2 v^2 \\
\frac{dn}{d\tau} &= c_1^3 + c_2^3 v + c_3^3 n + c_4^3 v^2
\end{aligned} \tag{4.5}$$

The expressions for the coefficient functions are only substituted in the final step of the derivation. Note however that the transformations below do not rely on any of the coefficients in the slow derivatives being zero. The zero coefficients merely make the computation more amenable to being carried out on a resource-constrained computer.

The next steps will be algebraic manipulations that bring the fast derivative of the system into the required form. Let $a = \frac{c_6^1}{2c_3^1}$ and $b = \frac{4c_3^1 c_5^1 - (c_7^1)^2}{4c_1^1 c_3^1}$. In a nonlinear change of coordinates $\bar{v} = v + ae + bn$, we eliminate the vn and ve terms from the fast equation. It is interesting to observe that this transformation mixes slow as well as cubic terms into the fast equation. We relabel $\bar{v}$ as v. Now let $c = \frac{4c_3^1 c_5^1 - (c_7^1)^2}{4c_1^1 c_3^1}$ be the n^2 coefficient of the fast part of $\frac{dv}{d\tau}$ derivative divided by the e coefficient of the fast part of the $\frac{dv}{d\tau}$ derivative. We make a change of coordinates $\bar{e} = e + cn^2$ to eliminate n^2 from the fast part of the $\frac{dv}{d\tau}$ equation. We relabel $\bar{e}$ as e. Letting $d = -\frac{-64(c_1^1)^2(c_3^1)^3 c_4^1 + 16(c_1^1)^2(c_3^1)^2(c_6^1)^2}{64(c_1^1)^2 c_2^1 (c_3^1)^3}$ be the coefficient of the e^2 term in the fast part of $\frac{dv}{d\tau}$ divided by the coefficient of the n term in the fast part of $\frac{dv}{d\tau}$, we make a substitution $\bar{n} = n + de^2$ and thus eliminate the fast e^2 terms from $\frac{dv}{d\tau}$. After dropping the bar from $\bar{n}$, we let $g = -\frac{c_6^1 c_7^1 - 2c_3^1 c_8^1)}{2c_1^1 c_3^1}$ be the fast en term of $\frac{dv}{d\tau}$ divided by

the fast e term of $\frac{dv}{d\tau}$, and make a change of coordinates $\bar{e} = e + gen$. We relabel $\bar{e}$ as e and now have a system in which the only quadratic fast term of $\frac{dv}{d\tau}$ is v^2 times a constant. Making a linear transformation $\bar{e} = e + hn$, where $h = \frac{c_2^1}{c_1^1}$ is the coefficient of the n term in the fast part of $\frac{dv}{d\tau}$ divided by the coefficient of the e term in the fast part of $\frac{dv}{d\tau}$, we eliminate the fast n term from $\frac{dv}{d\tau}$. We again drop the bar.

Due to the nonlinear changes of coordinate, the expressions for the derivatives now include cubic and higher-order terms. Such terms do not enter the normal form coefficients. To speed up the computer algebra, we therefore truncate these terms at this point. In the slow equations, quadratic terms can be discarded for the same reason. We revisit in Section 4.3 to which extent the truncations matter for the dynamics and bifurcation behavior of the system. We now scale v via $v \mapsto v/l$, where $l = c_3^1$ is the coefficient of v^2 in the fast part of the $\frac{dv}{d\tau}$ equation. We now have

$$\frac{dv}{d\tau} = \left(v^2 + \frac{c_1^1}{c_3^1}e\right)/\epsilon + [\text{slow terms}].$$

The slow terms in the fast equation can be eliminated by a substitution $\bar{e} = -(\frac{c_1^1}{c_3^1}e + \epsilon \cdot [\text{slow terms}])$. Note that the slow terms may and do involve e. To obtain derivatives only involving $\bar{e}$, we compute using series inversion the e that satisfies $\bar{e} = -(\frac{c_1^1}{c_3^1}e + \epsilon \cdot [\text{slow terms}])$ to first order in $\bar{e}$. Higher-order terms do not enter the singular Hopf normal form and thus do not need to be included. After the substitution has been completed, we relabel $\bar{e}$ as e.

We now reverse time, so that the v and e derivatives have the form

$$\begin{aligned} \frac{dv}{d\tau} &= (e - v^2)/\epsilon \\ \frac{de}{d\tau} &= \alpha + \beta v + \gamma e + \delta n. \end{aligned} \tag{4.6}$$

Following Guckenheimer [19], we change coordinates $\bar{n} = (n + \alpha + \gamma e)/\delta$, drop the bar, and subsequently scale $(\bar{v}, \bar{e}, \bar{n}, \bar{\tau}) = (v|\beta|^{1/2}, e|\beta|, n|\beta|^{3/2}, \tau|\beta|^{-1/2})$ to obtain, after

dropping bars, a system of the following form:

$$\begin{aligned} \frac{dv}{d\tau} &= (e - v^2)/\epsilon \\ \frac{de}{d\tau} &= n - v \\ \frac{dn}{d\tau} &= -\mu - av - be - cn. \end{aligned} \tag{4.7}$$

The system is now in singular Hopf normal form, and the coefficients μ, a, b, c are the singular Hopf normal form coefficients. They are functions of the c_i^j, and thus of the original system parameters of system (4.1) except g_L, as well as v_0. The value of v_0 may be fixed to become a new system parameter, while g_L is replaced by a relatively simple algebraic expression in v_0 and the other parameters of system (4.1). In this formulation, g_A in system (4.1) will, although it no longer appears explicitly as a parameter, effectively vary as C, g_K and g_A vary. Alternatively, the value of v_0 can be computed numerically in terms of a fixed g_L and the other parameters of system (4.1), for instance using Newton's method. Since Vo et al. fix $g_L = 0.3$ nS [64], we chose the latter approach and computed a 14-th order polynomial in variables g_K and g_A that approximates v_0 uniformly on $3.5 \leq g_K \leq 4, -50 \leq g_A \leq 500$ with a relative error of less than 10^{-11}, for capacitance $C = 0.5$ fixed.

Numerical studies suggest that for the parameter ranges of system (4.1) we work with in the remainder of this chapter, β is always negative, thus the coefficients in the obtained system remain smooth functions of the parameters of system (4.1).

4.2.2 Evaluation of singular Hopf normal form coefficients

The expressions obtained for the singular Hopf coefficients are large - on the order of 100,000 lines of Fortran code. The size of the expressions is largely due to our decision

to compute v_0 as a function of the parameters of system (4.1). A single evaluation of the expressions at given parameters (g_K, g_A) takes on the order of one second to execute in Mathematica. For the computations in Section 4.3, we therefore approximate the singular Hopf coefficient expressions using 13-th order polynomials in g_K and g_A that uniformly have a relative error of less than 2×10^{-8} on $3.5 \leq g_K \leq 4, -50 \leq g_A \leq 500$ for the capacitance fixed at $C = 0.5$. This range of parameters corresponds to those that we considered most interesting with respect to the analysis of singular Hopf normal form behavior, and to those parameters for which bifurcation behavior will be studied in subsequent sections. Note that the range of g_K included here is much narrower than in Toporikova et al. [62] and Vo et al. [64], while the range of g_A is much wider.

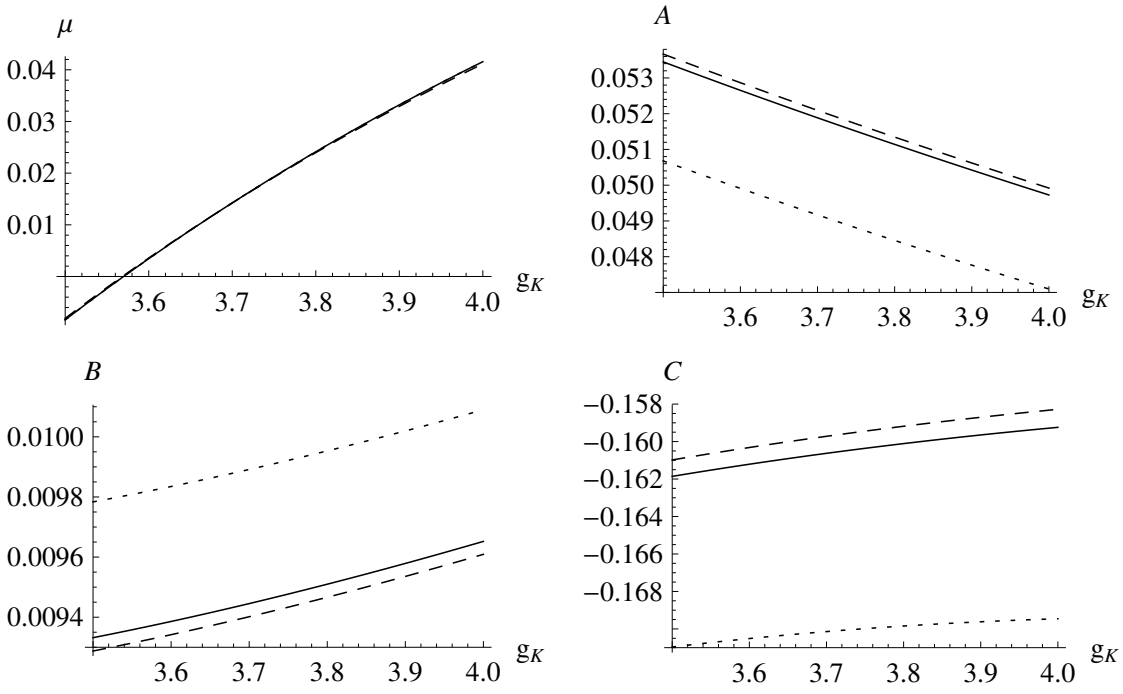

Figure 4.1: Scaled singular Hopf normal form coefficients μ, A, B and C for system (4.1), with capacitance $C = 0.5$. The dashed lines correspond to $g_A = 0.25$, the solid lines to $g_A = 25$, and the dotted lines to $g_A = 250$. The separation of time scales parameter ϵ is 0.005.

Figure 4.1 shows plots of the four scaled singular Hopf coefficients as functions of g_K and g_A. Observe that the ranges of coefficients μ, A, B, C that are shown include values where μ, A, B and C are of sizes $O(\epsilon)$, $O(\epsilon^{1/2})$, $O(\epsilon)$ and $O(\epsilon^{1/2})$ respectively. This corresponds to μ, a, b and c in (2.6) being $O(1)$. Larger coefficients would indicate that the separation of time scales parameter is not small enough to clearly separate the slow and fast time scales.

The derivation of the singular Hopf normal form coefficients, including the expressions obtained for the coefficients, can be found as a Mathematica script in the supplementary program files [79].

4.3 Comparison of normal form and lactotroph model bifurcation behavior

4.3.1 Similarities in bifurcation behavior

With the singular Hopf coefficient functions computed in the previous section, we expect the normal form (2.8) to approximate the lactotroph model (4.1) near the origin. Note that even near the origin, phase portraits of the two systems differ by a change of coordinates. This section discusses to which extent the approximation produces valid results when $C = 0.5$, corresponding to $\epsilon = 0.005$. We present bifurcation diagrams for system (4.1) and compare the system's bifurcation structure to that of the singular Hopf normal form.

The lactotroph model (4.1) undergoes a singular Hopf bifurcation at $(C, g_K, g_A) = (0.5, 3.59376, 4)$ and $(V, e, n) = (-14.4484, 1.10507 \times 10^{-4}, 0.279924)$, which corre-

sponds to scaled singular Hopf coefficients $(\mu, A, B, C) = (0.00286, 0.05288, 0.00934, -0.16049)$ and $\epsilon = 0.005$. The singular Hopf normal form undergoes singular Hopf bifurcation at $\mu + A^2/2 + AC/2 + O(\epsilon^{3/2}) = 0$ [19]. Indeed, we find that for the above normal form coefficients $\mu + A^2/2 + AC/2 = 1.12 \times 10^{-5} << \epsilon^{3/2}$. This suggests that the normal form approximates the bifurcation behavior of system (4.1) well in parameter regions where the scaled normal form coefficients μ, A, B and C are $O(\epsilon), O(\epsilon^{1/2}), O(\epsilon)$ and $O(\epsilon^{1/2})$ respectively. Possibly also show or comment on data for other values of g_A, to show that the Hopf bifurcation is in the expected place for a wide range of g_A.

Figures 4.2 and 4.3 show bifurcation diagrams for system (4.1), computed with the continuation software AUTO [74]. We show three bifurcation curves: a saddle-focus equilibrium point turns into a sink as g_K decreases across a Hopf bifurcation curve. The criticality of the Hopf bifurcation changes at a generalized Hopf bifurcation, where the Hopf bifurcation curve meets a fold of periodic orbits (LPC) bifurcation curve. Periodic orbits can moreover undergo period-doubling (PD) bifurcations. The period-doubling bifurcation curve gets extremely close to the fold of periodic orbits before the two curves veer away from each other. The approach of the two curves is nearly tangential. For $C = 5$, the two curves can be resolved by AUTO. Where the two curves get very close, this is no longer possible at $C = 0.5$. However, a numerical investigation suggests that the product of the absolute values of the two non-trivial multipliers of the bifurcating periodic orbit is very large where the period-doubling and fold bifurcation are close to each other. Since period-doubling and fold bifurcations occur where non-trivial multipliers of -1 and 1 occur respectively, the two bifurcations cannot occur simultaneously while the product of the absolute values of the two non-trivial multipliers is large. Tracking the periodic orbits on the PD and LPC curve as g_A decreases toward the region where the curves come close, we found that the periodic orbits grow rapidly in size in a canard explosion. Figure 4.2 includes a tangency of invariant manifolds bifurcation curve,

which was computed using the same methods as in Appendix D, with an accuracy in g_K of at least 2×10^{-4}.

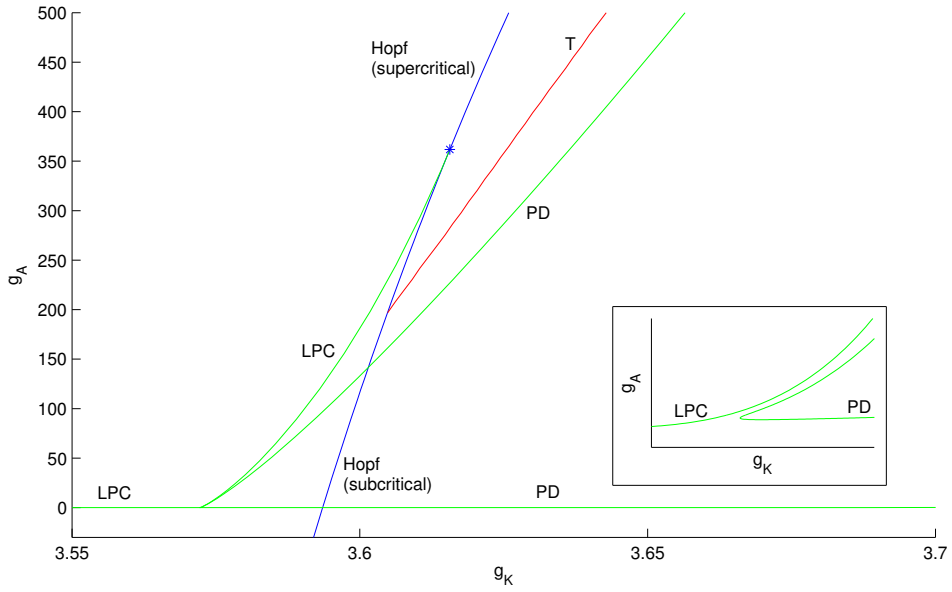

Figure 4.2: Bifurcation diagram for system (4.1) with capacitance $C = 0.5$. A Hopf bifurcation curve and fold of periodic orbits (LPC) bifurcation curve meet at a generalized Hopf bifurcation. The LPC bifurcation curve and a period-doubling bifurcation curve (PD) get very close before veering away from each other, as illustrated in an exaggerated fashion in the inset. A curve of tangency bifurcations (T) begins extremely close to the Hopf bifurcation curve.

The arrangement of Hopf, fold of periodic orbits, period-doubling bifurcation and tangency curve described above for system (4.1) with capacitance $C = 0.5$ appears in the singular Hopf normal form in a very similar form. Figure 4.4 shows a two-dimensional bifurcation diagram for system (2.6) in which the singular Hopf coefficients B and C have been fixed at 0.001 and 0.1 respectively (see [24] for a detailed bifurcation analysis of the normal form). As in the bifurcation diagrams for system (4.1), we find that a Hopf

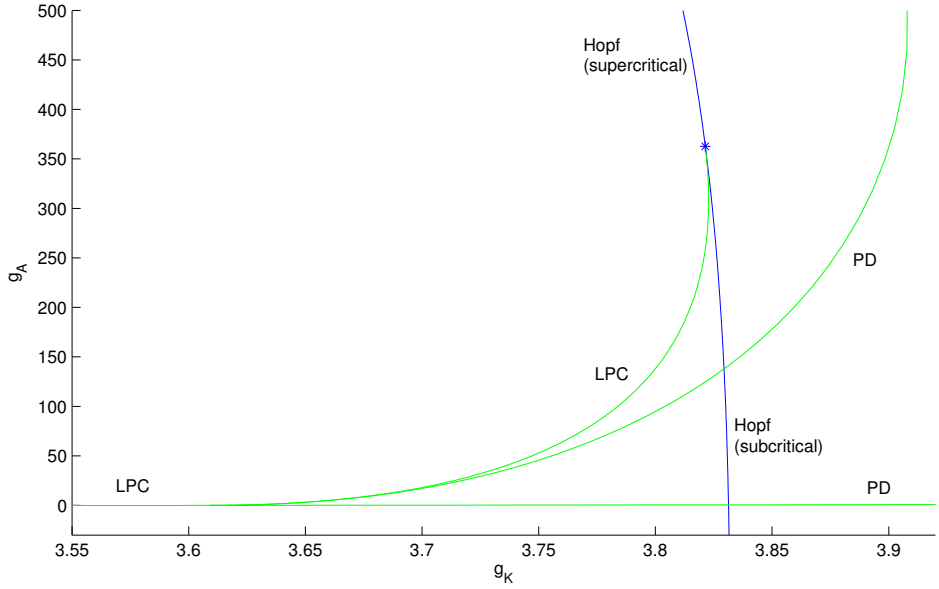

Figure 4.3: Bifurcation diagram for system (4.1) with capacitance $C = 5$. A fold of periodic orbits (LPC) bifurcation curve and a period-doubling bifurcation curve (PD) get very close to each other but do not meet and eventually veer away from each other. As for $C = 0.5$, the LPC curve meets a Hopf bifurcation curve (blue) at a generalized Hopf bifurcation.

bifurcation curve and an LPC curve meet at a generalized Hopf bifurcation, and that a PD and LPC curve approach each other in a region where periodic orbits grow to large sizes.

4.3.2 Differences in bifurcation behavior

Evaluating the normal form coefficients at the parameters $C = 0.5, 3.5 \leq g_K \leq 4, -50 \leq g_A \leq 500$, we find that $-0.014 < C^2 - 4B < -0.007 < 0$. According to the normal form bifurcation analysis in [24], no fold of periodic orbits or period-doubling bifurcations

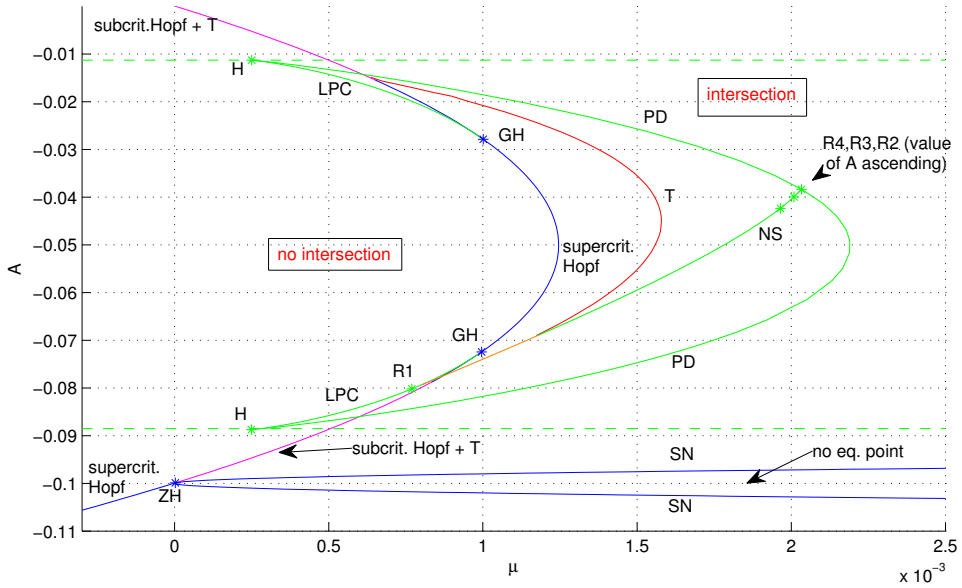

Figure 4.4: Bifurcation diagram for system (2.8) with singular Hopf normal form coefficients B and C fixed at $B = 0.001, C = 0.1$. Note that there are two regions in the diagram where a period-doubling (PD) and fold of periodic orbits (LPC) curve meet at points labeled H, with the LPC curve also meeting the Hopf bifurcation curve tangentially at a generalized Hopf (GH) bifurcation. A curve of tangency bifurcations (red, labeled T) begins very close to the Hopf bifurcation curve.

of the singular Hopf periodic orbit have been found in the normal form in parameter regions where $C^2 - 4B < 0$. This does not match the data from Figures 4.2 and 4.3. The discrepancies are likely due to the effect of quadratic and higher-order terms in the slow equations that were truncated in the derivation of the normal form coefficients. At $(C, g_K, g_A) = (0.5, 3.55644, 4)$, the point $(v, e, n) = (-0.06974, -0.02807, -0.02057)$ lies on a periodic orbit of the un-truncated system. At this parameter, the vector field of the transformed system (4.1) is approximately given by the expressions below, in which

terms containing cubic and higher powers of v, e and n have been truncated:

$$\begin{aligned}\frac{dv}{d\tau} = {} & 0.000262981 - 62.7745e - 0.00661863e^2 + 0.920704n - 0.955153en \\ & - 458.776e^2n + 1.13126n^2 + 839.679en^2 - 2584.38e^2n^2 + 0.280422v \\ & - 0.799607ev - 0.420264e^2v + 0.76533nv - 1.84635e^2nv + 0.560389n^2v \\ & + 5.14446en^2v - 7.0236e^2n^2v - 255.149v^2 + \text{higher-order terms},\end{aligned}$$

$$\begin{aligned}\frac{de}{d\tau} = {} & -2.80808 \times 10^{-17} - 1.90041e + 4.24907e^2 + 1.55838n - 10.5079en \\ & + 16.6104e^2n + 6.52303n^2 - 31.3915en^2 - 15.3118e^2n^2 + 1.40955v \\ & - 5.42213ev + 1.34955e^2v + 5.1897nv - 5.85557env - 33.2304e^2nv \\ & + 6.02678n^2v + 57.0567en^2v - 271.858e^2n^2v + 3.09294v^2 - 3.30096ev^2 \\ & - 1.62081e^2v^2 + 3.15945nv^2 + 4.41002env^2 - 31.0525e^2nv^2 - 0.936582n^2v^2 \\ & + 60.2599en^2v^2 - 185.172e^2n^2v^2 + \text{higher-order terms},\end{aligned}$$

and

$$\begin{aligned}\frac{dn}{d\tau} = {} & -0.000430785 - 0.647757e + 2.36203e^2 + 0.120621n - 6.74992en \\ & + 1.97713e^2n + 4.78342n^2 - 9.5842en^2 - 34.8874e^2n^2 + 1.01333v \\ & - 2.8071ev - 1.41183e^2v + 2.6845nv + 1.41173env - 18.6334e^2nv \\ & - 0.124438n^2v + 41.2268en^2v - 114.372e^2n^2v + 2.20465v^2 - 0.0519603ev^2 \\ & + 0.072388nv^2 + 3.31771env^2 - 17.0983e^2nv^2 - 4.62203n^2v^2 + 28.7904en^2v^2 \\ & - 75.1184e^2n^2v^2 + \text{higher-order terms}.\end{aligned}$$

At the point $(v, e, n) = (-0.06974, -0.02807, -0.02057)$ on the periodic orbit of the un-truncated system, the expressions for $\frac{de}{d\tau}$ and $\frac{dn}{d\tau}$ change by more than 30% in the truncation.

We found significant differences in the bifurcation behaviors of the transformed lactotroph model (4.1) immediately before the truncation of quadratic and higher-order

terms and after truncation. In particular, in the un-truncated system, at $(C, g_A) = (0.5, 4)$, the periodic orbit born in the Hopf bifurcation undergoes a fold and then a period-doubling bifurcation. In the truncated system, the periodic orbit is initially very close to the periodic orbit of the system before truncation. However, it grows quickly as g_K increases and vanishes in a canard explosion that ends in a homoclinic bifurcation with an equilibrium far from the singular Hopf equilibrium before the value of g_K where the fold bifurcation appears in the system before truncation is reached. Figure 4.5 shows the two families of periodic orbits in phase space. Note that in both families, large quickly-growing periodic orbits follow slow manifolds along segments that can approximately be parameterized as $(v, e, n) = (v, k_1 v^2, k_2 v^2)$, where k_1 and k_2 are parameter-dependent constants. This feature is a consequence of the fact that the critical manifold has the shape of a parabolic cylinder where $e \approx v^2$ (see also [24]). While both families end in canard explosions that conclude with a homoclinic bifurcation, the positions of the equilibrium at the homoclinic bifurcation are substantially different in the two cases.

4.4 Analysis of mixed-mode oscillations

This section uses the bifurcation data for system (4.1) from the previous section, together with the bifurcation analysis of the singular Hopf normal form from [24] to predict the onset of mixed-mode oscillations in system (4.1). We subsequently track the MMOs as g_K increases, and observe how the mixed-mode behavior gradually morphs into relaxation oscillations.

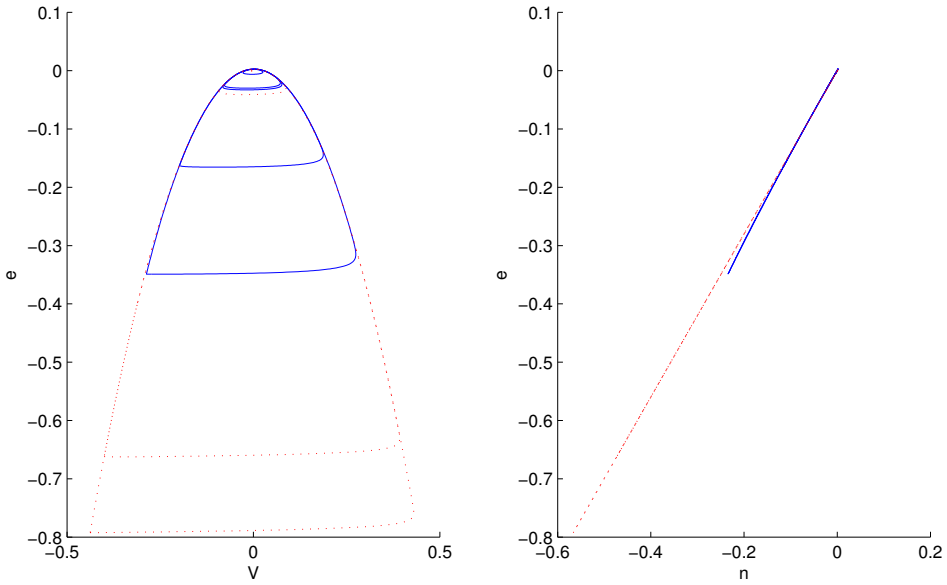

Figure 4.5: Phase portrait showing sample periodic orbits from families of periodic orbits at $C = 0.5, g_A = 4$, for the transformed system (4.1) before (solid blue lines) and after the truncation described in Section 4.2.1 (dotted red). The smallest periodic orbits occur shortly after the Hopf bifurcation, the largest periodic orbits are near-homoclinic equilibria that are located at the bottom-left corner of the largest blue and dotted red trajectories in the left pane.

4.4.1 Variation of g_K

We fix parameters $C = 0.5, g_A = 4$ in system (4.1) for the remainder of this section. Recall that system (4.1) then has a subcritical singular Hopf bifurcation at $g_K = 3.59376$. The equilibrium point undergoing Hopf bifurcation persists for values of g_K in the interval $[3, 15]$. We denote the equilibrium at g_K by $E(g_K)$. There is a folded singularity close to the equilibrium, we will denote it by $FS(g_K)$.

As g_K decreases from the Hopf point, the saddle periodic orbit born in the Hopf

bifurcation grows and undergoes a fold bifurcation at $g_K = 3.57361$. As we follow the family of periodic orbits further, with g_K now increasing, the family undergoes a period-doubling bifurcation at $g_K = 3.57367$. As g_K increases further past the Hopf parameter value, the singular Hopf equilibrium $E(g_K)$ loses stability and is now a saddle-focus with a two-dimensional unstable manifold. According to the analysis in [24], the unstable manifold of the equilibrium intersects a repelling branch of the slow manifold. These circumstances allow MMOs to occur if there is a suitable return mechanism that allows trajectories that have escaped the fold region to return to $E(g_K)$ via an attracting branch of a slow manifold. The following paragraphs present a case study supporting that subcritical singular Hopf bifurcation indeed almost exactly marks the onset of MMOs when $C = 0.5$ and $g_A = 4$.

We will in the following consider the fates of trajectories passing through small perturbations $E^p(g_K) := E^p(g_K) + (10^{-5}, 0, 0)$ and $FS^p(g_K) := FS^p(g_K) + (10^{-5}, 0, 0)$ of the equilibrium $E(g_K)$ and the folded singularity $FS(g_K)$. The results below will show that the size of the perturbation is unimportant as long as the time taken to diverge from the unstable equilibrium is not too large and the size of the perturbation remains small relative to the distance between $E(g_K)$ and $FS(g_K)$.

At $g_K = 3.59376 - 0.0001$, i.e., just before the Hopf bifurcation, both $E^p(g_K)$ and $FS^p(g_K)$ converge to the equilibrium point, which is a sink.

At the Hopf bifurcation, which is subcritical, the equilibrium turns into a saddle-focus. At $g_K = 3.59376 + 0.0001$, i.e. just after the Hopf bifurcation, trajectories through both $E^p(g_K)$ and $FS^p(g_K)$ exhibit MMO behavior with visually indistinguishable trajectories, as shown in Figure 4.6: trajectories approach the equilibrium along a stable manifold, then spiral away from it in the two-dimensional unstable manifold, and make an excursion that involves passages along slow manifolds and "jumps" between

different branches of slow manifold, before returning to the equilibrium point and repeating the process. After a single big excursion from the fold region, the trajectories no longer come close to the folded singularity.

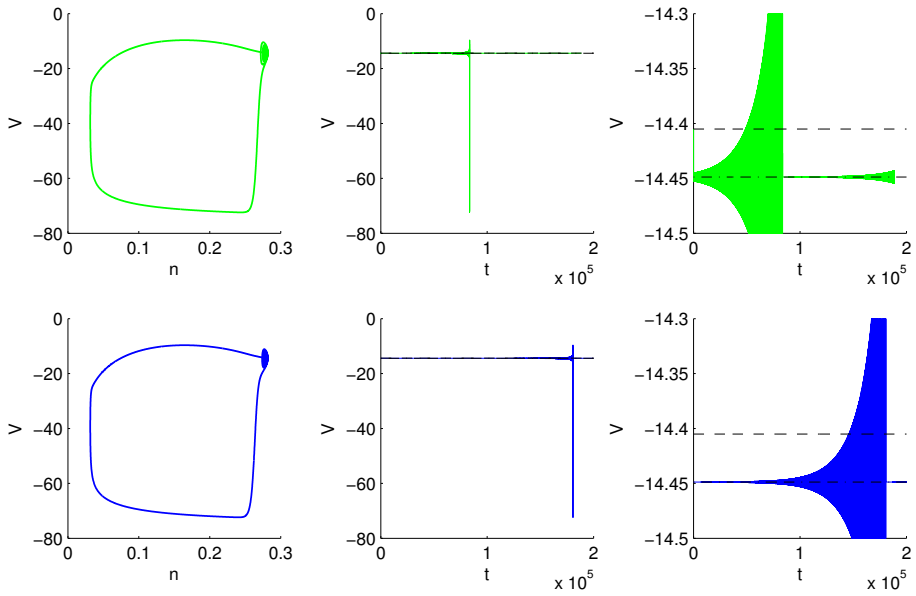

Figure 4.6: MMOs in system (4.1), at $C = 0.5, g_K = 3.59376 + 0.0001, g_A = 4$. The top panes show visualizations of an MMO trajectory (green) beginning close to the folded singularity. Initial transient behavior is not shown here. In the top middle and top right pane, the V-coordinates of the folded singularity and equilibrium point are indicated using a dashed and dashed-dotted line respectively. The bottom pane shows similar diagrams for a trajectory beginning close to the equilibrium. Note that both trajectories spend long periods of time close to the equilibrium point.

Note that at a parameter g_K extremely close and possibly slightly smaller than that of the subcritical Hopf bifurcation, we still expect MMOs to be present: while the equilibrium point is a sink, its basin of attraction only extends slightly in the direction of the two-dimensional complex eigenspace of the vector field's linearization at the equi-

librium. Trajectories approaching the equilibrium therefore have to be extremely close to the stable manifold in order to lie in the equilibrium's basin of attraction. A related discussion of subcritical Hopf-homoclinic bifurcations can be found in [26].

As the g_K increases toward $g_K = 15$, trajectories starting at the folded singularity or singular Hopf equilibrium point no longer return as close to the equilibrium point, and they do not spiral as strongly as for smaller g_K just after the singular Hopf bifurcation. Some spiraling is still visible at $g_K = 4$ (see Figure 4.7), while none can be seen at $g_K = 6$ (see Figure 4.8).

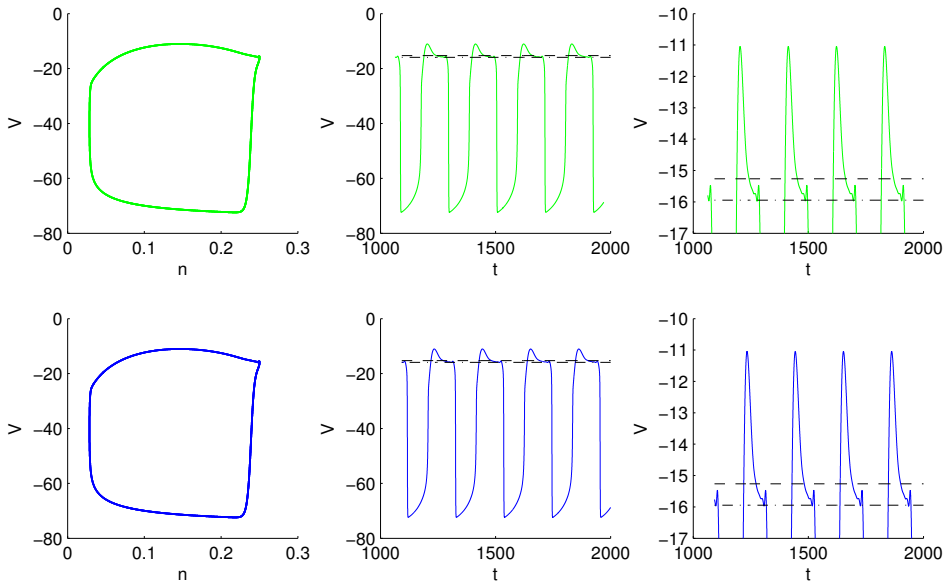

Figure 4.7: MMOs in system (4.1), at $C = 0.5, g_K = 4, g_A = 4$. Panes as in Figure 4.6 above. Note that neither trajectory spends long periods of time close to the equilibrium anymore.

At $g_K = 15$, the oscillations have morphed into a single mode relaxation oscillation (see Figure 4.9).

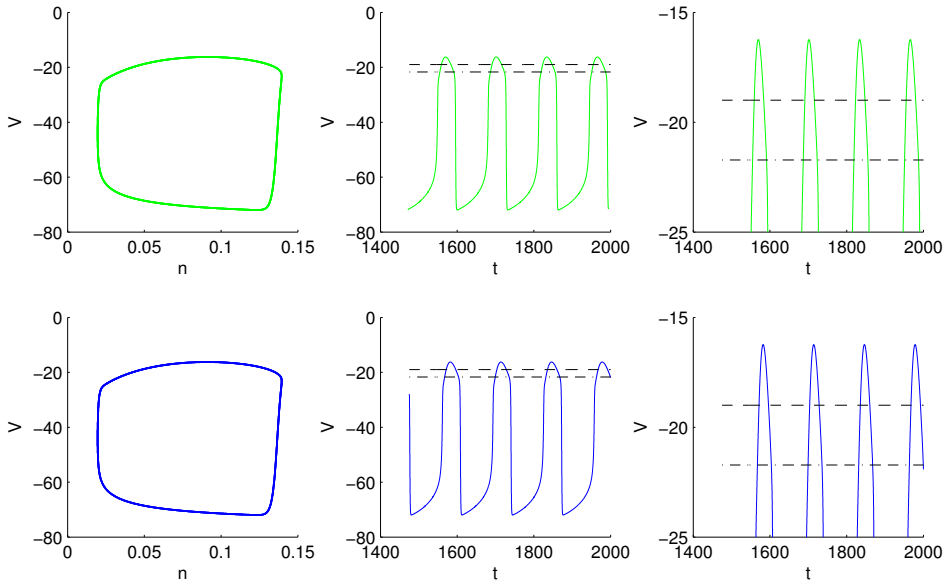

Figure 4.8: Trajectories in system (4.1), at $C = 0.5, g_K = 6, g_A = 4$. Panes as in Figure 4.6 above. Note that the time series no longer include visible mixed-mode oscillations. Moreover, the folded singularity nor the equilibrium visibly influence the course of the trajectory.

4.4.2 Variation of g_K and g_A

Repeating the analysis from Subsection 4.4.1 in which g_K varies for $g_A = 0.4$ and $g_A = 20$, we observed patterns almost identical to those from Subsection 4.4.1.

For very small values of g_A, such as $g_A = 0.03$, we observe that while MMOs exist, the reinjection into the fold region occurs at a substantial distance from the stable manifold of the singular Hopf equilibrium point. As a result, the MMO trajectory remains at an intermediate distance to the stable manifold only for a short period of time, before spiraling away from the equilibrium point and exiting the fold region after a small number of turns. This is shown in Figure 4.10 (top two diagrams). Note in particular

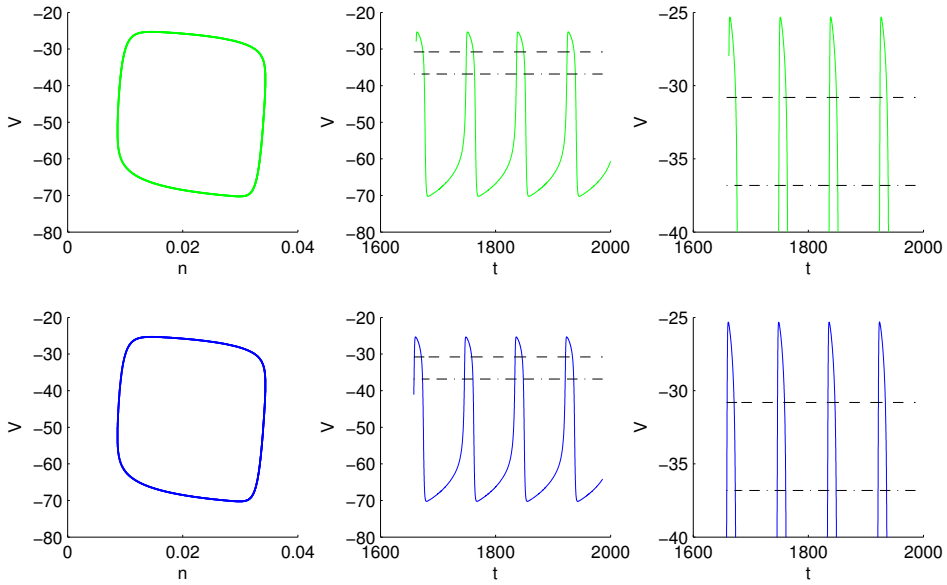

Figure 4.9: Trajectories in system (4.1), at $C = 0.5, g_K = 15, g_A = 4$. Panes as in Figure 4.6 above. The time series now show relaxation oscillation rather than MMO behavior.

that small-amplitude oscillations only begin after the trajectory has passed the folded singularity. For even smaller values of g_A, the large-amplitude oscillation has the shape of a relaxation oscillation and is no longer close to either the singular Hopf equilibrium or the folded singularity. This is illustrated for $g_A = 0.004$ in Figure 4.10 (bottom two diagrams).

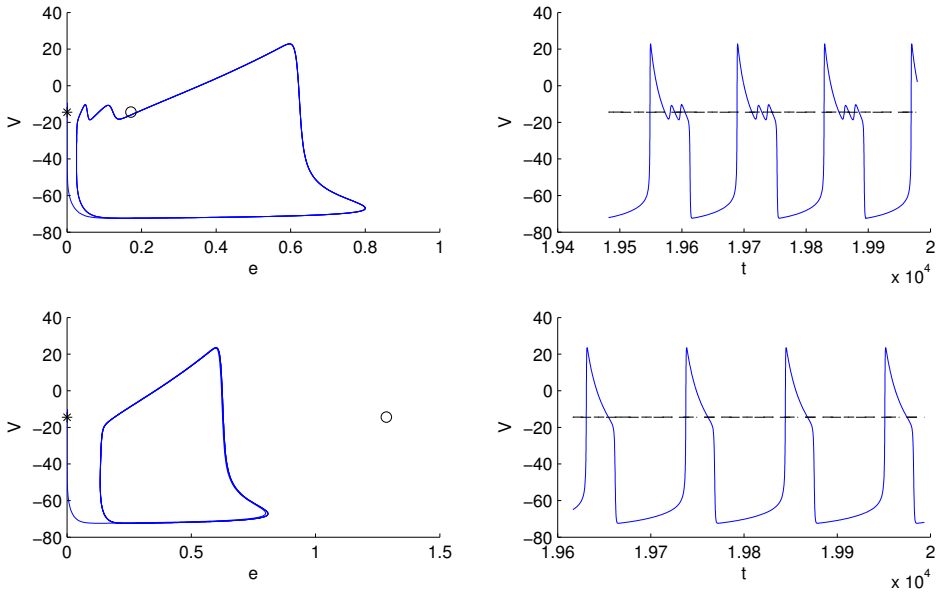

Figure 4.10: Trajectories in system (4.1), at $C = 0.5, g_K = 3.5935$. The top two panes show segments of a trajectory at $g_A = 0.03$, while the bottom two panes show segments of trajectory at $g_A = 0.004$. Both parameters lie to the right of the Hopf bifurcation curve. In the left panes, the singular Hopf equilibrium point as well as the folded singularity have been marked with a black star and a black circle respectively. Note the three small-amplitude oscillations present in the top trajectory. No small-amplitude oscillations are present in the trajectory in the bottom pane.

CHAPTER 5

RIGOROUS ENCLOSURES OF A SLOW MANIFOLD

Invariant manifolds and their intersections are important features that organize qualitative properties of dynamical systems. Three types of manifolds have been prominent in the subject: (1) compact invariant tori [45, 58], (2) stable and unstable manifolds of equilibria and periodic orbits, see e.g. [6, 7, 8, 14, 31, 39, 55, 70], and (3) slow manifolds of multiple time scale systems [12, 14, 23, 34]. Interval arithmetic and verified computing have been used extensively to give rigorous estimates and existence proofs for invariant tori and occasionally to locate stable and unstable manifolds, but the methods presented in this chapter are the first to employ these methods to locate slow manifolds. Each of these three cases poses numerical challenges to locate the manifolds.

Many methods that locate invariant tori assume that the flow on the tori is smoothly conjugate to a constant flow with dense orbits. Existence of this conjugacy confronts well known small divisor problems and the winding vector of the flow must satisfy diophantine conditions in order for this problem to be solvable. Typically, the numerical methods produce a Fourier expansion of the conjugacy which is determined up to a translation. The manifolds are located by projecting onto a discrete set of Fourier modes and solving a fixed point equation for the coefficients of the conjugacy.

The computation of stable and unstable manifolds of equilibria and periodic orbits is a "one-sided" boundary value problem. In the case of an equilibrium point of an analytic vector field, the local stable and unstable manifolds are analytic graphs that have convergent asymptotic expansions whose coefficients can be determined iteratively. The most challenging aspect of computations of two-dimensional manifolds arises from the way that trajectories do or do not spread out in the manifold as one departs from the equilibrium or periodic orbit. As illustrated by the Lorenz manifold [39], the manifolds

can twist and fold in ways that present additional geometrical complications for numerical methods. The development of rigorous bounds for these invariant manifolds follows similar principles to the verified computation of individual trajectories.

Slow manifolds of multiple time scale systems present unique theoretical and numerical challenges compared to the computation of invariant tori and (un)stable manifolds. The first of these challenges is that theory is developed primarily in terms of "small enough" values of the parameter ϵ measuring the time scale ratio of a slow-fast system. Numerically, one always works with specific values of ϵ. The convergence of trajectories as $\epsilon \to 0$ is singular, making it difficult to develop methods framed in terms of asymptotic expansions in ϵ. Divergent series are the rule rather than the exception in this context. The rich history of numerical integration methods for stiff systems and the large literature on reduction methods for kinetic equations of chemical systems reflect the difficulty of computing attracting slow manifolds, the simplest case for this problem. Computing slow manifolds of saddle-type presents the additional challenge that most nearby trajectories diverge from the slow manifold on the fast time scale in both forward and backward time. The second theoretical difficulty in finding slow manifolds is that they are only locally invariant in most problems of interest. The local invariance is accompanied by a lack of uniqueness: possible manifolds intersect fast subspaces in open sets whose diameter is exponentially small in ϵ; i.e., bounded by $\exp(-c/\epsilon)$ for a suitable $c > 0$. Methods based upon root finding of a discretized set of equations must choose a specific solution of the discretized equations. No rigorous numerical methods to compute slow manifolds besides the method presented here exist.

The purpose of this chapter is to compute approximations of slow manifolds that are guaranteed to be of a certain accuracy. This is achieved by computing two approximations that enclose the slow manifold. The two approximations of the slow manifold are

triangulated surfaces transverse to the vector field. To prove the transversality, we use interval analysis, as explained in Section 2.4. This is similar in spirit to the methods developed in [18] to study the phase portraits of planar polynomial vector fields. Even in the planar case the verified computation of phase portraits is a challenging task, and the few methods that exist include [18, 32].

5.1 Set-up and notation

To explain the methods we introduce in the simplest terms, we present the method for slow-fast systems that have two slow variables and one fast variable and use the singular Hopf normal form (2.6) as a test case. To simplify notation, we denote the two slow variables by y and z, i.e., from now on $y \in \mathbb{R}$, and the vector field in the slow variables is denoted by $g = (g_y, g_z)$. We also assume that f, g_y, and g_z are independent of ϵ. To summarize, the systems we study are of the following form:

$$\begin{aligned} \epsilon \dot{x} &= f(x, y, z) \\ \dot{y} &= g_y(x, y, z) \\ \dot{z} &= g_z(x, y, z), \end{aligned} \tag{5.1}$$

where $x, y, z \in \mathbb{R}$, and $f, g_y, g_z : \mathbb{R}^3 \to \mathbb{R}$. We will sometimes use the notation $F = (f, g_y, g_z)$.

In principle, the methods generalize to the case of codimension-one slow manifolds, and the definitions and existence proofs in Sections 5.2 and 5.3 have obvious higher-dimensional analogues. In practice, however, due to the scarcity of tools for computational geometry in higher dimensions, implementing a higher-dimensional version would be a significant extension of the work described in here. We comment on generalizations from the setting of systems with two slow and one fast variable in the

discussion at the end of this chapter, but leave consideration of further details to future work.

5.2 Overview of the method

This section describes our method to compute enclosures of the slow manifold of a slow-fast system of the form (5.1). We start by giving an overview of the main ideas of the method. There are five main steps in the algorithm:

1. triangulation of the critical manifold,
2. computing the $O(\epsilon)$ correction term for the slow manifold,
3. constructing left and right perturbations of the slow manifold,
4. proving that the left and right perturbations enclose the manifold, and
5. tightening the enclosure by contracting the left and right perturbations towards each other.

The first step is to compute a triangulation of the critical manifold which is adapted to the critical manifold's geometry. The manifold is defined implicitly by the condition $f(x, y, z) = 0$. In the example we consider in Section 5.4, we solve this equation to obtain explicit expressions for the functions of the form $x = h_0(y, z)$ whose graphs lie in the critical manifold. Alternatively, one computes approximations to h_0 using, e.g., automatic differentiation and continuation procedures. There are many software packages to compute triangulations of surfaces; we use CGAL [75] via its MATLAB interface. When a part of the critical manifold is represented as the graph of a function h_0, its domain in the plane of the slow variables can be triangulated, and then this triangulation can be lifted to the graph, as illustrated in Figure 5.1. For the triangles in

the lifted triangulation to have similar diameters, we choose triangles in the plane of the slow variables to have diameters that depend upon the gradient of h_0. We stress that the rest of the algorithm is independent from how the triangulation of the critical manifold is constructed. Rather than using axis parallel patches, one could, e.g., use approximate trajectory segments of the reduced system to determine the piece of the domain of the slow variables, where the slow manifold is computed.

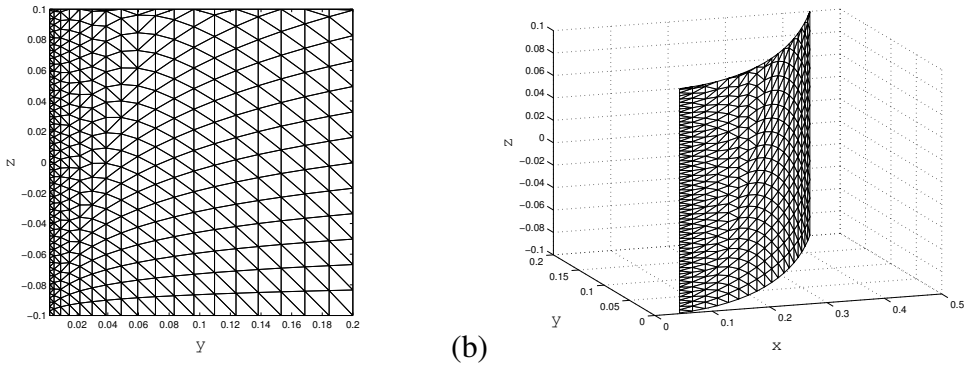

(a) (b)

Figure 5.1: The mesh generated for the example in Section 5.4. There is a fold at $\{y = 0\}$. (a) The Delaunay triangulation of the (y, z) plane that is generated by the geometry adapted mesh points. (b) The lift of the triangulation to the critical manifold.

We compute an approximation to the slow manifold using a procedure similar to that employed in stiff integrators that use Rosenbrock methods [27]. The tangent space to the critical manifold is orthogonal to the vector df. According to Fenichel theory, the slow manifold is $O(\epsilon)$ close to the critical manifold in the C^1 topology, so its tangent space is approximately normal to df. At a point (x, y, z) in the (lifted) triangulation of S_0, we look for a nearby point $(x + \delta, y, z)$ at which the vector field is orthogonal to $df(x, y, z)$. Since $f(x, y, z) = 0$ and the normal hyperbolicity implies that $\partial_x f \neq 0$,

$$\delta = -\epsilon \frac{(\partial_y f g_y + \partial_z f g_z)}{(\partial_x f)^2}$$

is an approximate solution to this equation. Setting δ to this value, we take $(x + \delta, y, z)$ as a point of the triangulation of the approximate slow manifold. The critical manifold and the approximation to the slow manifold are illustrated in Figure 5.2 (a) and (b), respectively. We next perturb this triangulation of the approximate slow manifold in both directions parallel to the x-axis, as in Figure 5.2 (c), by a factor $2^{j-6}\delta$, where j is a natural number that will be specified later. In case that δ is very small, we replace it by an $O(\epsilon^2)$ term. This procedure yields two surfaces that are candidates for the enclosing surfaces that we seek.

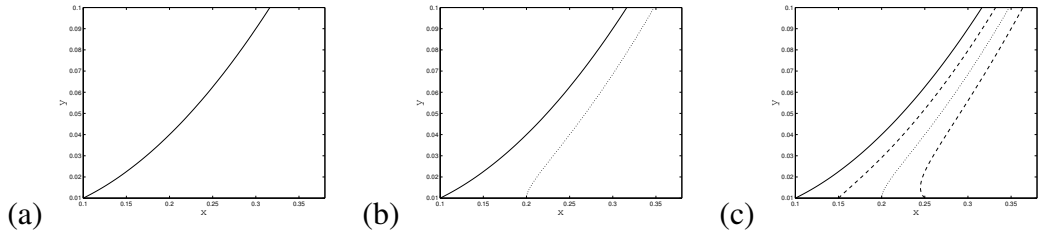

Figure 5.2: Construction of the enclosing triangulations. This figure shows the projection on (x, y) coordinates of: (a) the critical manifold (solid). (b) The critical manifold (solid) as well as the slow manifold (dotted). (c) The critical manifold (solid), the slow manifold (dotted), and the two enclosing surfaces (dashed).

To verify that the surfaces enclose the slow manifold, we check whether the flow of the full system (5.1) is transversal to the candidate surfaces. As the candidate surfaces are piecewise linear, we have to define what we mean by transversality at the edges and vertices of the triangulation.

Definition 5.2.1. *Let $\mathcal{T} \subset \mathbb{R}^3$ be a triangulated, piecewise linear two-dimensional manifold $\mathcal{T} = \bigcup T_i$. Since $\mathcal{T}$ is a manifold, it locally separates R^3 into two sides. We say that a vector v is transverse to $\mathcal{T}$ if v and $-v$ point to opposite sides of $\mathcal{T}$. A smooth vector field is transverse to $\mathcal{T}$ if it is transverse to $\mathcal{T}$ at every point of $\mathcal{T}$.*

Figure 5.3(a) illustrates this definition. Trajectories of the flow generated by F will all cross $\mathcal{T}$ from one side to another if F is transverse to $\mathcal{T}$. If $\mathcal{T}_1$ and $\mathcal{T}_2$ are triangulated surfaces transverse to the flow with opposite crossing directions, then they form enclosing surfaces for the slow manifold we seek.

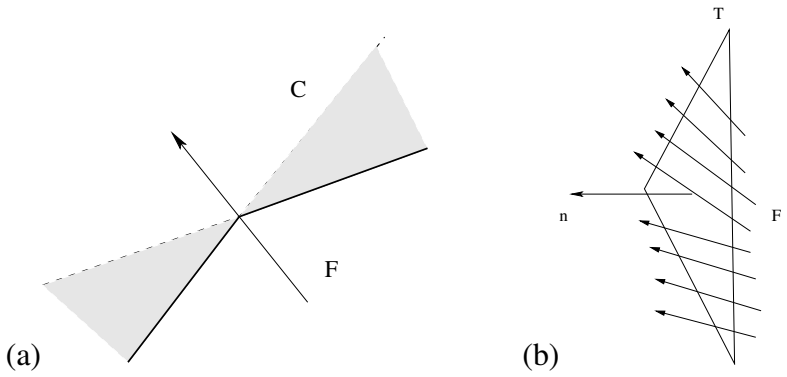

Figure 5.3: (a) Transversality check on an edge of the triangulation. F is transversal if it does not belong to the cone C. (b) Transversality check on one face of the triangulation. To verify that the flow intersects the surface transversally, it suffices to prove that the vector field is never orthogonal to the normal of the surface, which is a constant vector. So, we compute the range of $F \cdot n$, and prove that it does not contain 0.

Transversality is a condition that is local to each face of the triangulation, so we can check it on each face of the triangulation separately. To check the transversality condition on one face, we estimate the range of the inner product of the vector field with the normal of the face, as illustrated in Figure 5.3(b). Details about the existence of locally invariant, normally hyperbolic manifolds inside the enclosure are addressed in Section 5.3 below.

The final part of the algorithm is to iteratively update the location of the vertices by moving them towards each other in small steps along the fast direction. We check that the transversality properties still hold, see Figure 5.4. This tightening step is stopped when no more vertices can be moved. Note that the vertices of all 4 triangulations (of

the critical manifold, the approximate slow manifold, and the two perturbed manifolds) all have the same (y, z) components.

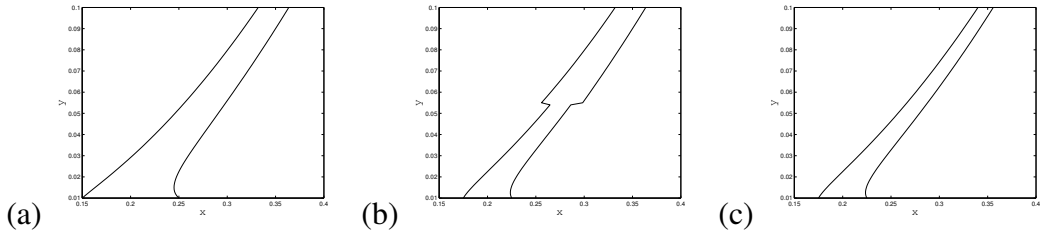

Figure 5.4: Updating the enclosures of the slow manifold. This figure show the projection on (x, y) coordinates of: (a) The initial enclosures. (b) The enclosures are updated vertex wise, here the first half of the vertices are updated. (c) The new enclosure.

5.3 Existence of locally invariant manifolds

The method outlined in the previous section constructs two triangulated surfaces, in the phase space of a slow-fast system, that are transversal to the flow for the given ϵ. In this section we discuss the existence of locally invariant manifolds enclosed between these two triangulations. We denote the two enclosing surfaces by $\mathcal{L}$ and $\mathcal{R}$, and the region enclosed between them by C. Note that $\mathcal{L}$ and $\mathcal{R}$ are graphs over the same compact region, so C is well defined. Specifically, if for some compact set of slow variables D, $\mathcal{L} = \{(x, y, z) \, : \, x = h_l(y, z), (y, z) \in D\}$, $\mathcal{R} = \{(x, y, z) \, : \, x = h_r(y, z), (y, z) \in D\}$, then $C = \{(x, y, z) \, : \, x \in [h_l(y, z), h_r(y, z)], (y, z) \in D\}$. We would like to claim that there is a locally invariant manifold inside of C which is a graph over the slow variables. We must thus verify that it is possible to choose a subset of C which is a C^1 manifold, locally invariant, and whose projection onto the domain in the slow variables is bijective. We start this section by defining *computable slow manifolds* as objects associated to a fixed ϵ. Similar

to a slow-manifold, a computable slow manifold is not unique. Informally, a computable slow manifold is a manifold close to the critical manifold where the flow is slow. We measure slowness by comparing the slopes of trajectories within our enclosure with the slope of the critical manifold. The relative slope is defined as a bound on the slope of trajectories divided by the slope of the critical manifold:

$$s(\epsilon) = \max_{C} \frac{\frac{|\dot{x}|}{|\dot{y}| + |\dot{z}|}}{\left(\left|\frac{\partial h_0(y,z)}{\partial y}\right| + \left|\frac{\partial h_0(y,z)}{\partial z}\right|\right)}. \tag{5.2}$$

Definition 5.3.1. *A computable slow manifold is a C^1 locally invariant, normally hyperbolic manifold, of the same dimension as the critical manifold, which projects injectively along the fast variable to the critical manifold, such that its relative slope satisfies $s(\epsilon) \leq \frac{1}{\sqrt{\epsilon}}$.*

Note that the order of $s(\epsilon)$ is $O\left(\frac{1}{\epsilon}\right)$ away from the slow manifold, so the definition is consistent with the standard perturbative definition of slow manifolds [34]. Slow manifolds are widely used in studies of slow-fast systems arising from biological or chemical models. However, computable slow manifolds are often the objects that are identified in applications: a locally invariant manifold at a *fixed* value of ϵ that follows the critical manifold closely, and on which the flow is slow [10, 23, 30]. This concept is captured by the definition of the computable slow manifold. Thus, our enclosures method gives a general and robust method to compute where candidates for such manifolds might lie in the phase space.

We will explain why computable slow manifolds exist within C in the following special case, which is sufficient for the purpose of this exposition.

Assumption 5.3.2. *Assume that:*

(I) All trajectories of C reach its boundary in forward and backward time.

(II) The boundary of C, ∂C is piecewise smooth. Tangencies of the vector field with ∂C are quadratic (i.e., folds in the sense of singularity theory), and these tangencies occur along smooth curves that connect $\mathcal{L}$ and $\mathcal{R}$.

(III) There are invariant horizontal and vertical cone fields (defined in Subsection 5.4.5) on C, and the vertical invariant cone field contains the fast direction of the vector field on C.

Assume that the vector field is inward on $\mathcal{L}$ and $\mathcal{R}$ and denote by C_{in} and C_{out} the sets in $\partial C - \mathcal{L} - \mathcal{R}$ where the vector field points inward and outward, respectively. Choose a smooth curve, $x = r_0(y, z)$, in $\partial C - \mathcal{L} - \mathcal{R}$ such that the projection of the curve to the slow variables contains the projection of C_{in} to the slow variables, and points on the curve on C_{out} are images of the flow of points on the curve on C_{in}. Flow this graph forward until each trajectory leaves C. The set swept out by these trajectory segments is:

$$S_\epsilon := \{\phi_t(x, y, z) \ : x = r_0(y, z), \phi_t(x, y, z) \in C\}. \tag{5.3}$$

The set S_ϵ is well-defined, as smooth as r_0 and the vector field, and diffeomorphic to its projection onto the critical manifold S_0. Inflowing trajectories of C must exit through C_{out}. The exit time is uniformly bounded, since C is compact. Hence, S_ϵ is well defined. The existence of invariant cone fields, with a normal vertical cone field containing the fast direction, ensures that S_ϵ is a graph over the slow variables, and thus diffeomorphic to the corresponding part of the critical manifold. The final requirement of the definition of the computable slow manifold, that the relative slope is small, yields a quantitative requirement on the tightness of $\mathcal{L}$ and $\mathcal{R}$.

5.4 Detailed description of the method for the singular Hopf normal form

In this section we give a detailed description of our method for computing enclosures of slow manifolds, applying it to the singular Hopf normal form as an example. Most of the details generalize to any system of the form (5.1). In the description, we comment on non-trivial differences between the general case and the example at hand.

5.4.1 Constructing the triangulation

The first step of our algorithm is to triangulate a portion of the critical manifold S_0. On a normally hyperbolic piece of the critical manifold, $\partial_x f \neq 0$. The implicit function theorem implies there is locally a function $h_0(y, z)$, such that $f(h_0(y, z), y, z) = 0$. In the singular Hopf normal form, h_0 is given explicitly as $h_0^{\pm}(y, z) = \pm\sqrt{y}$ with domain $D = [y_m, y_M] \times [z_m, z_M] \subset \mathbb{R}^2$. For other systems, any suitable method for finding a sufficiently accurate approximation to $h_0(y, z)$ can be used.

To construct the vertices of a Delaunay triangulation of S_0, as shown in Figure 5.1(a), we start with a triangulation of the domain of h_0, but want the diameter of the triangles on S_0 to be almost uniform. Setting $\kappa(y, z) = \|\nabla h\|$, $\tilde{k} = \sqrt{(y_M - y_m)^2 + (z_M - z_m)^2}/d$, and

$$k(y, z) := \frac{\tilde{k}}{1 + \kappa(y, z)},$$

with $d \in \mathbb{Z}_+$ to be chosen later, we select the following points in the (y, z) plane as

vertices of a triangulation:

$$
\begin{aligned}
(y_0, z_0) &:= && (y_m, z_m) && \\
(y_i, z_0) &:= && (y_{i-1} + k(y_{i-1}, z_0), z_0), && \text{if} \quad y_{i-1} < y_{i-1} + k(y_{i-1}, z_0) < y_M, \\
(y_i, z_0) &:= && (y_M, z_m), && \text{if} \quad y_{i-1} < y_M \leq y_{i-1} + k(y_{i-1}, z_0), \qquad (5.4) \\
(y_i, z_j) &:= && (y_i, z_{j-1} + k(y_i, z_{j-1})), && \text{if} \quad z_{j-1} < z_{j-1} + k(y_i, z_{j-1}) < z_M, \\
(y_i, z_j) &:= && (y_i, z_M), && \text{if} \quad z_{j-1} < z_M \leq z_{j-1} + k(y_i, z_{j-1}), \\
& && 0 \leq i \leq I,\ 0 \leq j(i) \leq J_i && \qquad (5.5)
\end{aligned}
$$

Note that these points are aligned along lines parallel to the fold curve $x = y = 0$ where $\partial_x f = 0$.

Let $\mathcal{T}$ denote the Delaunay triangulation generated by the set

$$\{(y_i, z_i) : 0 \leq i \leq I, 0 \leq j(i) \leq J_i\},$$

and $\mathcal{K}_0$ its lift to S_0, using the map $\pi_0^{-1} : (y, z) \mapsto (h_0(y, z), y, z)$. Clearly π_0^{-1} is a homeomorphism; i.e., the set of vertices, edges, and faces of $\mathcal{K}_0$, denoted by $V(\mathcal{K}_0)$, $E(\mathcal{K}_0)$, and $F(\mathcal{K}_0)$, are defined by $\pi_0^{-1}(V(\mathcal{T}))$, $\pi_0^{-1}(E(\mathcal{T}))$, and $\pi_0^{-1}(F(\mathcal{T}))$, respectively. $\mathcal{T}$ and $\mathcal{K}_0$ are shown in Figures 5.1(a) and 5.1(b), respectively.

5.4.2 Constructing perturbed triangulations

Our next step is to perturb $\mathcal{K}_0$, as illustrated in Figure 5.2, so that it lies closer to the computable slow manifold S_ϵ we are trying to enclose. Fenichel theory, [34], guarantees that for $\epsilon > 0$ sufficiently small, S_ϵ is the graph of a function $h_\epsilon(y, z)$ with domain D and $h_\epsilon(y, z) - h_0(y, z) = O(\epsilon)$. To compute triangulations $\mathcal{K}_\epsilon$ that approximate S_ϵ, we write h_ϵ in the form

$$h_\epsilon(y, z) = h_0(y, z) + \epsilon h_1(y, z).$$

Substituting into the equation $\epsilon \dot{x}_\epsilon = f(h_\epsilon(y,z),y,z)$, we get that:

$$\begin{aligned} f(h_0(y,z)+\epsilon h_1(y,z)+O(\epsilon^2),y,z)/\epsilon &= \partial_y(h_0(y,z)+\epsilon h_1(y,z))\dot{y}+\partial_z(h_0(y,z)+\epsilon h_1(y,z))\dot{z} \\ &= \partial_y h_0(y,z)\dot{y}+\partial_z h_0(y,z)\dot{z}+O(\epsilon) \\ &= \partial_y h_0(y,z)g_y(h_0(y,z),y,z) \\ &\quad +\partial_z h_0(y,z)g_z(h_0(y,z),y,z)+O(\epsilon). \end{aligned} \tag{5.6}$$

To compute $\partial_y h_0$ and $\partial_z h_0$, we use that $f(h_0(y,z),y,z)=0$, and hence

$$\partial_y h_0(y,z) = -\frac{\partial_y f(h_0(y,z),y,z)}{\partial_x f(h_0(y,z),y,z)},$$

and

$$\partial_z h_0(y,z) = -\frac{\partial_z f(h_0(y,z),y,z)}{\partial_x f(h_0(y,z),y,z)}.$$

In addition, since $f(h_0(y,z),y,z)=0$,

$$f(h_\epsilon(y,z),y,z) = \epsilon \partial_x f(h_0(y,z),y,z)h_1(y,z)+O(\epsilon^2). \tag{5.7}$$

Thus, we can solve equation (5.7) for $h_1(y,z)$, up to $O(\epsilon)$, and substitute for $f(h_\epsilon(y,z),y,z)$ using (5.6), obtaining

$$h_1(y,z) = -\frac{\partial_y f(h_0(y,z),y,z)g_y(h_0(y,z),y,z)+\partial_z f(h_0(y,z),y,z)g_z(h_0(y,z),y,z)}{(\partial_x f(h_0(y,z),y,z))^2}+O(\epsilon),$$

which in our case, considering $h^+(y,z)$, reads:

$$h_1^+(y,z) = \frac{\sqrt{y}-z}{4y}. \tag{5.8}$$

For $h^-(y,z)$, which we will use in Section 5.6, we get:

$$h_1^-(y,z) = \frac{-\sqrt{y}-z}{4y}. \tag{5.9}$$

We put $\pi_\epsilon^{-1} : (y,z) \mapsto (h_0(y,z)+\epsilon h_1(y,z),y,z)$, and define:

$$\mathcal{K}_\epsilon := \pi_\epsilon^{-1} \circ \pi_0(\mathcal{K}_0).$$

$\mathcal{K}_\epsilon$ is our approximation to the slow manifold, shown together with S_0 in Figure 5.2(b). Heuristically, it is $O(\epsilon^2)$ to S_ϵ at the vertex points.

Let σ_c denote the following map that moves points parallel to the x-axis:

$$\sigma_c : (x, y, z) \mapsto (x + c \max\left(|h_1(y, z)|, \frac{\epsilon^2}{|c|}\right), y, z). \tag{5.10}$$

We define our candidate enclosing surfaces as:

$$\mathcal{L}_{\epsilon,N} := \sigma_{-\epsilon/N}(\mathcal{K}_\epsilon) \tag{5.11}$$

$$\mathcal{R}_{\epsilon,N} := \sigma_{\epsilon/N}(\mathcal{K}_\epsilon), \tag{5.12}$$

where $N \in \mathbb{R}_+$. The initial choice for N in our implementation was $N = 64$, but we would have chosen a smaller N if that had failed. The verification step of the algorithm includes a loop that divides N by a factor 2 upon failure and repeats the transversality test. Note that the region that is enclosed by $\mathcal{L}_{\epsilon,N}$ and $\mathcal{R}_{\epsilon,N}$ is disjoint from the critical manifold so long as $N > 1$. The construction of S_0, S_ϵ, $\mathcal{L}_{\epsilon,N}$ and $\mathcal{R}_{\epsilon,N}$ is shown in Figure 5.2.

5.4.3 Verifying the enclosure property

To prove that a slow manifold is located between $\mathcal{L}_{\epsilon,N}$ and $\mathcal{R}_{\epsilon,N}$, it suffices to prove that the vector field (5.1) is transversal to each face of the triangulations, with opposite crossing directions for $\mathcal{L}_{\epsilon,N}$ and $\mathcal{R}_{\epsilon,N}$. For the remainder of this subsection, we restrict our attention to a single triangle. Local transversality, i.e., the verified transversality on each face in the triangulation, implies global transversality of $\mathcal{L}_{\epsilon,N}$ and $\mathcal{R}_{\epsilon,N}$.

Let T be one face in $\mathcal{L}_{\epsilon,N}$ or $\mathcal{R}_{\epsilon,N}$. We denote its vertices by v_1, v_2, and v_3 and its edges by e_{12}, e_{13}, and e_{23} with the edge e_{ij} between the vertices v_i and v_j. To verify

that the vector field is transverse, it suffices to prove that the inner product between the normal of the face and the vector field is non-zero. Note that in contrast to most work on slow-fast systems, this condition, which is the main condition checked by our algorithm, becomes *easier* to verify as $\epsilon \to 0$. The reason is that as $\epsilon \to 0$, the condition becomes essentially one-dimensional. We denote the normal to the face, normalized so that the first component is positive, by $n(T)$. This is possible because the first component is zero exactly at the folds, where the critical manifold fails to be normally hyperbolic. With this notation, the condition that we have to verify is

$$F(x, y, z) \cdot n(T) \neq 0, \quad \text{for all } (x, y, z) \in T. \tag{5.13}$$

Condition (5.13) is equivalent to a verification that

$$F(\lambda_1 v_1 + \lambda_2 v_2 + \lambda_3 v_3) \cdot n(T) \neq 0 \quad \text{for all } \lambda_i \in [0, 1], \lambda_1 + \lambda_2 + \lambda_3 = 1, \tag{5.14}$$

which is an enclosure of the range of a function on a compact domain. This problem is the one we solve with interval analysis. Directly enclosing (5.14) using interval analysis in order to verify that the function is non-zero is, however, not optimal. The reason is that the problem is sufficiently sensitive that we would have to split the λ_i domains into a very fine subdivision, and since this has to be done on each face, such a procedure would be prohibitively slow.

Our actual approach is based on monotonicity; first we prove that $F \cdot n$ is monotone on the face and on its restriction to the edges. Then we compute $F(v_i) \cdot n$ for the three vertices and verify that the interval hull of the results, i.e., the smallest representable interval containing the results, does not contain 0. Note that this amounts to showing that the dot-product does not change sign on the face. We introduce

$$G := \nabla(F \cdot n). \tag{5.15}$$

If $G \neq (0,0,0)$ on all of T, then $F \cdot n$ has no critical points inside of T and we can restrict our attention to the edges, i.e. the boundary of T. Consider an edge $e_{ij} = \{(1-\lambda)v_i + \lambda v_j \; : \; \lambda \in [0,1]\}$, and denote its parametrization by $r(\lambda)$. The scalar product $F \cdot n$ is monotone on the edge if

$$0 \neq \frac{\partial}{\partial \lambda}(F(r(\lambda)) \cdot n) = G \cdot (v_j - v_i).$$

Hence, we arrive at the monotonicity requirements, which for the case at hand are much easier to verify than (5.14):

$$(0,0,0) \notin G(T) \tag{5.16}$$

$$0 \notin G(e_{12}) \cdot (v_2 - v_1) \tag{5.17}$$

$$0 \notin G(e_{13}) \cdot (v_3 - v_1) \tag{5.18}$$

$$0 \notin G(e_{23}) \cdot (v_3 - v_2) \tag{5.19}$$

If the conditions (5.16-5.19) are satisfied we compute

$$F(v_1) \cdot n \sqcup F(v_2) \cdot n \sqcup F(v_3) \cdot n, \tag{5.20}$$

where $\sqcup$ denotes the interval hull. If (5.20) does not contain zero, then the vector field is transversal to the face T. If (5.16) holds but one or more of (5.17-5.19) do not hold, then we add the appropriate $F(e_{ij}) \cdot n$ terms to (5.20).

5.4.4 Improving the bounds

If the previous steps of the algorithm are successful, they yield two surfaces $\mathcal{L}_{\epsilon,N}$ and $\mathcal{R}_{\epsilon,N}$, that have been proven to enclose the part of the slow manifold that is above $[y_m, y_M] \times [z_m, z_M]$ in the (y,z) plane. Since N is fixed after the verification step we henceforth drop the indices on $\mathcal{L}$ and $\mathcal{R}$. Our aim is to produce enclosures that are as

tight as possible, given the mesh size. We, therefore, try to improve the enclosure. The procedure is illustrated in Figure 5.4.

We do this by iteratively updating each of the vertices in the triangulation by moving them towards each other along the segment joining them. This segment is parallel to the x-axis due to our earlier constructions. The moves are done in two steps: (1) a tentative move is made of a vertex, and (2) the transversality conditions of all faces attached to this vertex are verified. When the transversality holds, the vertex is fixed at its new position and we proceed to the next vertex. The efficiency of this procedure will depend on several factors, primarily the ordering of the vertices and how much the vertices are moved. By moving a vertex only a fraction of what seems to be possible, the effect of the ordering of the vertices can be minimized. The penalty of smaller updates is that the procedure has to be run more times. Larger moves might be possible if an appropriate sorting algorithm were used, but we have not found an effective and efficient sorting criterion. Instead, we heuristically determine an update factor that optimizes the accuracy vs complexity. Given a right vertex, v_R, and a left vertex, v_L, such that $\pi_0(v_R) = \pi_0(v_L)$, we move each of them towards each other by an amount

$$\frac{1}{8}\|(v_R - v_L)\|. \tag{5.21}$$

We run the procedure to refine the enclosures of the slow-manifold several times, until no further improvement is possible. The quantity we use to measure the quality of the enclosures is the average distance between the two triangulations at the vertices. Let ι denote the number of vertices of the triangulations; by construction $\mathcal{L}$ and $\mathcal{R}$ have the same number of vertices, edges, and faces. The only difference between $\mathcal{L}$ and $\mathcal{R}$ is the values of the x-coordinates. We put

$$\eta(\mathcal{L}, \mathcal{R}) = \frac{1}{\sqrt{\iota}}\|v_R - v_L\|. \tag{5.22}$$

If the triangulation is fine enough, η will be $O(\epsilon^2)$. This fact is investigated numerically

in Section 5.5.

5.4.5 Cone fields

In order to ensure that there are manifolds inside of the set C enclosed by $\mathcal{L}$ and $\mathcal{R}$, we need to have invariant cone fields on C, as explained in Section 5.3. In this subsection we describe how such cone fields - one horizontal and one vertical - are constructed. Recall, see [35], that a standard horizontal or vertical cone for a phase space with variables (x, y) is a set $\{\gamma||x|| \geq ||y||\}$ or $\{\gamma||y|| \geq ||x||\}$, respectively, and that a cone is the image of a standard cone under an invertible linear map. Equivalently, a cone is the set of points where a non-degenerate indefinite quadratic form is non-negative. Since horizontal and vertical cones are traditionally in the expanding and contracting directions, respectively, we will call the cone in the normal direction the vertical cone, and the cone in the direction of the slow manifold the horizontal cone. Also recall that a cone field is invariant if it is mapped into itself by the derivative of the dynamics, i.e., if the set where the quadratic form is non-negative is mapped by the derivative into the set where the quadratic form at the image point under the map is non-negative.

For the case at hand we will use $\gamma = 1$ for both the horizontal and vertical cones in an appropriate coordinate system, such that the normal direction is in the vertical cone. A cone field is a map that associates a cone to each point of its domain. Given that (2.8) only has one nonlinear component, we will use constant cone fields. To prove that the cone fields are invariant, we solve the variational equation for the time 0.0004 flow map, and use the eigendirections of the derivative of the flow as a basis, in which we represent the standard horizontal and vertical cones with $\gamma = 1$. We verify that the vertical and horizontal cone fields are invariant, and that the vertical cone contains the fast direction,

which ensures that S_ϵ defined in (5.3) projects injectively onto the slow variables, and, thus, is a graph over them. The flow time needs to be large enough for us to be able to prove the separation of the horizontal and vertical directions, but small enough that we do not move away too far in phase space. The value 0.0004 turned out to be a good choice.

5.4.6 Algorithms

An implementation [80] of the method described above has been made using the INTLAB package [76] for interval arithmetic. A detailed description of the main algorithm is given as Algorithm 1. The algorithm that checks if the vector field is transversal to a face is given as Algorithm 2. Algorithm 1 takes a triangulation as input. That triangulation can be computed with any method, not only the one outlined in Section 5.4.1. In Algorithm 2 the function $sign(x)$ returns 0 if $0 \in x$.

5.5 Numerical Results

In this section we describe the results of several experiments illustrating the behavior of the enclosure computations. Given a system and a domain, there are two numbers that can be changed, the number d, which controls the mesh size, and the value of ϵ. In the experiments below, we use the normal form for singular Hopf bifurcation discussed in Chapter 3. We choose the same values of the constants as in the Section 3.1: $\mu = 10^{-2}$, $A = -0.05$, $B = 0.001$, and $C = 0.1$. We enclose the branch of the critical manifold $\{y = x^2\}$ where $x > 0$. The results of four experiments are described below, in each of them we present the results as a plot of η vs ϵ. In the first experiment, we fix the

Algorithm 1: Implementation of the main algorithm

Data: (f, g_y, g_z), h_0, $\mathcal{T}$, ϵ
Result: $\mathcal{L}$, $\mathcal{R}$, η

forall the $(y, z) \in \mathcal{T}$ **do**
  $h_1(y,z) = -\frac{\partial_y f(h_0(y,z),y,z) g_y(h_0(y,z),y,z) + \partial_z f(h_0(y,z),y,z) g_z(h_0(y,z),y,z)}{(\partial_x f(h_0(y,z),y,z))^2}$;
end
$N = 64$;
transversal=false;
$NF = \mathcal{T}.numberOfFaces$;
while $\neg transversal$ & $N > 2^{-18}$ **do**
  $x_{left} = h_0(y,z) + h_1(y,z) - \epsilon/N \max(|h_1(y,z)|, \epsilon N)$;
  $x_{right} = h_0(y,z) + h_1(y,z) + \epsilon/N \max(|h_1(y,z)|, \epsilon N)$;
  if $getTransversality(\mathcal{T}, x_{left}) = -getTransversality(\mathcal{T}, x_{right}) = NF$ **then**
    transversal=true;
  else
    $N = N/2$;
  end
end
if $\neg transversal$ **then**
  exit(FAIL);
end
$\eta = 1$;
$\eta_{new} = 0$;
while $\eta_{new} < \eta$ **do**
  $\eta = \frac{\|x_{left} - x_{right}\|}{\sqrt{\mathcal{T}.\iota}}$;
  $\tilde{x}_{left} = x_{left}$, $\tilde{x}_{right} = x_{right}$;
  forall the $1 \le i \le \iota$ **do**
    $tri = \mathcal{T}.adjacentFaces(i)$;
    $\tilde{x}_{left}(i) = x_{left}(i) + 0.125(x_{right}(i) - x_{left}(i))$;
    if $getTransversality(tri, \tilde{x}_{left}, \mathcal{T}.y, \mathcal{T}.z) =$
    $-getTransversality(tri, x_{right}, \mathcal{T}.y, \mathcal{T}.z) = tri.numberOfFaces$ **then**
      $x_{left}(i) = \tilde{x}_{left}(i)$;
    else
      $\tilde{x}_{left}(i) = x_{left}(i)$;
    end
    $\tilde{x}_{right}(i) = x_{right}(i) - 0.125(x_{right}(i) - x_{left}(i))$;
    if $getTransversality(tri, x_{left}, \mathcal{T}.y, \mathcal{T}.z) =$
    $-getTransversality(tri, \tilde{x}_{right}, \mathcal{T}.y, \mathcal{T}.z) = tri.numberOfFaces$ **then**
      $x_{right}(i) = \tilde{x}_{right}(i)$;
    else
      $\tilde{x}_{right}(i) = x_{right}(i)$;
    end
  end
  $\eta_{new} = \frac{\|x_{left} - x_{right}\|}{\sqrt{\mathcal{T}.\iota}}$;
end
$\mathcal{L} = Triangulate(\mathcal{T}.Triangulation, x_{left}, \mathcal{T}.y, \mathcal{T}.z)$;
$\mathcal{R} = Triangulate(\mathcal{T}.Triangulation, x_{right}, \mathcal{T}.y, \mathcal{T}.z)$;

Algorithm 2: getTransversality(Triangulation,Vertices)

Data: $F = (f, g_y, g_z)$, $\mathcal{T}$(Triangulation,Vertices)
Result: *Intersections*

$NF = \mathcal{T}.numberOfFaces$;
$Intersections = 0$;
forall the $1 \leq i \leq NF$ **do**
  $n = \mathcal{T}.Normal(i)$;
  $(v_1, v_2, v_3) = \mathcal{T}.Vertices(i)$;
  $(e_{12}, e_{13}, e_{23}) = \mathcal{T}.Edges(i)$;
  $G = \nabla(F(\mathcal{T}.Face(i)) \cdot n)$;
  if $0 \in G$ **then**
    $Intersections+ = sign(F(\mathcal{T}.Face(i)) \cdot n)$;
  else
    $G_{12} = \nabla(F(e_{12}) \cdot n) \cdot e_{12}$, $G_{13} = \nabla(F(e_{13}) \cdot n) \cdot e_{13}$, $G_{23} = \nabla(F(e_{23}) \cdot n) \cdot e_{23}$;
    if $0 \notin G_{12}G_{13}G_{23}$ **then**
      $Intersections+ = sign(F(v_1) \cdot n \sqcup F(v_2) \cdot n \sqcup F(v_3) \cdot n)$;
    else
      forall the $a \in \{12, 13, 23\}$ **do**
        if $0 \in G_a$ **then**
          $F_a = F(e_a) \cdot n$
        else
          $F_a = F(v_{a_1}) \cdot n \sqcup F(v_{a_2}) \cdot n$
        end
      end
      $Intersections+ = sign(F_{12} \sqcup F_{13} \sqcup F_{23})$;
    end
  end
end

domain as a small strip where $y \in [0.01, 0.2]$ and $z \in [-0.01, 0.01]$ and give the results for several values of ι (defined implicitly by changing d). In the second, we take a square domain where $y \in [0.01, 0.2]$ and $z \in [-0.095, 0.095]$ for comparison. Our third example analyzes the effect and usefulness of the tightening step described in Section 5.5.3. In our fourth example, we investigate the heuristic constant 8 in the denominator of (5.21); the domain and constants are from the first example with its finest mesh. Note that our domains are such that $\dot{y} < 0$, which means that the assumptions from Section 5.3 are satisfied, i.e., all trajectories with initial conditions in C leave in both forward and

backward time, and tangencies of the vector field with ∂C occur along a plane where they have quadratic tangency.

In the computations we use the function G defined in (5.15) to prove the monotonicity properties that enables us to efficiently prove transversality. We note that for the example at hand, G is

$$\begin{pmatrix} -\frac{2x}{\epsilon}n_x - n_y + \frac{0.05}{\sqrt{\epsilon}}n_z \\ \frac{1}{\epsilon}n_x - \frac{0.001}{\epsilon}n_z \\ n_y - \frac{0.1}{\sqrt{\epsilon}}n_z \end{pmatrix}.$$

A trivial calculation shows that $G = (0,0,0)$ if and only if $x = -25\sqrt{\epsilon}$ and n is a multiple of $(1, \frac{100}{\sqrt{\epsilon}}, 1000)$, so monotonicity always holds on the right branch of the critical manifold.

5.5.1 Varying ι

The convergence rate of the enclosures at the vertex points should ideally be $O(\epsilon^2)$, since we have corrected for the linear term in the asymptotic expansion of h_ϵ. Our interpolating surfaces between the vertex points are, however, linear. The discretization size thus puts a curvature-dependent restriction on the tightness of the enclosure. In Figure 5.5(a), we illustrate how η for increasing values of ι first decreases, but then reaches a plateau. Looking at η as a function of ϵ, we see that as the mesh size decreases (ι increases), η is approximately proportional to ϵ^2, as expected. This gives a heuristic picture of how η depends on ϵ: for moderately small ϵ, there is a period of quadratic convergence, where the accuracy depends on ϵ; for very small ϵ on the other hand, the accuracy depends primarily on the mesh size. In the intermediate region, the accuracy

depends both on the ratio of time scales and the mesh size. In this region, the exponent decreases from 2 to 0. Figure 5.5(b) illustrates the quadratic convergence region for the finest mesh size from Figure 5.5(a).

As the plateau is reached, $s(\epsilon)$ defined in (5.2) starts to increase. For $\epsilon = 0.1$ the enclosure is too wide for all trajectories inside to be slow in the sense of Definition 5.3.1. In Table 5.1 we give the slopes on the ϵ interval $[10^{-1}, 10^{-4}]$ and bounds on the intervals where $\sqrt{\epsilon}\, s(\epsilon) \leq 1$ on C, for the various ι values from Figure 5.5(a). We are only able to prove that the cone fields are invariant for $\epsilon \leq 10^{-1.94}$, which means that for $\epsilon > 10^{-1.94}$ the normal hyperbolicity is too weak for the algorithm to work. Thus, for the finest mesh size, we prove that the computable slow manifold exists for $10^{-6} \leq \epsilon \leq 10^{-1.94}$. Finer meshes would prove the existence for smaller values of ϵ.

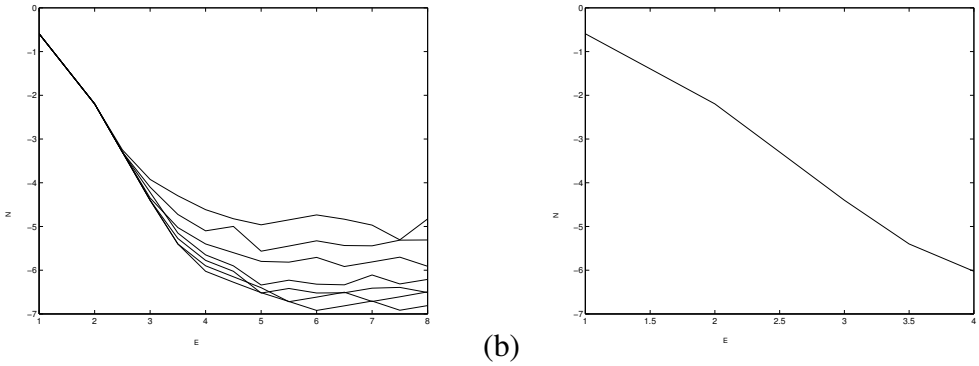

(a) (b)

Figure 5.5: (a) $\log_{10}\eta$ vs $-\log_{10}\epsilon$ for the various values of ι specified in Table 5.1. (b) Zoom in on $-\log_{10}\epsilon \in [1, 4]$ for the value $\iota = 162190$. The least squares approximation of the slope in the steepest part ($-\log_{10}\epsilon \in [2, 3.5]$) is -2.14, on the whole interval $[1, 4]$ it is -1.89.

ι	1200	4662	18236	40805	72239	112736	162190
Slope	-1.40	-1.58	-1.70	-1.76	-1.82	-1.86	-1.89
$\max(-\log_{10}\epsilon)$	4	4.5	5	5	6	6	6

Table 5.1: The second row is the least squares approximations of the slopes of $\log_{10}\eta(-\log_{10}\epsilon)$ on the domain $-\log_{10}\epsilon \in [1,4]$, for some different values of ι. The third row gives the maximum value of $-\log_{10}\epsilon$ where the flow is slow on C, i.e., $s(\epsilon) \leq \frac{1}{\sqrt{\epsilon}}$ on C.

5.5.2 Larger domain

In this subsection we redo the experiment from the previous subsection for a square domain. There are roughly the same number of triangles in the y and z directions, rather than having only a couple of faces in each $\{y = const\}$ slice as we had in Subsection 5.5.1. The resulting η vs ϵ graph is given as Figure 5.6. We see that the results correspond to the coarser meshes in Figure 5.5(a), which is natural, since a larger domain would require a larger number of faces to achieve similar accuracy. This illustrates that the results in Subsection 5.5.1 do not depend on the specific thin slice in the z-direction that we chose to study. For the two discretization sizes in Figure 5.6 we have $\sqrt{\epsilon}\, s(\epsilon) \leq 1$ for $\epsilon \geq 10^{-4}$ and $\epsilon \geq 10^{-5}$, respectively. We are only able to prove that the cone fields are invariant for $\epsilon \leq 10^{-2.09}$, which means that for $\epsilon > 10^{-2.09}$, the normal hyperbolicity is too weak for the algorithm to work. Thus, for the finest mesh size, we prove that the computable slow manifold exists for $10^{-5} \leq \epsilon \leq 10^{-2.09}$.

5.5.3 The effect of the tightening step

The tightening step is the slow part of the algorithm, and our program spends the vast majority of its computing time performing this step. It is therefore interesting to see how

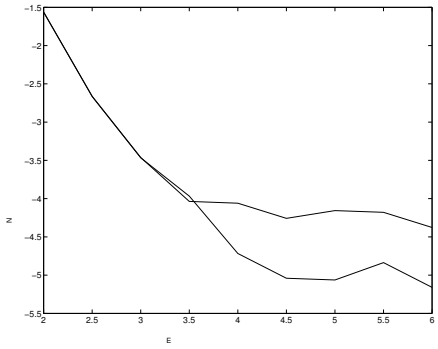

Figure 5.6: $\log_{10}\eta$ vs $-\log_{10}\epsilon$ for $\iota = 21810$ and $\iota = 194396$. The least squares approximations of the slopes on the interval $[2, 4]$ are -1.27 and -1.52, respectively.

the results of a fast version of the algorithm, i.e. without the tightening step, compares performance-wise. We run the example from Section 5.5.1, with the highest precision ($\iota = 162190$), and compare the results. The η vs ϵ graph of the results is given as Figure 5.7. In this example, the program spends 92.7% of the computing time performing the tightening step. The total computing time in this case was 1526 seconds on a 3.2 GHz Dual-Core AMD Opteron. For the example at hand, it might not be worth the extra effort to compute the tightening step for all applications. We do need it, however, for the application in Section 5.6.

5.5.4 Varying the improvement rate

Our method contains a choice of the heuristic constant in the denominator of equation (5.21) that regulates the aggressiveness of the tightening step. In this subsection, we present a study on how the results depend on this choice. We use the same model as above, the domain from Subsection 5.5.1, and the finest mesh size from Subsection 5.5.1 ($\iota = 162190$). For the purpose of this study, we denote the denominator of equation

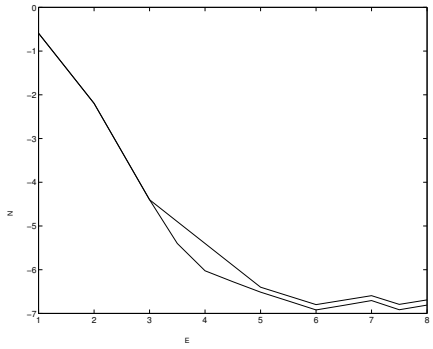

Figure 5.7: $\log_{10}\eta$ vs $-\log_{10}\epsilon$ for $\iota = 162190$, with and without the tightening step of the algorithm.

(5.21), by l. In Figure 5.8 we display the results for $l = 4, 6, 8$. For larger values of l, the results are virtually indistinguishable from the $l = 8$ case. Typically, the updates mostly occur for smaller values of ϵ. The reason is that for sufficiently small values of ϵ the vector field is almost equal to the layer equation, which makes the transversality condition almost trivial. Therefore, less smooth triangulations will still work, and the updates will not violate the transversality conditions.

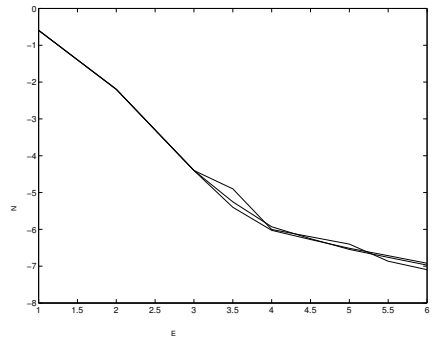

Figure 5.8: $\log_{10}\eta$ vs $-\log_{10}\epsilon$ for $\iota = 162190$, for updates with $\|(v_R - v_L)\|$ divided by 4, 6, and 8.

5.6 Tangencies

In this section we give a proof that the singular Hopf normal form (2.8), used here with $(A, B, C) = (-0.07, 0.001, 0.16)$, undergoes a tangency bifurcation of the unstable manifold of the saddle equilibrium, and the repelling slow manifold. We will in this section often refer to these manifolds as the unstable manifold and the slow manifold. Since we consider μ-families of manifolds in this section, we augment the notation $W^u(E_f)$ and S_r from Chapter 3 by an index μ and denote the unstable manifold of the equilibrium in the fold region and the repelling slow manifold at parameter μ by $W^u(E_f^\mu)$ and S_r^μ respectively. With a slow manifold for the rescaled system, we mean the image of a computable slow manifold for some ϵ under the map (2.7).

Recall that (computable) slow manifolds are not unique. We therefore need to define what we mean by tangency, since if one choice of computable slow manifold is tangential, there will be other choices where the intersection is transversal. The natural setting is therefore to define when a one parameter family of slow manifolds is tangential to another manifold or family of manifolds.

Definition 5.6.1. *A smooth one-parameter family of manifolds, $\{M_\mu\}_{\mu\in[\mu_0,\mu_1]}$, intersects a one-parameter family of families of computable slow manifolds $\{C_\mu\}_{\mu\in[\mu_0,\mu_1]}$ tangentially if for each choice of a smooth one-parameter family of computable slow manifolds $\{S_\mu\}_{\mu\in[\mu_0,\mu_1]}$, $S_\mu \in C_\mu$, there is a value of $\mu \in (\mu_0, \mu_1)$ such that S_μ and M_μ intersect tangentially.*

In our proof, we compute one enclosing region C that satisfies the requirements from Section 5.3 for all values of the parameter μ that appear in the proof. However, the computable slow manifolds might change with the parameter, since they are defined using (5.3). We prove that the one-parameter family of unstable manifolds $W^u(E_f^\mu)$ moves

through this fixed enclosing region, and that, as the family passes through C, it always has to have a tangential intersection with at least one of the computable slow manifolds, regardless of how the smooth one-parameter family of computable slow manifolds inside of C was chosen.

Theorem 5.6.2. *For* $0 < \epsilon \leq 10^{-3}$*, the singular Hopf normal form* (2.6) *undergoes a tangential bifurcation of a computable slow manifold and the unstable manifold of the equilibrium. The bifurcation occurs in the interval* $[\mu_0, \mu_1] = [0.00454, 0.004553]$ *with fixed parameters* $(A, B, C) = (-0.07, 0.001, 0.16)$.

The main argument in the proof of Theorem 5.6.2 is illustrated in Figure 5.9. We consider the intersections of S_r^μ and $W^u(E_f^\mu)$ with a half-plane Σ. At μ_0, the two manifolds do not intersect each other in Σ. Notice that the unstable manifold seems to translate to the left relative to the repelling slow manifold as μ increases. At μ_1, the two manifolds intersect transversally in Σ. In the proof of the theorem, we formalize and prove these observations, and moreover show that the first intersection of the two manifolds is tangential. The vector field is transverse to Σ, so a tangential intersection of the manifolds in Σ corresponds to a tangential intersection in the three-dimensional phase space.

In the proof of Theorem 5.6.2, we will at times work with the singular Hopf normal form (2.6), and at other times with the rescaled singular Hopf normal form (2.8). Recall that in the rescaled system, we use upper case variables and parameters (μ is scale-independent). Note that we do not assert that the tangency of the manifolds is unique. We will first prove Theorem 5.6.2 for $\epsilon = 10^{-3}$. For smaller ϵ, the result follows from the rescaling (2.7) and the following property of the relative slope condition for the singular Hopf normal form:

$$\frac{s(\epsilon')}{\sqrt{\epsilon'}} = \frac{s(\epsilon)}{\sqrt{\epsilon}}.$$

Hence, if

$$s(\epsilon) \leq \frac{1}{\sqrt{\epsilon}},$$

then

$$s(\epsilon') = \sqrt{\frac{\epsilon'}{\epsilon}} s(\epsilon) < s(\epsilon) \leq \frac{1}{\sqrt{\epsilon}} < \frac{1}{\sqrt{\epsilon'}}.$$

The existence of computable slow manifold at a particular value of ϵ thus implies the existence of computable slow manifolds at all smaller values of ϵ. Note that these computable slow manifolds will appear at different positions in the phase space for different values of ϵ.

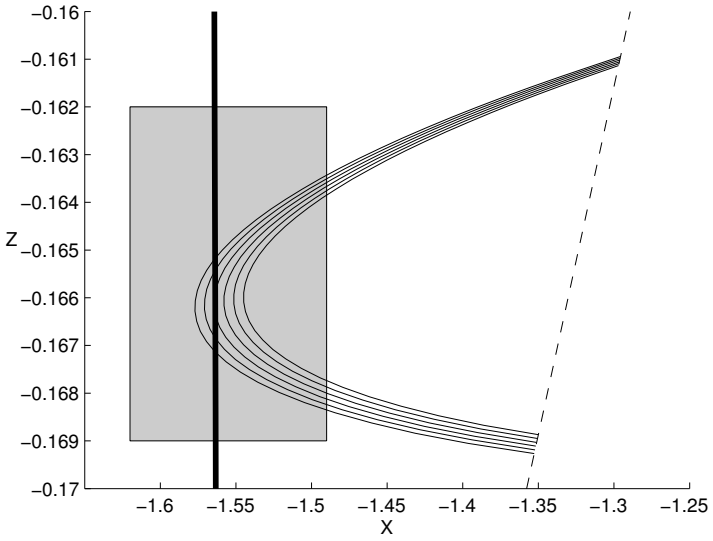

Figure 5.9: An example family S_r^μ (thick line) and images of fundamental domains (solid curves) of $W^u(E_f^\mu)$ for a selection of μ in $[\mu_0, \mu_1]$, shown here intersected with Σ. The boundary of Σ is drawn as a dashed line, the rectangle R is drawn as a shaded region. As μ is varied in $[\mu_0, \mu_1]$, the slow manifold only moves by amounts too small to be noticeable at the scale of the diagrams. For each $W^u(E_f^\mu)$ included in the figure, we plot the first intersection of the trajectories with Σ, if the trajectory reaches Σ.

Set-up. We will work with

$$\Sigma := \{(X, Y, Z) \in \mathbb{R}^3 : Z \geq -0.1693 + 0.16\,(X + 1.353),\, Y = 2\}$$

and

$$R := \{(X, Y, Z) \in \Sigma : -1.62 \leq X \leq -1.49, -0.169 \leq Z \leq -0.162\}.$$

We next list verifiable conditions that via Lemma 5.6.4 below will prove Theorem 5.6.2. Many of these conditions are illustrated in Figure 5.10. Let

$$Y_{min}, Y_{max} : [\mu_0, \mu_1] \to \mathbb{R}$$

be continuous with $Y_{min}(\mu) \leq Y_{max}(\mu)$. Further define a two-dimensional "box" by

$$B_0 := \{(\mu, X, Y, Z) \in [\mu_0, \mu_1] \times W^u(E_f^\mu) :\ X = \pi_X(p_\mu), Y_{min}(\mu) \leq Y \leq Y_{max}(\mu)\}.$$

Note that the requirement $(X, Y, Z) \in W^u(E_f^\mu)$ uniquely defines Z as a function of (μ, X, Y). Denote the corners of B_0 corresponding to

$$(\mu, Y) \in \{(\mu_1, Y_{max}(\mu_1)), (\mu_0, Y_{max}(\mu_0)), (\mu_0, Y_{min}(\mu_0)), (\mu_1, Y_{min}(\mu_1))\}$$

by $\{M_1, M_2, M_3, M_4\}$. Denote the flow map of system (2.8) from B_0 to Σ, wherever it is defined, by Ψ. The next step of our construction is to introduce a number of assumptions, that are verifiable using validated numerics, i.e., they can be restated as a finite number of computable conditions. The geometry of these assumptions is illustrated in Figure 5.10. In Lemma 5.6.4 below we show that these assumptions are sufficient to prove Theorem 5.6.2.

Assumption 5.6.3. *Assume that the following conditions are satisfied:*

(I) For $\mu \in [\mu_0, \mu_1]$, a family of repelling slow manifolds S_r^μ intersects R in a single family of curves C_μ that enters R at the top and exits R at the bottom.

(II) The map Ψ is defined on the three sides of B_0 corresponding to $Y = Y_{min}(\mu), Y = Y_{max}(\mu)$ and $\mu = \mu_0$, and their images under Ψ lie in R and strictly to the right of $S^{\mu}_{r} \cap R$.

(III) The map Ψ is defined on $\{(\mu, X, Y, Z) \in B_0 : \mu = \mu_1\}$ and its image lies in R. Furthermore, $\Psi(M_1)$ and $\Psi(M_4)$ are strictly to the right of $S^{\mu}_{r} \cap R$, and there exists a point $M_5 \in \{(\mu, X, Y, Z) \in B_0 : \mu = \mu_1\}$ such that $\Psi(M_5)$ lies strictly to the left of $S^{\mu}_{r} \cap R$ in Σ.

(IV) The map Ψ is well-defined on B_0.

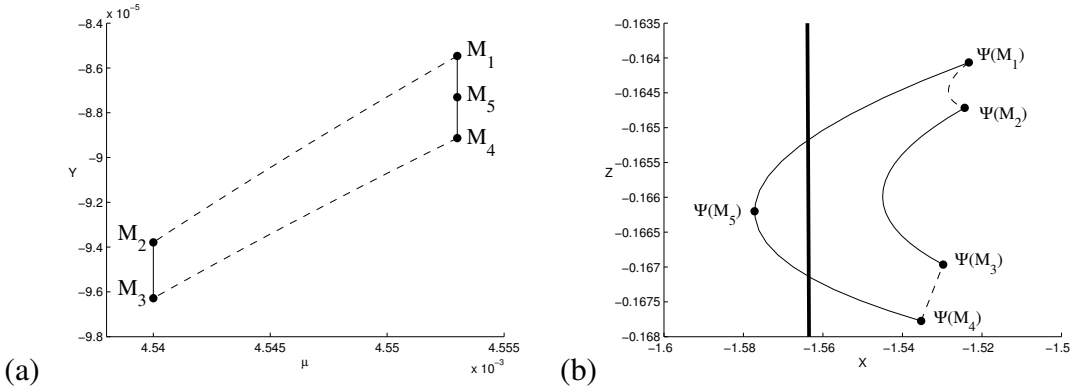

Figure 5.10: Illustration of the assumptions made in Assumption 5.6.3. The box B_0 shown in pane (a) maps into $R \subset \Sigma$ as shown in pane (b). As μ is varied in $[\mu_0, \mu_1]$, the slow manifold (thick solid line) only moves by amounts too small to be noticeable at the scale of the diagrams.

Lemma 5.6.4. *Suppose that Assumptions 5.6.3 are satisfied. Then S^{r}_{μ} and $W^u(E^{\mu}_{f})$ intersect tangentially for some $\mu^* \in [\mu_0, \mu_1]$.*

Proof of Lemma 5.6.4. Fix a family of slow repelling manifolds S^{r}_{μ}, $\mu \in [\mu_0, \mu_1]$. Since all of B_0 reaches Σ by Assumption 5.6.3.IV, the existence and uniqueness theorem for ODEs implies that the map from B_0 to $\Sigma \times [\mu_0, \mu_1]$ is continuous. We may thus define

the continuous function

$$\text{dist}(\mu, Z) := \min\left(\pi_X(W^u(E_f^\mu)|_Z \cap R) - \pi_X(S_\mu^r|_Z \cap R)\right)$$

where Z is required to lie in the range of Z values of R and $|_Z$ denotes restriction to Z. Consider

$$\mu^* = \min\{\mu \in [\mu_0, \mu_1] : \min_Z \text{dist}(\mu, Z) = 0\},$$

the existence of which follows from Assumptions 5.6.3.II and 5.6.3.III, and the continuity of $\text{dist}(\mu, Z)$. Clearly $S_{\mu^*}^r \cap R$ and $W_{\mu^*}^u \cap R$ intersect in at least one point (X_0, Y_0, Z_0). Moreover,

$$\pi_X(W_{\mu^*}^u|_Z \cap R) - \pi_X(S_{\mu^*}|_Z \cap R) \geq 0$$

for the range of Z values that lie in R. Since $W_{\mu^*}^u$ and S_{μ^*} are smooth surfaces in $\mathbb{R}^3$, transverse to R, we can now consider the Taylor series expansion of

$$\pi_X(W_{\mu^*}^u|_Z \cap R) - \pi_X(S_{\mu^*}|_Z \cap R)$$

at X_0 with respect to X and conclude that its linear term must be zero. We have thus shown that the manifolds $W_{\mu^*}^u$ and S_{μ^*} intersect tangentially in R. □

Subsection 5.6.1 below gives details on the verification of Assumption 5.6.3.I. Subsection 5.6.2 describes in detail how Σ, Y_{min}, and Y_{max} are chosen, and provides details on the verification of Assumptions 5.6.3.II, 5.6.3.III, and 5.6.3.IV.

5.6.1 Slow manifold computations

Showing that for $\mu \in [\mu_0, \mu_1]$, a family of repelling slow manifolds S_r^μ intersects R in a single family of curves is a straight-forward application of the methods developed in

the earlier parts of this chapter: we compute slow manifold enclosures for the rescaled singular Hopf system (2.8) over a domain that corresponds to

$$1 \leq Y \leq 500, \quad -0.169 \leq Z \leq -0.162,$$

and for the singular Hopf parameter values

$$\{(\mu, A, B, C) \in \mathbb{R}^4 : \mu \in [4.54, 4.553] \times 10^{-3}, A = -0.07, B = 0.001, C = 0.16\}.$$

The actual computations for the enclosures are performed in the original singular Hopf coordinates of (2.6), as described in earlier sections of this chapter. Let $\epsilon_0 = 10^{-3}$. In the original coordinates of the singular Hopf normal form (2.6), the domain now corresponds to

$$D = [y_{min}, y_{max}] \times [z_{min}, z_{max}],$$

where $y_{min} = 1.0\,\epsilon_0, y_{max} = 500.0\,\epsilon_0, z_{min} = -0.169\,\sqrt{\epsilon_0}, z_{max} = -0.162\,\sqrt{\epsilon_0}$, and the set of singular Hopf system parameters is

$$\left\{(\epsilon, \mu, a, b, c) \in \mathbb{R}^5 : \epsilon = \epsilon_0, \mu \in [4.54, 4.553] \times 10^{-3}, a = -\frac{0.07}{\sqrt{\epsilon_0}}, b = \frac{0.001}{\epsilon_0}, c = \frac{0.16}{\sqrt{\epsilon_0}}\right\}.$$

The enclosures obtained show that points (X, Y, Z) in the repelling slow manifold over D must satisfy

$$-1.5726 < X < -1.5539.$$

Moreover, the methods of Section 5.3 of this chapter were used to check that at any parameter in the above-described set, S_r^μ is a graph over a domain $D \subset S_0$, and that $s(\epsilon_0) \leq 1.027$. Again, note that the computation is independent of the choice of ϵ_0, since a different choice of ϵ_0 would imply that we should enclose a different part of the phase space. Since the above z_{min} and z_{max} were chosen large and small enough, respectively, to conclude that the enclosed repelling slow manifolds enter R at the top and leave R at the bottom, we have shown the existence of the sought family of slow manifolds.

Remark. Even though the slow manifold intersected with the section Σ in our case resembles a fixed straight line, enclosing it with the precision required for the proof to work is a hard problem. To determine rigorously the location of a slow manifold is difficult even in the easiest non-trivial cases. The problem is amplified in our case since we need high accuracy in the rescaled system, where the errors are blown up by a factor $O\left(\frac{1}{\sqrt{\epsilon}}\right)$.

5.6.2 Unstable manifold computations

We now describe how Y_{min} and Y_{max} are chosen for Assumptions 5.6.3.II and 5.6.3.III to be satisfied. Recall that Figure 5.9 was obtained by examining trajectories in entire fundamental domains of $W^u(E_f^\mu)$ for $\mu \in [\mu_0, \mu_1]$, and that some of these trajectories did not reach Σ. We chose Y_{min} first and then Y_{max} in such a way that B_0 is on the one hand small enough for the map to Σ to be well-defined and its image to be in R, and on the other hand large enough for the images of marked points $M_1, \ldots, M_5$ and of the boundaries of B_0 to map to the left or right of S_r^μ as required by Assumptions 5.6.3.II and 5.6.3.III.

Computing $Y_{min}(\mu)$

Let $L \subset \Sigma$ be the line given by

$$L := \{(X, Y, Z) = (t, 3, -0.1678 + 0.16\,(t + 1.535)) \ : t \in \mathbb{R}\}.$$

This line lies well within Σ and is parallel to $\partial\Sigma$. It is moreover transverse to the parts $W^u(E_f^\mu)$ that reach Σ, for all $\mu \in [\mu_0, \mu_1]$. The boundary value problem (BVP) for the flow of the rescaled singular Hopf normal form with the following boundary conditions and μ as the continuation parameter is thus well-defined:

- trajectories have to start in the unstable eigenspace of p_μ,
- trajectories have to start at an X coordinate equal to that of p_μ,
- trajectories have to end on L.

Note that there are multiple solutions to this BVP, as each trajectory in the unstable manifold satisfies the initial boundary condition multiple times as it spirals away from the equilibrium point p_μ, but we choose one by selecting a fundamental domain for its endpoint near p_μ. The equilibrium points $p_\mu = (x_\mu, x_\mu^2, x_\mu)$ satisfy the equation $x_\mu = -45 + \sqrt{45^2 - 1000\mu}$. We use a trajectory that initially has a Y coordinate approximately 10^{-4} larger than that of p_μ, deferring a discussion of the suitability of this distance to a remark at the end of this subsection. Solving the BVP with a shooting method, we find that the Y coordinates of the solutions to the boundary value problem are close to linear in μ on the interval $[\mu_0, \mu_1]$. We thus define

$$Y_{min}(\mu) = x_\mu^2 - 9.37888799540 \times 10^{-5} + 0.640307054861539\,(\mu - \mu_0),$$

to be the linear function in μ that approximates the Y coordinates of the solution endpoints to the BVP.

Computing $Y_{max}(\mu)$

After inspecting diagrams similar to Figure 5.10, we defined $Y_{max}(\mu)$ in an ad-hoc manner to be the linear function for which the box B_0 contains 25% of a fundamental domain of $W^u_{\mu_0}$ and 40% of a fundamental domain of $W^u_{\mu_1}$:

$$Y_{max}(\mu) = x_\mu^2 - 9.628167607168 \times 10^{-5} + 0.549805711513847\,(\mu - \mu_0).$$

Computing unstable manifolds

The complexity of the singular Hopf normal form makes it unfeasible to compute unstable manifolds analytically. We therefore begin by describing a method to rigorously compute the location of $W^u(E_f^\mu)$. We will use the method developed in Section 5.4 together with covering relations with cone conditions [70] to enclose and propagate the manifolds, and validated numerical integration [46, 50, 51, 52] to propagate the manifolds. In our implementation [80] we use the software VNODE-LP [78] to integrate the system (2.8). The computations are done using order 11 Taylor expansions in VNODE-LP.

We construct an h-set with cones centered at p_μ as a cylinder of size 10^{-4} and 10^{-5} in the (X, Y) and Z directions, respectively, with a cone with Lipschitz constant 0.1 defined by the quadratic form

$$Q = \begin{bmatrix} 1 & 0 & 0 \\ 0 & 1 & 0 \\ 0 & 0 & -100 \end{bmatrix}.$$

We verify that covering relations and cone conditions hold for the time 6.3 map. This proves that the unstable manifold exists within the h-set, and yields an enclosure of the unstable manifold as a Lipschitz graph with Lipschitz constant 0.1 over the disc:

$$\left\{(X, Y) \ : \|(X - x_\mu, Y - x_\mu^2)\| \leq 10^{-4}\right\}.$$

To further contract the enclosure for a given value of (X, Y), we partition the line segment over (X, Y) in the cone, and integrate backwards for 100 time units or until the trajectory leaves the cone. Subsegments that leave the cone in backwards time are removed, and we use the interval hull of the remaining subsegments as our new bound of a point in the unstable manifold. The covering relations with cone conditions prove that each remaining subsegment over (X, Y) contains a unique Z value such that $(X, Y, Z) \in W^u(E_f^\mu)$.

Given an initial enclosure of a point in W^u_μ, we propagate it forwards by integrating (2.8) using VNODE-LP until it hits Σ. To integrate the top and bottom of B_0, i.e., the boundaries of B_0 where μ is not constant, and the interior of B_0, we consider a four-dimensional phase space by appending $\dot{\mu} = 0$ to (2.8). This procedure stabilizes the numerical behavior of the propagation of the unstable manifold.

Verifying Assumptions 5.6.3.(II-IV)

Using the method described in Section 5.6.2, one can now subdivide ∂B_0 into small subsets, compute an interval enclosure of each subset, and use validated numerical integration to show that Assumptions 5.6.3.II, 5.6.3.III and 5.6.3.IV are satisfied. In practice, this requires some experimentation: if the subsets are too large, wrapping effects in the numerical integration will make the verification of Assumptions 5.6.3.II, 5.6.3.III and 5.6.3.IV impossible. On the other hand, the computing time for the entire verification of Assumption 5.6.3.II is approximately proportional to the number of subsets to be integrated numerically. The bounds on $\Psi(\partial B_0)$ and $\Psi(M_i)$, for $i = 1, 4$, and 5, are given in Table 5.2.

(a)

	$\Psi(\partial B_0(\mu_0))$	$\Psi(\partial B_0(\mu_1))$	$\Psi(\partial B_0(Y_{min}))$	$\Psi(\partial B_0(Y_{max}))$
X	-1.5^{468}_{227}	$-1.^{6102}_{5156}$	-1.5^{462}_{236}	-1.5^{368}_{107}
Z	-0.16^{71}_{46}	-0.16^{83}_{35}	-0.16^{84}_{64}	-0.16^{57}_{29}

(b)

	$\psi(M_1)$	$\psi(M_4)$	$\psi(M_5)$
X	-1.52^{37}_{29}	-1.535^{5}_{1}	-1.57^{86}_{58}
Z	-0.164^{1}_{0}	-0.167^{8}_{7}	-0.166^{3}_{1}

Table 5.2: (a) The image of ∂B_0 under Ψ. (b) The image of the marked points on the $\partial B_0(\mu_1)$ line under Ψ. All images are in the interior of R. The computations for (a) and (b) prove Assumptions 5.6.3.II and 5.6.3.III, respectively.

Remark. Note that since the position of S_r^μ as well as the map to Σ are computed using interval arithmetic, their computed positions have errors due to over-estimation associated with them. These errors have to be taken into account when choosing the Y value at which to place the half-plane Σ, the interval boundaries μ_0 and μ_1, and the functions Y_{min} and Y_{max}. Generally, placing Σ at greater values of Y results in tighter bounds for the slow manifold, and the repelling nature of the slow manifold spreads trajectories that were initially close in the fundamental domain far apart, making it easier to verify Assumptions 5.6.3.(II-IV). We found the size 2×10^{-4} of the h-sets constructed in Section 5.6.2 to be large enough to keep the validated numerical integration to Σ short enough to not accumulate prohibitively large errors, while being small enough to be efficiently computable.

Remark. To give further insight into what happens after the bifurcation we note that the following set is forward invariant. For other values of the parameters, similar sets can be constructed. For $k > B$,

$$X < \frac{-\mu}{A + C}, \quad X^2 > (1 + k)Y, \quad Y > \frac{1 + k}{k}, \quad |X| > |Z|.$$

We verify that the above conditions are satisfied, with $k = 2$, for the point M_5. Thus, $X \to -\infty$ and $Y \to \infty$ for a part of the unstable manifold past the tangential bifurcation.

5.7 Discussion

Some of our ideas generalize to the case of slow manifolds of saddle type. To compute normally hyperbolic manifolds of saddle type, see e.g. [8], one usually first computes the manifold's stable and unstable manifolds, and then intersects them. To compute a saddle slow manifold in a three-dimensional ambient space using our ideas, one could

compute enclosures of the stable and unstable manifolds, as presented in this dissertation. The existence argument given in Section 5.3 can be modified to this setting, under appropriate assumptions on the dynamics on the slow manifold. Generalization to slow manifolds of saddle type in higher-dimensional ambient spaces is substantially more challenging.

We made several design decisions when constructing our algorithm for computing slow manifolds. This section discusses details of some of them and motivates our choices.

- Our enclosures were constructed as pairs of enclosing transversal piecewise linear surfaces. There are several alternative approaches to how to construct and refine the vertices of the enclosing triangulated surfaces $\mathcal{L}$ and $\mathcal{R}$. For the examples in Sections 5.5 and 5.6 we used rectangular patches in the domain of the slow variables. Instead, one could construct the triangulations of the original domain in the slow variables by considering a dynamically defined region, constructed by flowing a set of initial conditions on the critical manifold with the slow flow, and use a discretization of those trajectories as the vertices of the triangulation.
- We considered other possibilities for moving vertices in Section 5.4.4; namely, to move them along trajectories of the flow of (5.1), or to move them along the normal of the triangulation. Both of these methods have serious disadvantages. When moving vertices along the flow of the system, we have to carefully check whether the vertices are moved past edges, thereby destroying the integrity of the triangulation. If the triangulation remains a graph over the (y, z) domain, it is possible to generate a new triangulation by a Delaunay-type algorithm, and lift it to the surface, but if two vertices flow to the same (y, z) coordinate this is no longer possible. Additionally, this method of moving vertices moves the two enclosing

surfaces by different amounts, so that we obtain an enclosure of a smaller part of the slow manifold. A third drawback is that the triangulations might develop very acute triangles. Finally, numerical integration of a large number of vertices is slow compared to the approach that we use. Moving vertices along the normals combines the worst of both methods: we no longer control the triangulations, and we might introduce violations of the transversality conditions.

- The tightening procedure described in Section 5.4.4 only updates one vertex at the time, i.e., we move one vertex a big step and if all the faces attached to it are still transversal to the flow, then we move it. An alternative would be to move not only the vertex itself, but at the same time all vertices attached to it by an edge. Such a procedure would work as follows: when it is one vertex' "turn", only update it by a fraction of its potential improvement, and simultaneously move the ones it attaches to, by a smaller amount. The smaller neighbor updates should be such that the expected value of the total update of each vertex stays the same as in Section 5.4.4. The benefit of such an approach is that the triangulation is not skewed as much in each step, so it should be easier to verify the transversality condition. In practice, however, the gain of this approach is negligible, compared to a slight increase of the denominator of (5.21). There are also disadvantages of such an approach, primarily in its computational complexity. Each time an update is made, one has to not only locate all its neighboring vertices and update them, but also locate all of their neighboring faces and check the transversality condition on them. In the results presented in Section 5.5, we thus only update one vertex at the time.

- We construct invariant cone fields on C to prove that it contains normally hyperbolic locally invariant manifolds. We constructed these manifolds by flowing a "ribbon" around the inflowing boundaries of the enclosure. The property that our

enclosures were aligned with the flow, in the sense that for one of the slow variables the vector field is non-zero, was crucial for proving the existence of computable slow manifolds. In general one could also use the invariant cone fields to show that the graph transform is well defined, by adapting the method in [35]. To prove the convergence of such a scheme would require very careful estimates of the expansion and contraction rates, and the norms of the nonlinear components of the vector field. An alternative is to define an extension of the vector field outside of C that has a slow manifold that is invariant rather than just locally invariant. Global invariance together with normal hyperbolicity would give a unique manifold for the extension using the technique from [8]. Given normal hyperbolicity, ensured by the existence of the cone field, either method would give the existence of a (non-unique) C^1 normally hyperbolic manifold which is the graph over the slow variables. Either of these approaches, however, includes many subtle details that need to be clarified for the case at hand.

- If the mesh size of piecewise linear enclosing surfaces remains fixed as ϵ decreases, then the curvature of the slow manifold becomes a a limiting factor in the tightness of enclosures. With smoother enclosing manifolds, tighter enclosures are likely possible. We did not attempt this because the transversality calculations for piecewise linear systems were particularly simple in the singular Hopf normal form we studied.

APPENDIX A

BIFURCATION LABELS

Bifurcation label	Bifurcation / explanation	Codim.
H_{sup}	supercritical Hopf bifurcation	1
H_{sub}	subcritical Hopf bifurcation	1
SN	saddle-node bifurcation	1
PD	period-doubling bifurcation	1
NS	torus bifurcation / Neimark-Sacker bifurcation	1
LPC	fold of periodic orbits bifurcation / limit point of cycles bifurcation	1
H	homoclinic bifurcation	1
T	tangency of invariant manifolds bifurcation	1
S	approximate symmetry of the slow flow	1
ZH	zero Hopf bifurcation / fold Hopf bifurcation	2
GH	generalized Hopf bifurcation / Gavrilov-Guckenheimer bifurcation	2
P	see sections 4 and 5	2
R1	1:1 resonance on a torus bifurcation curve	2
R2	1:2 resonance on a torus bifurcation curve	2
R3	1:3 resonance on a torus bifurcation curve	2
R4	1:4 resonance on a torus bifurcation curve	2
E	fold of generalized Hopf bifurcations	3
F	endpoint of the tangency curve crosses the torus bifurcation curve	3
G	tangency curve coalesces with Hopf bifurcation curve	3
H	torus bifurcation curve intersect Hopf bifurcation curve tangentially	3
I	period-doubling bif. curve intersects Hopf bif. curve tangentially	3
J	fold of the curves where the slow-flow has singular cycles	3

Table A.1: Table showing the abbreviations for bifurcations used in this paper, together with the full name or description of the bifurcation, as well as their codimension. Different names for the same bifurcation are separated by slashes.

APPENDIX B

TWO-DIMENSIONAL BIFURCATION DIAGRAMS FOR THE SCALED SINGULAR HOPF NORMAL FORM

This appendix is a catalog of (μ, A) bifurcation diagrams for system (2.8), including at least one sample diagram for each of the (B, C) regions Ia to VIIIa described in Section 3.3.

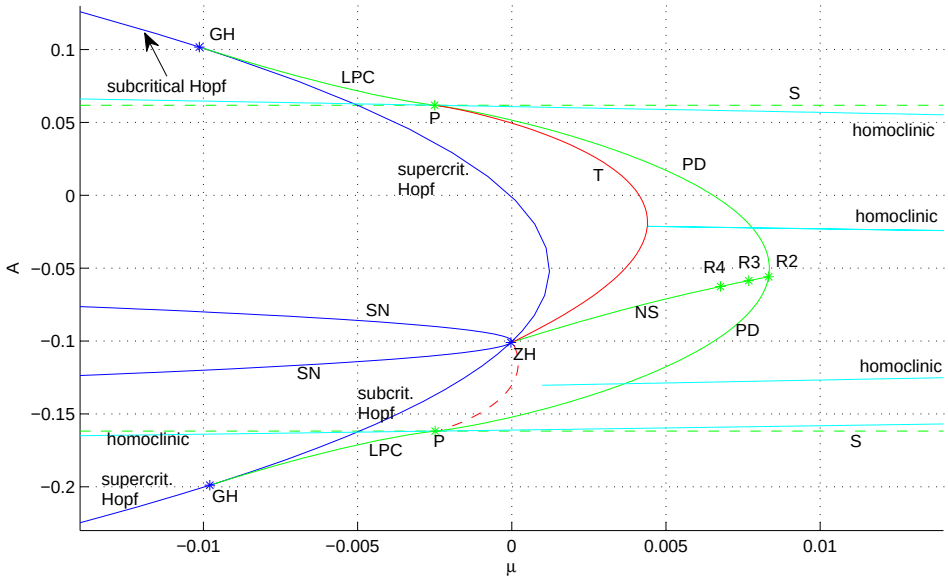

Figure B.1: Region Ia: (μ, A) bifurcation diagram for $(B, C) = (-0.01, 0.1)$. This diagram shows homoclinic bifurcations as cyan curves. The top and bottom homoclinic curves have equilibria close the origin, while the middle two have equilibria distant from the origin. The first and the third homoclinic curves connect for $O(\epsilon^{1/2})$ values of μ, as do the second and fourth homoclinic curves. We conjecture that the endpoint of the top curve is close to where the periodic orbit born in the singular Hopf bifurcation ceases to be the only ω limit set for trajectories in the two-dimensional unstable manifold of the singular Hopf equilibrium, and that the endpoint of the bottom curve is close to where the periodic orbit born in the singular Hopf bifurcation ceases to be the only α limit set for trajectories in the two-dimensional stable manifold of the singular Hopf equilibrium. The location of a tangential intersection of S_a with $W^s(E_f)$ is drawn with a dashed red line.

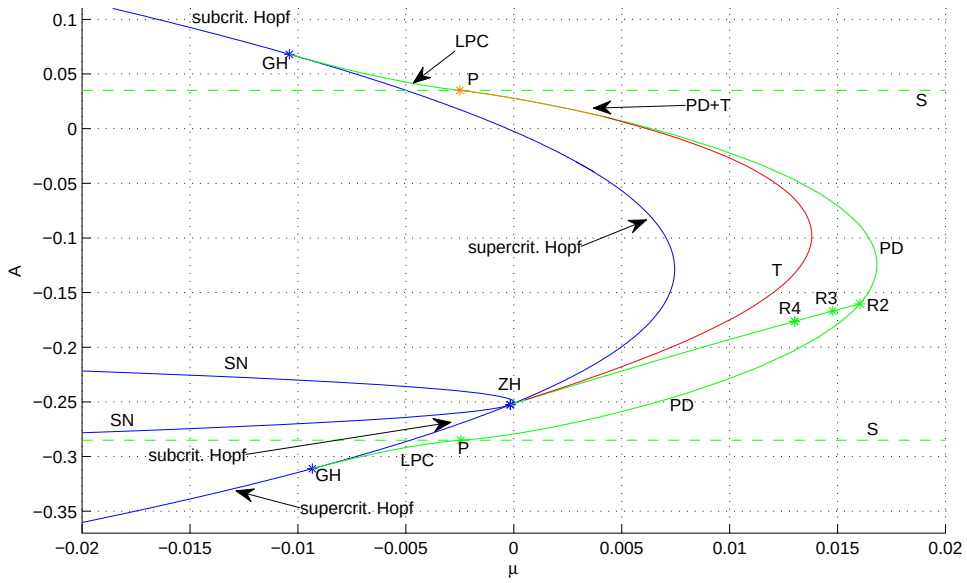

Figure B.2: Region Ia: (μ, A) bifurcation diagram for $(B, C) = (-0.01, 0.25)$. Observe that the tangency curve in some regions nearly coincides with the period-doubling and the torus bifurcation curves. This is not the case for all (B, C) in region Ia. For $B < 0$ with large absolute value or C less positive than in this figure, the torus bifurcation curve coincides with the tangency curve on shorter segments, or not at all. For $B < 0$ with small absolute value, the tangency curve tends to separate from the period-doubling curve closer to the point labeled P.

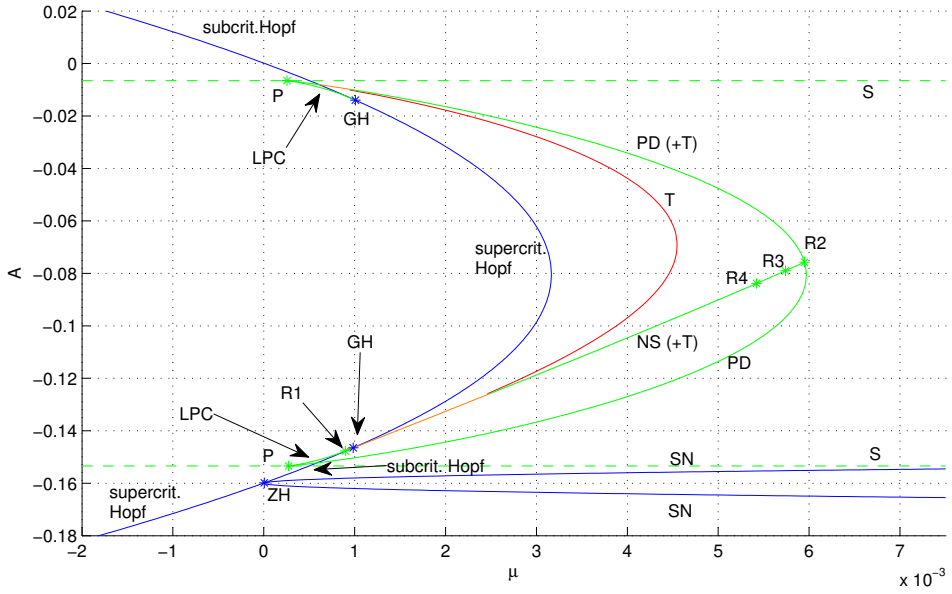

Figure B.3: Region IIa: (μ, A) bifurcation diagram for $(B, C) = (0.001, 0.16)$. Note that the tangency curve partly coincides with the period-doubling curve, cf. Figure 3.9. This is typically observed for very large values of C, cf. Figure C.1.

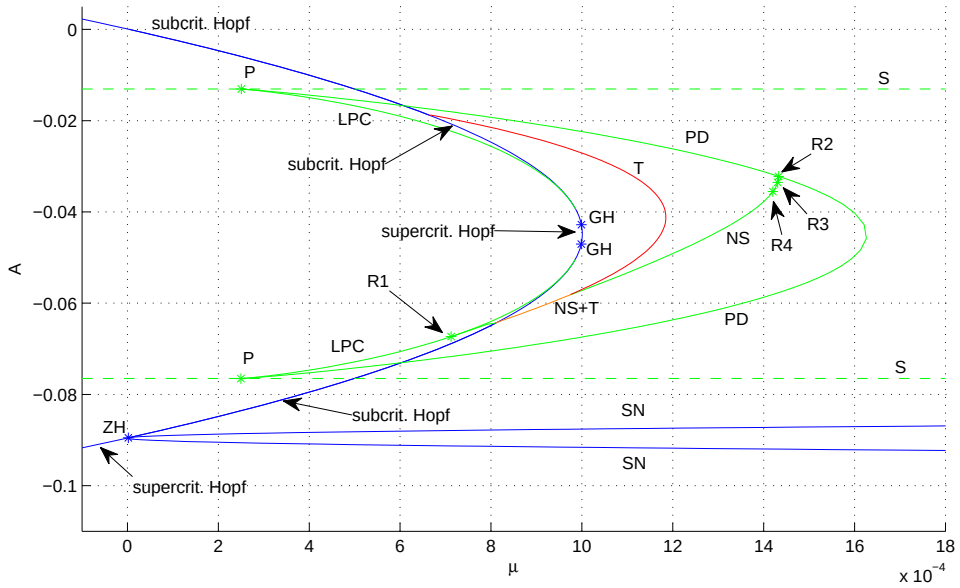

Figure B.4: Region IIa: (μ, A) bifurcation diagram for $(B, C) = (0.001, 0.0896)$. The generalized Hopf bifurcations are close together, and vanish at $(B, C) = (0.001, 0.0894)$.

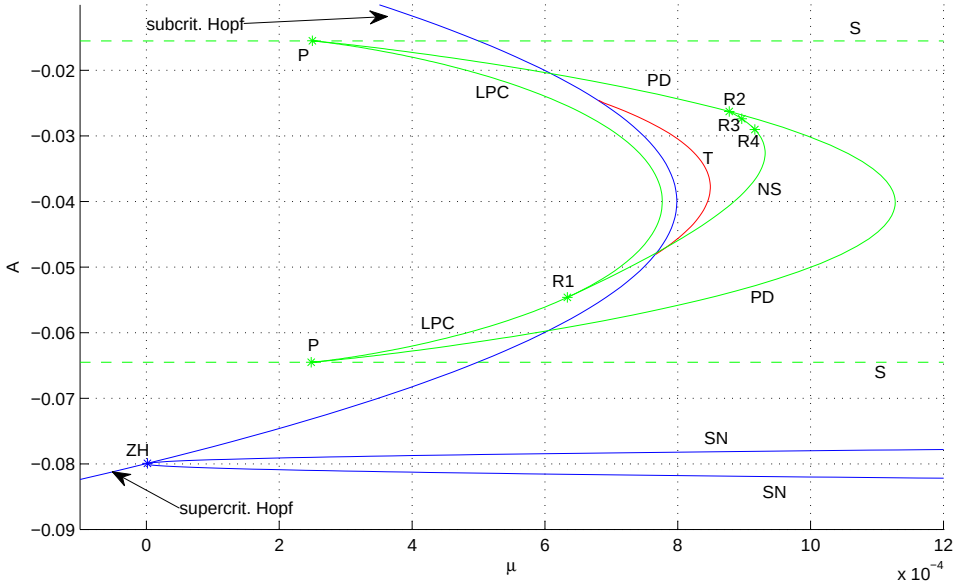

Figure B.5: Region IIIa: (μ, A) bifurcation diagram for $(B, C) = (0.001, 0.08)$.

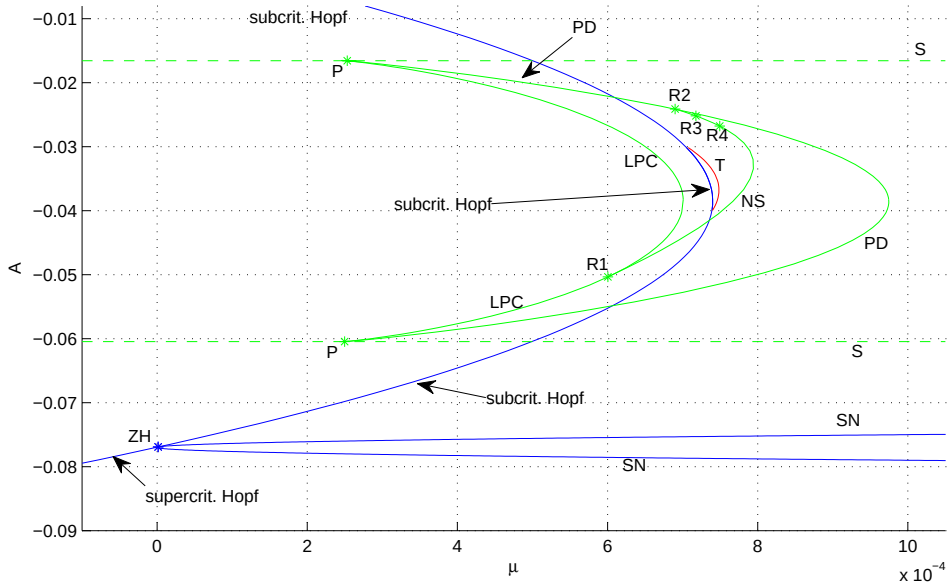

Figure B.6: Region IVa: (μ, A) bifurcation diagram for $(B, C) = (0.001, 0.077)$. The tangency curve and the torus bifurcation curve do not meet in this diagram.

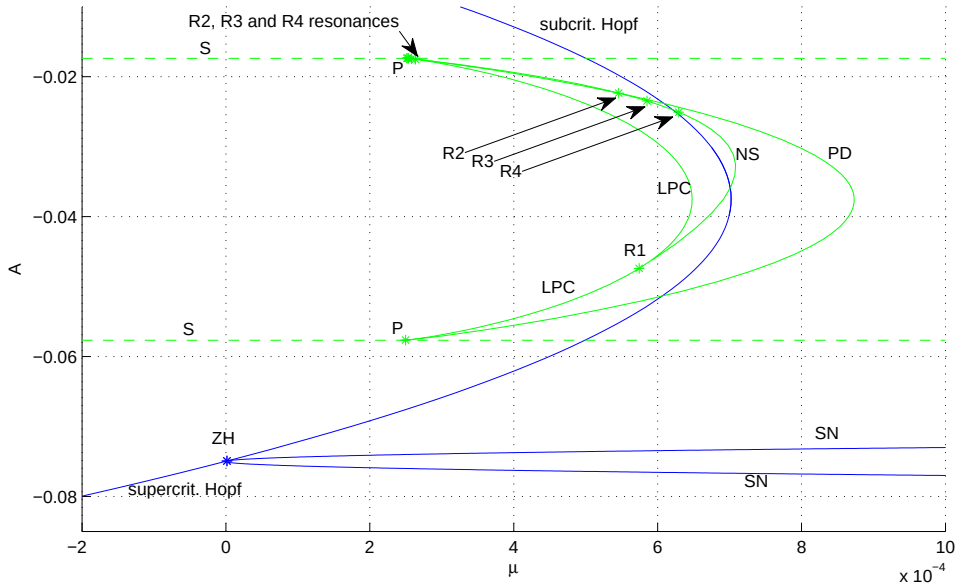

Figure B.7: Region Va: (μ, A) bifurcation diagram for $(B, C) = (0.001, 0.075)$.

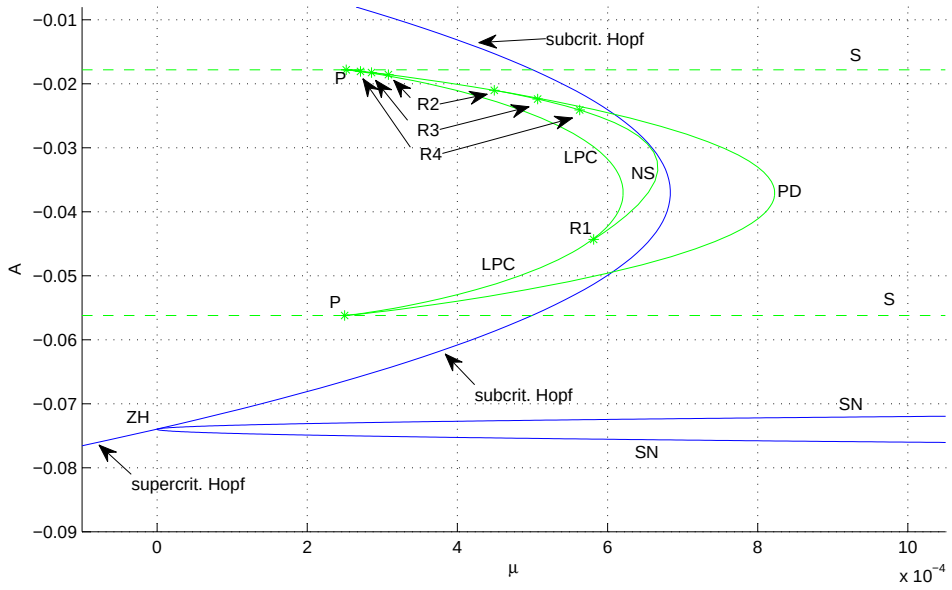

Figure B.8: Region Va / VIa: (μ, A) bifurcation diagram for $(B, C) = (0.001, 0.074)$. Relative to Figure B.6, the resonances have crossed the Hopf curve, and a second torus bifurcation curve with R2, R3 and R4 resonances appeared.

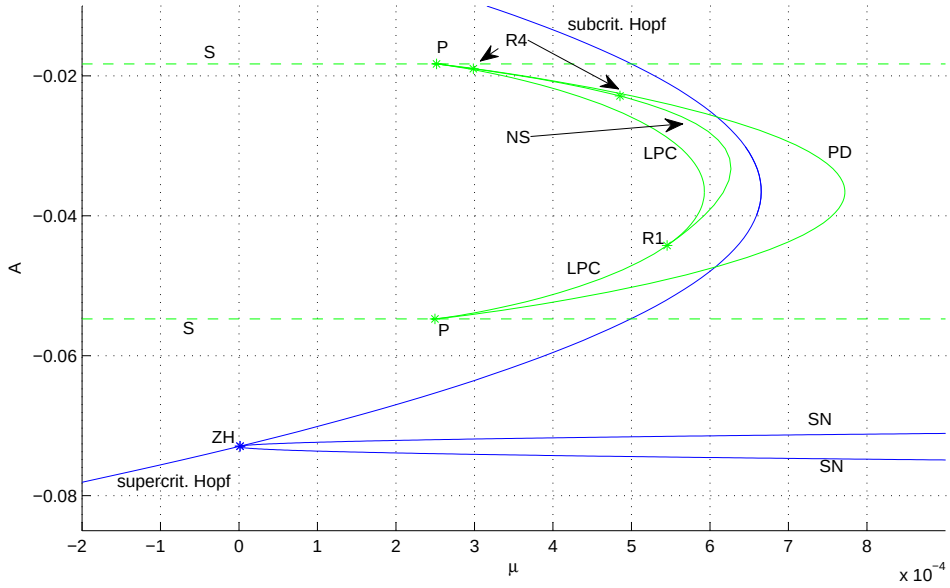

Figure B.9: Region VIa: (μ, A) bifurcation diagram for $(B, C) = (0.001, 0.073)$. Although the torus bifurcation curve and period-doubling curve are at times very close, we did not detect intersections of the two curves.

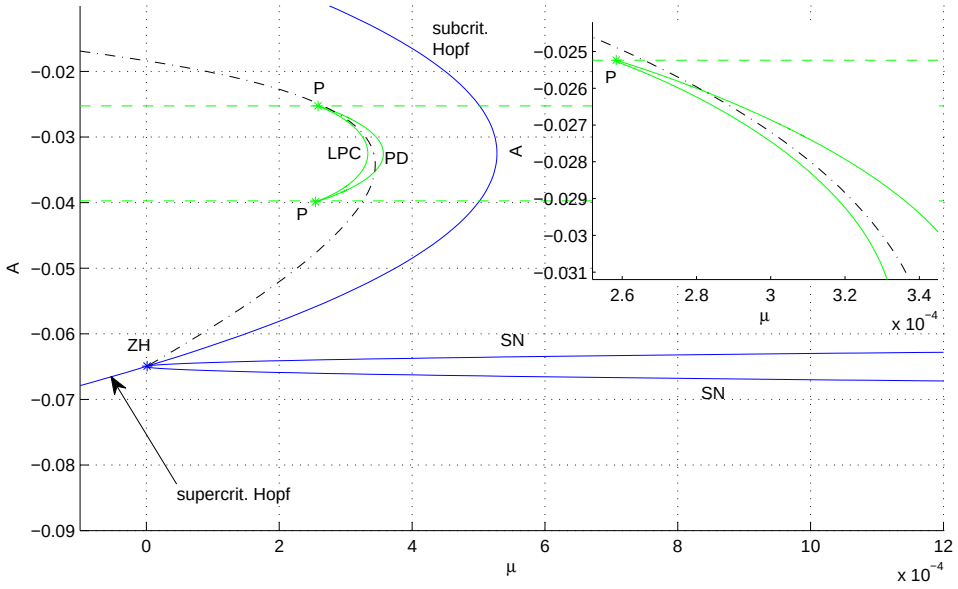

Figure B.10: Region VIIa: (μ, A) bifurcation diagram for $(B, C) = (0.001, 0.065)$. In this diagram, the curve $L_{(B,C)}$, explained in Section 3.3 and not included in other (μ, A) bifurcation diagrams, is plotted with a dashed black line. The inset shows that the curve lies on the branch of the periodic orbit that has real multipliers. Note that while the singular Hopf periodic orbit does not undergo any torus bifurcations for these values of B and C, there may be other (μ, A) bifurcation diagrams in region IVa with torus bifurcations and the same kinds of codimension-two bifurcations of periodic orbits that occur in region IIIa.

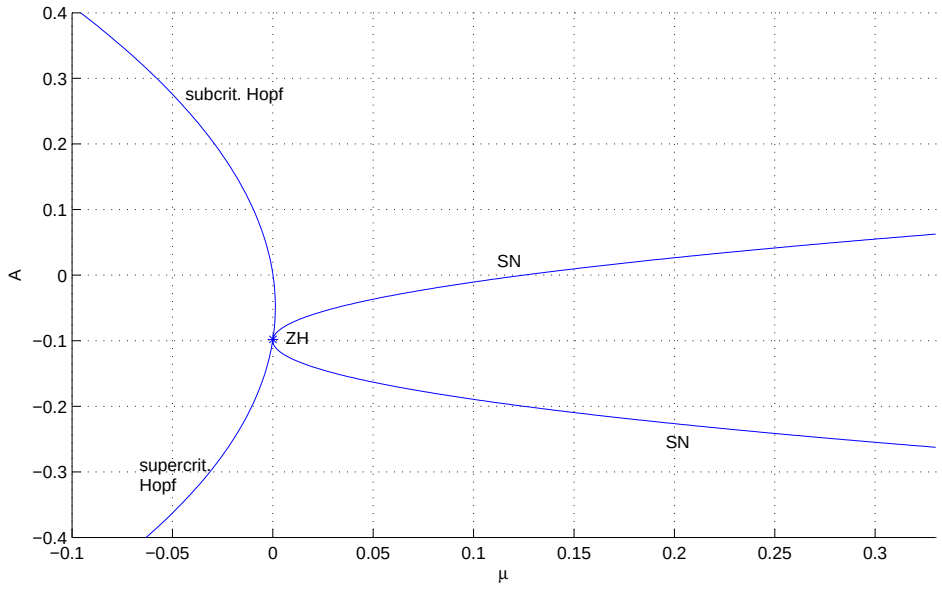

Figure B.11: Region VIIIa: (μ, A) bifurcation diagram for $(B, C) = (0.02, 0.1)$.

APPENDIX C

LOCATIONS OF DEGENERACIES OF BIFURCATION DIAGRAMS FOR THE SINGULAR HOPF NORMAL FORM

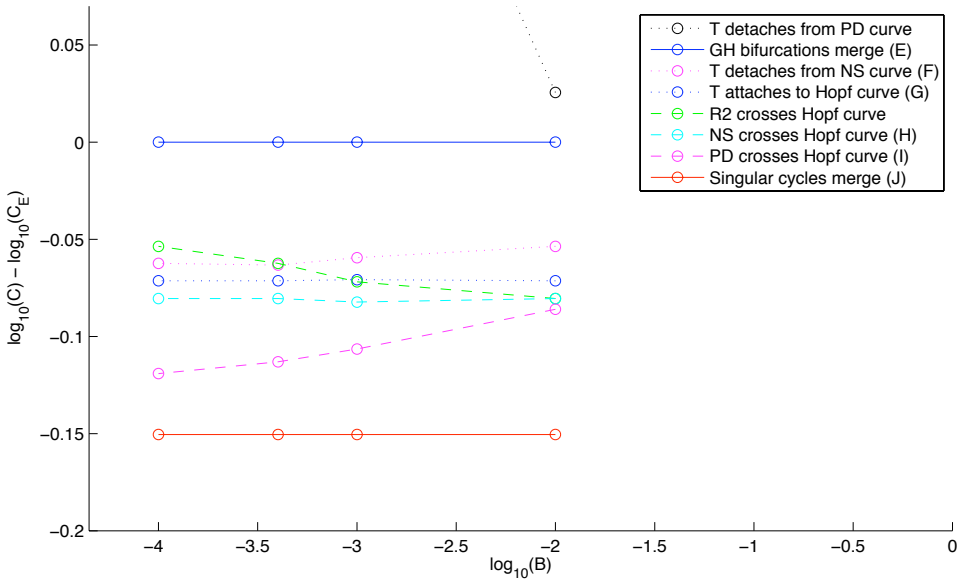

Figure C.1: Approximate positions of degeneracies of (μ, A) bifurcation diagrams of system (2.8) in (B, C) parameter space for $B, C > 0$. The legend lists eight types of degeneracies where (μ, A) slices of the parameter space fail to be transverse to codimension-two bifurcation surfaces. The function $C_E(B)$ is the value of C for which the two generalized Hopf (GH) bifurcations merge at a given value of B.

Inspecting (μ, A) bifurcation diagrams for a large number of parameters (B, C), it is easy to see that the catalog of diagrams in Appendix B completely describes the bifurcations of the types considered in this paper for $B < 0$. The completeness of the diagrams for $B > 0$ was verified by computing curves that separate the (B, C) plane into regions with qualitatively different (μ, A) bifurcation diagrams as shown in Figure C.1. Where applicable, the curve labels introduced in Chapter 3 are included in parentheses.

For numerical reasons, $|B|$ was restricted to lie between 10^{-4} and 10^{-2}. The positions of the folds of the generalized Hopf bifurcations and of the points where the slow flow has singular cycles are calculated using asymptotic relations. All other data points were obtained from sequences of (μ, A) bifurcation diagrams. The error in the ordinates of the data points is significant, but the order of the data points on the ordinate is correct for each value of B. Note how the dashed green line intersects several other curves, corresponding to further degeneracy in the set of (μ, A) bifurcation diagrams.

Figure B.2 illustrates the degeneracies that can occur in (μ, A) bifurcation diagrams if C is too large relative to $|B|^{1/2}$. The saddle-node bifurcation is close to intersecting the dashed curve where the slow-flow has singular cycles.

APPENDIX D

NUMERICAL METHODS TO COMPUTE THE TANGENCY CURVE

This appendix describes two non-rigorous numerical methods used for the computation of the tangency curves in Chapter 3 and Appendix B. The first method is a shooting method, used by Desroches et al. ([9]) to compute the tangency curve for the Koper model discussed in Section 3.4. The second method uses collocation and the software package AUTO [74].

The tangency bifurcation marks the onset of a bistability of trajectories in the unstable manifold $W^u(E_f)$ of the saddle-focus E_f near the origin: the repelling slow manifold S_r separates trajectories that flow to $X = -\infty$ from those that remain in the fold region. This observation motivates the use of a shooting algorithm to compute the position of the tangency curve in parameter space: given a set of parameters, a grid of initial conditions in a linear approximation of $W^u(E_f)$ is integrated numerically for a long time interval. The tangency curve separates the parameters where at least one trajectory reaches $X = -\infty$ from the parameters where all trajectories approach a bounded attractor. This curve can be computed by a two-parameter predictor-corrector continuation method starting from an initial parameter on the tangency curve, where the correction may be implemented using interval bisection.

The main disadvantage of this method is that it requires choices regarding the number of grid points and, more importantly, the length of the integration-time. Unless convergence to an attractor such as a limit cycle can be determined easily, this method cannot determine in an automated fashion whether a trajectory that has stayed in the fold region for a long period of time will remain in the fold region forever or leave it after a phase of transient behavior. For example, if E_f is close to a Hopf bifurcation curve, and the real part of its eigenvalues are thus close to zero, convergence to the periodic orbit

is slow and takes a very long time. In this case, the algorithm may give incorrect results unless the integration time is chosen adaptively.

The run-time of the algorithm described above is proportional to the number of grid points and the integration-time, as the bulk of the computation time of the algorithm is spent on numerical time-integration of trajectories that remain in the fold region for the entire integration time. Slight speed-ups can be achieved by choosing the order of time integrations for grids of initial conditions to start with points that are far apart in the fundamental domain. Sometimes, this locates a trajectory that escapes the fold region more quickly than choosing initial points consecutively along a segment of a fundamental domain of the linearized unstable manifold. We found that using more than 10 grid points did not improve the accuracy of the method significantly. Larger speed-ups are possible by parallelizing the algorithm. Since the tangency curve is smooth, parallelism can be implemented using a two-pass approach: in the first pass, a coarse approximation of the position of the curve is computed on a single processor with the algorithm described above, using large step-sizes, few grid points, and thus little computation time. The second pass interpolates between data points of the first pass, using larger numbers of interpolated points, more grid points and long integration times on multiple processors. This second pass is embarrassingly parallel.

The tangency curve can also be computed via continuation of a boundary value problem in AUTO. The boundary conditions require that trajectories begin on a fixed ray in the linear approximation of the equilibrium's unstable manifold and end on the parabola $Y = X^2 + 5$. An initial trajectory segment satisfying these requirements, obtained for example using the first method, can then be continued in one parameter. AUTO's fold detection determines when the continued solution folds, i.e. $W^u(E_f)$ and S_r intersect

tangentially. Switching to a continuation of the fold, the tangency can now be continued in two parameters. Computing the tangency curve in AUTO is in general much faster than the shooting method, but the shooting method provides additional insight into the fate of the trajectories in $W^u(E_f)$ before and after the tangency. As with the shooting method, the boundary value algorithm breaks down close to the Hopf curve, unless the number of mesh points is increased appropriately.

BIBLIOGRAPHY

[1] Z. Arai and K. Mischaikow, *Rigorous computations of homoclinic tangencies*, SIAM J. Appl. Dyn. Syst., 5 (2006), pp. 280–292.

[2] V. I. Arnold, V. Afrajmovich, Yu. S. Il'yashenko, and L. P. Shil'nikov, *Dynamical Systems V*, Encyclopaedia of Mathematical Sciences, Springer-Verlag, 1994.

[3] É Benoît, *Canards et enlacements*, Publ. Math. IHES Publ. Math., 72 (1990), pp. 63–91.

[4] É. Benoît, J. L. Callot, F. Diener, and M. Diener, *Chasse au canards*, Collect. Math., 31 (1981), pp. 37–119.

[5] B. Braaksma, *Singular Hopf bifurcation in systems with fast and slow variables*, J. Nonlinear Science, 8 (1998), pp. 457–490.

[6] X. Cabré, E. Fontich, and R. de la Llave, *The parameterization method for invariant manifolds. III. Overview and applications*, J. Differential Equations, 218 (2005), pp. 444–515.

[7] M. J. Capiński, *Covering relations and the existence of topologically normally hyperbolic invariant sets*, Discrete Contin. Dyn. Syst., 23 (2009), pp. 705–725.

[8] M. J. Capiński and P. Zgliczyński, *Cone conditions and covering relations for topologically normally hyperbolic invariant manifolds*, Discrete Contin. Dyn. Syst., 30 (2011), pp. 641–670.

[9] M. Desroches, J. Guckenheimer, B. Krauskopf, C. Kuehn, H. M. Osinga, and M. Wechselberger, *Mixed-mode oscillations with multiple time scales*, SIAM Review, 54 (2012), pp. 2011–288.

[10] M. Desroches, B. Krauskopf, and H. M. Osinga, *Mixed-mode oscillations and slow manifolds in the self-coupled FitzHugh-Nagumo system*, Chaos, 18 (2008).

[11] M. Desroches, B. Krauskopf, and H. M. Osinga, *The geometry of slow manifolds near a folded node*, SIAM J. Appl. Dyn. Sys., 7 (2008), pp. 1131–1162.

[12] M. Desroches, B. Krauskopf, and H. M. Osinga, *Numerical continuation of canard orbits in slow-fast dynamical systems*, Nonlinearity, 23 (2010), pp. 739–765.

[13] F. Dumortier and R. Roussarie, *Canard cycles and center manifolds* Mem. Amer. Math. Soc., 577 (1996).

[14] J. P. England, B. Krauskopf, and H. M. Osinga, *Computing two-dimensional global invariant manifolds in slow-fast systems*, Internat. J. Bifur. Chaos Appl. Sci. Engrg., 17 (2007), pp. 805–822.

[15] N. Fenichel, *Persistence and smoothness of invariant manifolds for flows*, Indiana Univ. Math. Journal, 21 (1971), pp. 1109–1137.

[16] W. Govaerts, *Numerical methods for bifurcations of dynamical equilibria*, SIAM, 2000.

[17] Andreas Griewank and Andrea Walther, *Evaluating Derivatives: Principles and Techniques of Algorithmic Differentiation*, second edition, SIAM, 2008.

[18] J. Guckenheimer, *Phase portraits of planar vector fields: computer proofs*, Experiment. Math., 4 (1995), pp. 153–165.

[19] J. Guckenheimer, *Singular Hopf bifurcation in systems with two slow variables*, SIAM J. Appl. Dyn. Syst., 7 (2008), pp. 1355–1377.

[20] J. Guckenheimer and R. Haiduc, *Canards at folded nodes*, Mosc. Math. J., 5 (2005), pp. 91–103.

[21] J. Guckenheimer and P. J. Holmes, *Nonlinear Oscillations, Dynamical Systems, and Bifurcations of Vector Fields*, Springer-Verlag, New York, 1983.

[22] J. Guckenheimer, T. Johnson, and P. Meerkamp, *Rigorous enclosures of a slow manifold*, SIAM J. Appl. Dyn. Syst., to appear, e-print: arXiv:1201.1948.

[23] J. Guckenheimer and C. Kühn, *Computing slow manifolds of saddle type*, SIAM J. Appl. Dyn. Syst., 8 (2009), pp. 854–879.

[24] J. Guckenheimer and P. Meerkamp, *Unfoldings of singular Hopf bifurcation*, SIAM J. Appl. Dyn. Syst., to appear, e-print: arXiv:1107.3185.

[25] J. Guckenheimer and C. Scheper, *A geometric model for mixed-mode oscillations in a chemical system*, SIAM J. Appl. Dyn. Syst., 10 (2011), pp. 92–128.

[26] J. Guckenheimer and A. R. Willms, *Asymptotic analysis of subcritical Hopf-homoclinic bifurcation*, Physica D, 139 (2000), pp. 195–216.

[27] E. Hairer and G. Wanner, *Solving ordinary differential equations. II. Stiff and differential-algebraic problems*, Second edition, Springer Series in Computational Mathematics, Springer-Verlag, Berlin, 1996, xvi+614 pp.

[28] M. W. Hirsch, C. C. Pugh, and M. Shub, *Invariant manifolds*, Lecture Notes in Mathematics, Vol. 583. Springer-Verlag, Berlin-New York, 1977.

[29] A. J. Homburg, H. Kokubu, and V. Naudot, *Homoclinic doubling cascades*, Arch. Rational Mech. Anal., 160 (2001), pp. 195–243.

[30] E. M. Izhikevich, *Neural excitability, spiking and bursting*, Internat. J. Bifur. Chaos Appl. Sci. Engrg., 10 (2000), pp. 1171–1266.

[31] T. Johnson and W. Tucker, *A note on the convergence of parametrised non-resonant invariant manifolds*, Qualitative Theory of Dynamical Systems, 10 (2011), pp. 107–121.

[32] T. Johnson and W. Tucker, *On a computer-aided approach to the computation of Abelian integrals*, BIT - Numerical Mathematics, 51 (2011), pp. 653–667.

[33] T. Johnson and W. Tucker, *On a fast and accurate method to enclose all zeros of an analytic function on a triangulated domain*, in Proceedings of PARA - 2008, to appear in Lecture Notes in Computer Science 6126/6127 Springer-Verlag, 2011.

[34] C. K. R. T. Jones, *Geometric singular perturbation theory*, Dynamical systems (Montecatini Terme, 1994), Lecture Notes in Math., 1609, Springer, Berlin, 1995, pp. 44–118.

[35] A. Katok and B. Hasselblatt, *Introduction to the Modern Theory of Dynamical Systems*, Cambridge University Press, Cambridge, 1995.

[36] M. Kisaka, H. Kokubu, and H. Oka, *Bifurcations to N -homoclinic orbits and N -periodic orbits in vector fields*, J. Dyn. Differential Equations, 5 (1993), pp. 305–357.

[37] M. Kisaka, H. Kokubu, and H. Oka, *Supplement to homoclinic-doubling bifurcation in vector elds*, in: R. Bamon, R. Labarca, J. Lewowicz, J. Palis (eds.), Dynamical Systems, Longman, New York, 1993, pp. 92–116.

[38] M. T. M. Koper, *Bifurcations of mixed-mode oscillations in a three-variable autonomous Van der Pol-Duffing model with a cross-shaped phase diagram*, Physica D, 80 (1995), pp. 72–94.

[39] B. Krauskopf, H. M. Osinga, E. J. Doedel, M. E. Henderson, J. Guckenheimer, A. Vladimirsky, M. Dellnitz, and O. Junge, *A survey of methods for computing (un)stable manifolds of vector fields*, Internat. J. Bifur. Chaos Appl. Sci. Engrg., 15 (2005), pp. 763–791.

[40] B. Krauskopf, H. M. Osinga, and J. Galan-Vioque, *Numerical Continuation Methods for Dynamical Systems*, Springer-Verlag, Berlin / New York, 2007.

[41] M. Krupa, N. Popovic, and N. Kopell, *Mixed-mode oscillations in three time-scale systems: A prototypical example*, SIAM J. Appl. Dyn. Sys., 7 (2008), pp. 361–420.

[42] M. Krupa and M. Wechselberger, *Local analysis near a folded saddle-node singularity*, J. Differential Equations, 248 (2010), pp. 2841–2888.

[43] C. Kuehn, *Global return maps for mixed-mode oscillations with one fast and two slow variables*, Chaos, 21 (2011).

[44] Y. A. Kuznetsov, *Elements of applied bifurcation theory*, Springer, New York, 3rd Edition, 2004.

[45] R. de la Llave, *A tutorial on KAM theory*, Smooth ergodic theory and its applications (Seattle, WA, 1999), Proc. Sympos. Pure Math., Amer. Math. Soc. Providence, RI. 69, 2001, pp. 175–292.

[46] R. Lohner, *Einschließung der Lösung gewöhnlicher Anfangs- und Randwertaufgaben und Anwendungen*, PhD thesis, Universität Karlsruhe, 1988.

[47] S. Luzzatto and P. Pilarczyk, *Finite resolution dynamics*, Found. Comput. Math., 11 (2011), pp. 211–239.

[48] A. Milik and P. Szmolyan, *Multiple time scales and canards in a chemical oscillator*, Multiple-Time-Scale Dynamical Systems (Minneapolis, 1997), IMA Vo. Math. Appl. 122, Springer-Verlag, New York, 2001, pp. 117–140.

[49] R. E. Moore, *Interval Analysis*, Prentice-Hall, Englewood Cliffs, New Jersey, 1966.

[50] N. S. Nedialkov and K. R. Jackson. *An interval Hermite-Obreschkoff method for computing rigorous bounds on the solution of an initial value problem for an ordinary differential equation*, Reliab. Comput., 5 (1999), pp. 289–310.

[51] N. S. Nedialkov, K. R. Jackson, and G. F. Corliss, *Validated solutions of initial value problems for ordinary differential equations*, Appl. Math. Comput., 105 (1999), pp. 21–68.

[52] N. S. Nedialkov, K. R. Jackson, and J. D. Pryce, *An effective High-Order Interval Method for Validating Existence and uniqueness of the Solution of an IVP for an ODE*, Reliab. Comput., 7 (2001), pp. 449–465.

[53] A. Neumaier, *Interval Methods for Systems of Equations*, Encyclopedia of Mathematics and its Applications 37, Cambridge Univ. Press, Cambridge, 1990.

[54] B. E. Oldeman, B. Krauskopf, and A. R. Champneys, *Death of period-doublings: locating the homoclinic doubling cascade*, Physica D, 146 (2000), pp. 100–120.

[55] J. Ombach, *Computation of the local stable and unstable manifolds*, Univ. Iagel. Acta Math., 32 (1995), pp. 129–136.

[56] V. Petrov, S. Scott, and K. Showalter, *Mixed-mode oscilllations in chemical systems*, J. Chem. Phys., 97 (1992), pp. 6191–6198.

[57] B. Sandstede, *Verzweigungstheorie homokliner Verdopplungen*, Ph.D. Thesis, Freie UniversitŁt Berlin, Institut fr Angewandte Analysis und Stochastic, Berlin, Report No. 7, 1993.

[58] C. Simó, *On the Analytical and Numerical Approximation of Invariant Manifolds*, Les Méthodes Modernes de la Mecánique Céleste, D Benest and C Foeschlé (eds.), Editions Frontièrs, Paris, 1990, pp. 285-329.

[59] P. Szmolyan and M. Wechselberger, *Canards in R^3*, J. Differential Equations, 177 (2001), pp. 419-453.

[60] J. Tabak, N. Toporikova, M. E. Freeman, and R. Bertram, *Low dose of dopamine may stimulate prolactin secretion by increasing fast potassium currents*, in Journal of Computational Neuroscience, 28 (2007), pp. 211–222.

[61] F. Takens, *Forced oscillations and bifurcations*, in Applications of Global Analysis, Math. Inst. Rijksuniv, Utrecht, 3 (1974), pp. 1–61, 1974, reprinted in Global analysis of dynamical systems, Inst. Phys., Bristol, pp. 1–59, 2001.

[62] N. Toporikova, J. Tabak, M. E. Freeman, and R. Bertram, *A-type* K^+ *current can act as a trigger for bursting in the absence of a slow variable*, Neural Computation 20 (2008), pp. 436-451.

[63] W. Tucker, *Validated numerics. A short introduction to rigorous computations*, Princeton University Press, Princeton, NJ, 2011, xii+138 pp.

[64] T. Vo, R. Bertram, J. Tabak, and M. Wechselberger, *Mixed-mode oscillations as a mechanism for pseudo-plateau bursting*, J. Comput. Neurosci. 28 (2010), pp. 443–458.

[65] T. Vo, R. Bertram, and M. Wechselberger, *Bifurcations of canard-induced mixed-mode oscillations in a pituitary lactotroph model*, Discrete and Continuous Dyn. Syst., 32 (2011), pp. 2879–2912.

[66] M. Wechselberger, *Existence and bifurcation of canards in* $\mathbb{R}^3$ *in the case of a folded node*, SIAM J. Appl. Dyn. Syst., 4 (2005), pp. 101–139.

[67] M. Wechselberger, *À propos de canards (Apropos canards)*, Trans. Am. Math. Soc., in press.

[68] D. Wilczak and P. Zgliczyński, *Computer assisted proof of the existence of homoclinic tangency for the Hénon map and for the forced damped pendulum*, SIAM J. Appl. Dyn. Syst., 8 (2009), pp. 1632–1663.

[69] P. Zgliczyński, C^1 *Lohner algorithm*, Found. Comput. Math. , 2 (2002), pp. 429–465.

[70] P. Zgliczyński, *Covering relations, cone conditions and stable manifold theorem*, J. Differential Equations, 246 (2009), pp. 1774–1819.

[71] P. Zgliczyński and M. Gidea, *Covering relations for multidimensional dynamical systems*, J. Differential Equations, 202 (2004), pp. 32–58.

[72] Wolfram Research, Inc., *Mathematica, Version 8.0*, Champaign, IL, 2010.

[73] The MathWorks, *MATLAB (2009a)*, Natick, MA, 2009.

[74] *AUTO: Software for continuation and bifurcation problems in ordinary differential equations*, available at `http://cmvl.cs.concordia.ca/auto/`, 2010.

[75] *Computational Geometry Algorithms Library*, available at `www.cgal.org/`.

[76] S. M. Rump *INTLAB - INTerval LABoratory*, in Tibor Csendes, editor, Developments in Reliable Computing, Kluwer Academic Publishers, Dordrecht, 1999, pp. 77–104.

[77] A. Dhooge, W. Govaerts, and Y. A. Kuznetsov, *MatCont: A MATLAB package for numerical bifurcation analysis of ODEs*, ACM Trans. Math. Software, 29(2003), pp. 141–164, software available from `http://sourceforge.net/projects/matcont/`.

[78] *VNODE-LP A validated Solver for Initial Value Problems in Ordinary Differential Equations*, available at `www.cas.mcmaster.ca/~nedialk/Software/VNODE/VNODE.shtml`.

[79] Program files supplementing the chapter on singular Hopf bifurcation in a pituitary lactotroph model, available at `www.math.cornell.edu/~pmeerkamp`.

[80] Program files supplementing the chapter on enclosures of slow manifolds, available at `www.math.cornell.edu/~tjohnson`.